Theses and Dissertations   Graduate School

2013

Optimization of Radiation Therapy in Time-Dependent Anatomy

W. Tyler Watkins
Virginia Commonwealth University

www.manaraa.com

OPTIMIZATION OF RADIATION THERAPY IN TIME-DEPENDENT ANATOMY

A dissertation submitted in partial fulfillment of the requirements for the degree of
Doctor of Philosophy in Medical Physics at Virginia Commonwealth University.

by

William Tyler Watkins

M.S. Physics, San Diego State University, 2009

B.S. Physics, San Diego State University, 2003

Director: Jeffrey V. Siebers, Ph.D.

Professor and Director, Medical Physics Graduate Program

Department of Radiation Oncology

Virginia Commonwealth University

Richmond, Virginia

May, 2013

Acknowledgement

Thank you God for bringing me close to the people I have known and loved, all of you have

contributed to who I am, and what I have accomplished.

TABLE OF CONTENTS

LIST OF TABLES

LIST OF FIGURES

ABSTRACT

OPTIMIZATION OF RADIATION THERAPY IN TIME DEPENDENT ANATOMY

William Tyler Watkins, Ph.D.

Major Director: Jeffrey V. Siebers, Ph.D.
Professor and Director, Medical Physics Graduate Program
Department of Radiation Oncology

The objective of this dissertation is to develop treatment planning techniques that have the potential to improve radiation therapy of time-dependent (4D) anatomy. Specifically, this study examines dose estimation, dose evaluation, and decision making in the context of optimizing lung cancer radiation therapy.

Two methods of dose estimation are compared in patients with locally advanced and early stage lung cancer: dose computed on a single image (3D-dose) and deformably registered,

accumulated dose (or 4D-dose). The results indicate that differences between 3D- and 4D-dose are not significant in organs at risk (OARs), however, 4D-dose to a moving lung cancer target can deviate from 3D-dose. These differences imply that optimization of the 4D-dose through multiple-anatomy optimization (MAO) can improve radiation therapy in 4D-anatomy. MAO incorporates time-dependent target and OAR geometry while enabling a simple, clinically realizable delivery. MAO has the potential to enhance the therapeutic ratio in terms of target coverage and OAR sparing in 4D-anatomy.

In dose evaluation within 4D-anatomy; dose-to-mass is a more intuitive and precise metric in estimating the effects of radiation in tissues. Assuming physical density is proportional to functional tissue density, dose-to-mass has a 1-1 correspondence with radiation damage. Dose-to-mass optimization boosts dose in massive regions of lung cancer targets and can reduce integral dose to lung by preferentially treating through regions of low-density lung tissue.

Finally, multi-criteria optimization (MCO) is implemented in order to clarify decision making during plan design for lung cancer treatment. An MCO basis set establishes a patient-specific decision space which reveals trade-offs in OAR-dose at a fixed, constrained target dose. By interpolating the MCO basis set and evaluating the plan on 4D-anatomy, patient- and organ-specific conservatism in plan design can be expressed in real time.

Through improved methods of dose estimation, dose evaluation, and decision making, this dissertation will positively impact radiation therapy of time-dependent anatomy.

1   Introduction

Chapter 1 list of abbreviations:

DNA - deoxyribonucleic acid

RT – radiation therapy

LINAC – linear accelerator

MLC- multi-leaf collimator

3DCRT – 3D conformal radiation therapy

IMRT – intensity modulated radiation therapy

beamlet – (radiation) beam element

CT – computed tomography

OAR – organ at risk

Radiation therapy is a mainstay in the treatment of cancer. Radiation damages cells through ionization with the potential to alter atomic and molecular bonds including bonds in deoxyribonucleic acid (DNA). With sufficient radiation dose (energy imparted per unit mass), a loss of cell-functionality will occur which often includes impaired cell ability to repair and reproduce. The potential to impair harmful cells (i.e. cancer) with radiation is the basis of radiation therapy (RT). The goal of RT is to destroy cancer cells while minimizing damage to

healthy, normal tissue; in other words to maximize radiation's therapeutic ratio. The overall objective of this work is to develop and investigate methods which, when implemented, will improve the therapeutic ratio of radiation therapy for lung cancer.

One premise of RT is that cancer can be identified and localized (including delineation from healthy, normal tissue). Assuming this premise is met, collimation of radiation from an external source allows design of an RT plan which specifically targets tumors and avoids healthy tissue. Specifically, external beam RT utilizing photons produced from a linear accelerator (LINAC), shaped with a multi-leaf collimator (MLC), and delivered from multiple beam angles have enabled design of RT-dose distributions which conform to patient-specific anatomy. This specialized, highly conformal treatment is called 3D-conformal radiation therapy (3DCRT). 3DCRT has since evolved into intensity modulated radiation therapy (IMRT) where each beam element (beamlet) is modulated according to patient-specific anatomy to maximize dose to tumors while minimizing dose to normal tissues. In order to design (or plan) an IMRT treatment, several postulates are necessary including (but not limited to) a sufficiently accurate patient representation through imaging such as computed tomography (CT), accurate dose estimation in the simulated anatomy, well-defined evaluation metrics and objectives, and prudent decision making in plan design.

This dissertation focuses on RT for treatment of lung cancer. While the methods apply to other cancer sites, fulfilling the preconditions of IMRT for planning and treatment of lung cancer is particularly challenging. Lung cancer RT is complicated by many factors including large heterogeneities in lung tissue, respiratory motion, and high-incidence of complications in surrounding organs at risk (OARs). These challenges may be relevant to poor survival rates in

lung cancer patients, but there are too many confounding factors in lung cancer survival to make such a claim. According to the National Cancer Institute, overall five year relative survival of lung cancer patients (all types and stages) is 15.9%.[1] Competing mortality combined with complications in detection and diagnosis make drawing conclusions about the efficacy of RT for long-term survival of patients with lung cancer very challenging. However, by increasing the therapeutic ratio an increase in RT efficacy can be inferred.

1.1 SPECIFIC AIMS

The objective of this work is to implement and develop techniques which have the potential to improve the therapeutic ratio of radiation therapy in time-dependent (4D) anatomy. These techniques address the preconditions of IMRT treatment in time-dependent anatomy. Specifically, this dissertation focuses on (1) dose estimation within simulated anatomy, (2) evaluation metrics used to determine the quality of treatment and (3) decision making during plan design, including plan-optimization.

In order to describe the three specific aims of this work with added detail in Chapter 3, Chapter 2 introduces basic concepts in RT and summarizes current techniques for lung cancer RT. The planning process includes patient simulation, treatment planning, treatment evaluation, inclusion of uncertainty, and plan optimization. Chapter 2 also describes the patient cohort used in this dissertation and resulting publications and manuscripts (included in Appendices A-E). Chapters 4-7 are dedicated to the specific aims of this work; Chapter 8 draws conclusions and describes future work.

2 Radiation Therapy Planning for Lung Cancer

Chapter 2 list of abbreviations:

4DCT – four dimensional computed tomography

aCT – average CT image

MIP – maximum intensity projection image

RPM™- Varian Medical Systems, Palo Alto, CA

RTP – radiation therapy planning

GTV – gross tumor volume

CTV – clinical tumor volume

ITV – internal target volume

PTV – planning target volume

OAR – organ at risk

MAO – multiple anatomy optimization

LQ – linear quadratic

Gy – Grey (1 Joule / kilogram)

D_{tot} – total physical dose

N_{fx} – number of fractions

BED – biologic equivalent dose

SBRT – stereotactic body radiation therapy

RTOG – radiation therapy oncology group

DVH – dose volume histogram

TCP – tumor control probability

NTCP – normal tissue complication probability

QUANTEC - quantitative analysis of normal tissue effects in the clinic

IGRT – image guided radiation therapy

CBCT – cone beam computed tomography

SM – setup margin

IM – internal margin

RTV – representative target volume

ROI – region of interest

TPS – treatment planning system

BFGS – Broyden-Fletcher-Goldfarb-Shanno

LA – locally advanced

NSCLC – non-small cell lung cancer

MCO – multi-criteria optimization

DMH – dose-mass histogram

The purpose of this Chapter is to introduce relevant methods in the practice of radiation

therapy (RT) for lung cancer. The sections are divided according to different stages of the RT

process. Simulation imaging allows for computerized treatment planning. Plan evaluation and incorporation of uncertainty allows for plan optimization. Finally, a group of lung cancer patients is described in Section 2.6, these patients' image-sets are utilized throughout this document and related publications.

2.1 SIMULATION IMAGING

The current standard for CT-simulation of lung cancer patients is four-dimensional computed tomography (4DCT).[2,3] X-ray projections are acquired throughout the respiratory cycle in order to capture patient-specific, time-dependent anatomic features including the tumor boundaries. The projections are sorted and reconstructed into phase images (labeled by a percentage) and each phase image represents a portion of the breathing period; common breathing periods range from 3-6 seconds (s)[4,5]. If the breathing cycle is divided into 10-phase images the temporal resolution of each phase image is approximately 0.3-0.6 s, depending on the patient specific breathing pattern. The 4DCT image set is composed of 3D-images which, when considered together, represent a 4D-model of patient anatomy and its motion during respiration.

4DCT image sets are susceptible to image artifacts due to many factors including breathing irregularities and intra-phase residual motion. Yamamoto *et al.*[6] examined 50 4DCT image sets and found that approximately half contained blurring and/or sorting artifacts. Some level of blurring always exists in 4DCT phase images due to intra-phase residual motion. The extent of intra-phase residual motion is patient-specific but can be minimized through proper acquisition techniques including minimizing gantry rotation speed.[7] 4DCT projections (or slices) are sorted

based on signals acquired during image acquisition. One common signal is a breathing trace acquired through an infrared camera, e.g. the real-time position management (RPM) camera (RPM™, Varian Medical Systems, Palo Alto, CA). Others have reported using spirometers (e.g. Lu *et al.*[8]), compression belts (e.g. Werner *et al.*[9]), or internal anatomy.[10] Irregular or erratic breathing can cause incorrect or inconsistent phase labeling and can result in sorting artifacts. One cycle of a breathing pattern is shown in Figure 1 with the approximate respiratory phases labeled according to assignment from the RPM system.
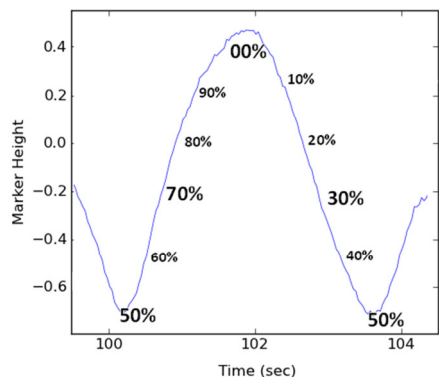
Figure 1. An example of a breathing cycle acquired from an infrared camera recording a marker block placed on a patient's chest. The approximate respiratory phases are labeled as a percentage, with maximum inhale phase labeled 00%, exhale is 50%.

In this dissertation, the 4DCT image set is assumed to be a sufficiently accurate representation of the patient anatomy in order to perform RT treatment planning. Clinically, if plan-limiting artifacts are detected during the planning process a new simulation set (through re-acquisition or alternate reconstruction methods) is necessary in order to implement the methods described herein. In Chapter 6, an automated method of identifying image artifacts through evaluation of inter-phase mass conservation is developed.

For the most part, current clinical radiation therapy planning (RTP) software is designed to handle a single image for dose calculation and plan optimization. Despite the availability of 4DCT image sets for lung cancer patients, a single image is often used to approximate the moving anatomy in RTP. The chosen, single image is designated the planning image. Common

planning images used for clinical RT of lung cancer include a single phase image (e.g. mid-ventilation, 30% phase) or a composite image such as the average CT (aCT) density[11] or the maximum intensity projection (MIP).[12,13] Figure 2 shows a coronal slice of each of these images for one patient included in this dissertation; the 30% phase (left), aCT (middle), and MIP (right) have different density information resulting in different targets delineated on each image.
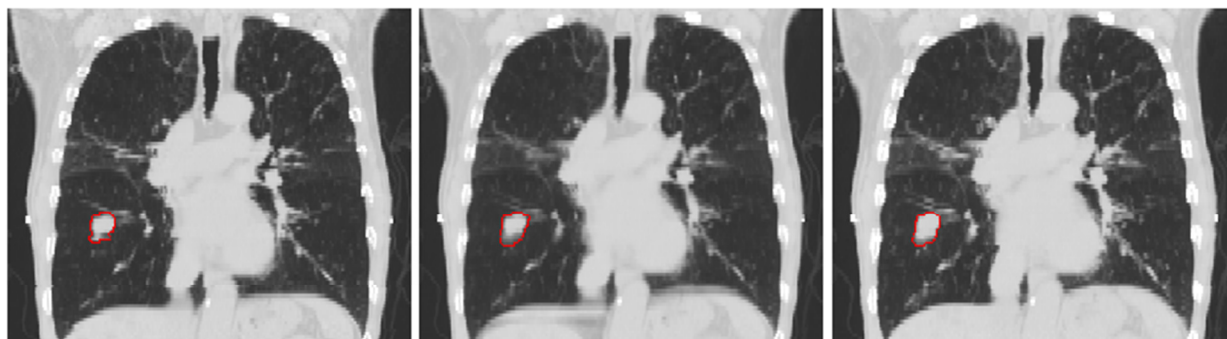
Figure 2. Images commonly used for radiation therapy planning of lung cancer include the 30% phase image (left), the average 4DCT density (middle), or the maximum intensity projection (right). Physician delineations of the tumor (red) differ between the image sets.

Approximating 4D-anatomy with a single image may have an effect on RT treatment; this approximation introduces uncertainty in structure definition, in dose-estimation, and in plan optimization. One hypothesis of this work is that inclusion of the entire 4DCT image-set will improve dose estimation, plan evaluation, and plan optimization in RTP of lung cancer. This hypothesis is examined for dose calculation in Chapter 4, for plan evaluation in Chapter 6-7, and for plan optimization in Chapters 5.

2.2 PLANNING TECHNIQUES

Several methods have been introduced for RT of lung cancer which specifically account for respiratory motion and lung tissue heterogeneities. Motion management techniques are summarized in the American Association of Physicists in Medicine (AAPM) task-group report 76 (TG-76)[14] and are summarized in the following paragraphs.

In order to accurately identify the moving lung-cancer target the gross tumor volume (GTV) is delineated on all phases of the 4DCT-image set by an expert physician. As described in ICRU report 62[15], the GTV is expanded to account for microscopic disease into a clinical target volume (CTV). The union of phase-based CTVs is defined as the lung cancer internal target volume (ITV)[15–17] which is used as a surrogate for the actual, moving CTV. The ITV-method is the most common approach in designing a lung-cancer target surrogate. An ITV-plan is designed to deliver uniform dose to the entire ITV to while the patient breathes freely (free-breathing treatment) and/or consistently with breathing captured during 4DCT acquisition. Figure 3 shows a coronal slice of an aCT-image with a dose distribution designed to deliver uniform dose to the ITV.

The ITV is expanded into a planning target volume (PTV) in order to account for inter-

Figure 3. A coronal slice of an average-CT (aCT) image with an ITV (black) delineated. The dose distribution intends to treat 95% of the ITV to 70 Gy. The motion of the diaphragm can be inferred from the blurred density in the inferior lung.
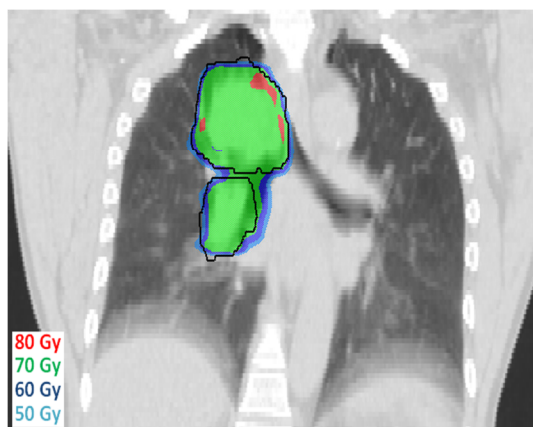
fraction geometric deviations (or set-up error) between the LINAC and the ITV coordinate systems. Uncertainty in lung cancer RT and PTV design is described in more detail in section 2.4. The assumption of the ITV-planning approach is that a uniform dose to the entire ITV will result in a uniform dose to the moving CTV which, by definition, is always contained within the ITV. This dissertation examines this assumption in Chapter 4.

When motion of the GTV is large (e.g. >1 cm) and respiratory motion is quasi-periodic and predictable, respiratory gating is an option.[18,19] Gating attempts to exploit breathing periodicity by triggering the LINAC on and off in order to treat only during a pre-specified portion of the breathing cycle, when the target is assumed to be at a known position. The beam on/off trigger is often based on the position of a surrogate on the patient surface. The 4DCT simulation images used for planning establish a correlation between surrogate and tumor locations. The validity of this correlation, however, has slowed universal implementation of gating. Specifically, the reproducibility of the phase images as a function of surrogate position over the course of RT is cause for concern. If the tumor location, as a function of surrogate position, deviates from the information conveyed from 4DCT images there is a possibility of target miss. Prohibitively long treatment times limit the minimum gating window (composed of the number of phases treated during each beam-on cycle) resulting in residual motion during beam-on times. Reducing the gating window reduces residual motion and increases treatment time. The beam-on window necessitates construction of a gated-ITV; a union of CTVs defined in phases designated for beam-on. Both free-breathing and gated RT use a union of phase-based CTVs to form an ITV on a single planning image which is used for dose computation and plan design (or optimization).[20]

Similar to gating, breath-hold RT attempts to treat in a portion of the breathing cycle while the patient, either voluntarily[21] or through active control[22], holds their breath. Breath-hold RT is a viable method of motion management for patients comfortable with holding their breath or using an active-control device. This limits the applicability in lung cancer RT due to disease-related difficulty in breathing.[14] Similar to gating, efficient delivery may depend on the ability of the patient to hold their breath. However, if the breath-hold technique is well-tolerated during simulation and/or training, it is a reasonable solution for minimizing (or more ideally, eliminating) respiratory motion during RT. Determining the uncertainties associated with the technique, and specifically the reproducibility of individual breath holds remains an active area of interest.[23,24]

Another option for treating a moving target is tracking. Target tracking designs time-dependent MLC apertures which follow the moving target in real time; it is an idealized solution for treating a moving target.[25–27] The tracking plan is designed on multiple phase images and considers the actual target (not an ITV). However, target tracking requires real time knowledge of tumor position (e.g. through imaging or a surrogate) in order to synchronize delivery with motion. System latency between tracked positions and delivery necessitates prediction[28,29], but the predictability of respiration is also a cause for concern. If a prediction model relies on prior information, inter-fraction breathing variations must be minimized which may be possible with, e.g., breath coaching.[30] Tracking is not implemented clinically due to these (and other) concerns, but may be in the future.

There is evidence that gating, breath-hold, and tracking have the potential to increase the therapeutic ratio compared to ITV planning.[19,21,22,27,31–33] However, these methods involve

complicated deliveries, new technology, and may create patient discomfort. This dissertation attempts to improve on the ITV method of RTP for lung cancer by utilizing a 4D-optimization which designs plans that can be delivered during free breathing. The method inherently includes all information available in 4DCT and is evaluated on a patient cohort representative of a large population of lung cancer patients and potential advantages are discussed. The method is termed multiple anatomy optimization (MAO) and is discussed in Chapter 5.

2.3 EVALUATION OF RADIOTHERAPY PLANS

Most often, an optimized RT dose distribution is delivered to the patient in multiple treatment sessions, termed fractions. Ideally, the number of fractions is determined from biologic differences in repair and repopulation of tumors and normal tissues which can be estimated from the linear-quadratic (LQ) model of cell survival.[34] However, the historic treatment of 2 Gy per day (1 Gy = 1 Joule/kg) often determines the number of fractions (see, e.g. Fowler[35] or Barendsen[36]), i.e. for a total dose of D_{tot} the number of fractions $N_{fx}=D_{tot}/2$ Gy. Hypo-fractionated RT, however, is transforming the 2 Gy/day approach and prescribing a higher dose per fraction (e.g. 12 Gy/fraction) for many treatments.

The α/β ratio is a retrospectively derived quantity based on the LQ model.[34] According to the model, the number of surviving cells N from an initial cell population of N_0, after irradiation to dose D is

$$N/N_0 = exp\left(-\alpha D - \beta D^2\right)$$

Biologic Equivalent Dose (BED)[35] considers the effects of fractionation and radiation sensitivity according to the LQ model. It is computed based on the number of fractions (N_{fx}), dose per fraction (D_{fx}), and the α/β ratio according to

$$BED = N_{fx}D_{fx}\left(1 + \frac{D_{fx}}{\alpha/\beta}\right).$$

For lung cancer RT, the number of fractions can be as few as 1 in hypo-fractionation[37] in stereotactic body radiation therapy (SBRT) of early stage lung cancer, while 30-35 fractions is the standard of care in conventional-fractionation for locally advanced, stage III and greater disease.[38]

The appropriate prescription dose level in order to achieve local control in non-small cell lung cancer (NSCLC) is debatable. The uncertainty in the appropriate value arises due to many factors including competing morbidity and the effects of chemotherapy combined with RT. However, for traditional fractionation, physical doses of at least 60 Gy and not more than 84 Gy are appropriate according to the results of (Radiation Therapy Oncology Group) RTOG-9311[38,39] based on 3DCRT planning and delivery. Bradley *et al.*[38] established a possible upper limit on treatment dose based on two dose-related deaths of 40 patients treated to a physical dose of 90.3 Gy in 42 fractions. For a given treatment protocol, the total treatment dose is often a compromise between a dose sufficient to eradicate the tumor and the ability of collateral dose to spare normal tissues. A realistic value for physical dose and fractionation routine for locally advanced disease is 70 Gy delivered in 33 fractions[38] which is the prescription used in this work.

In SBRT of lung cancer, physical doses up to 24 Gy in a single fraction have been reported[40], however a more common regimen is 40-70 Gy in 3-4 fractions as prescribed in RTOG- 0236, RTOG-0915, and the Japan Clinical Oncology Group trial 0403. The physical dose of 50 Gy delivered in four fractions, assuming α/β = 10 Gy, results in a BED>100 Gy but some authors have questioned the validity of the linear-quadratic model for single fraction doses >5 Gy.[41] For SBRT patients in this work, a physical prescription dose of 48 Gy is used.

One method to evaluate physical dose is through the dose-volume histogram (DVH). The DVH is a 2D graph of (relative) volume parameterized at dose levels. The DVH was introduced in a letter by Shipley *et al.*[42] in order to graphically display a proportion of posterior rectal wall at variable dose levels. The DVH has since become an important utility for assessing dose and the quality of RT plans. The DVH currently influences decision making in plan approval, in optimization, and in retrospective evaluation. By relating tumor control probability (TCP) and normal tissue complication probability[43] (NTCP) to non-uniform dose to partial volumes of a region of interest (ROI) through the DVH, a reasonable estimate of safe and effective treatment is possible.[44]

Figure 4. Patient anatomy (top left) and a dose-distribution (top right) are combined to form a 2D plot of relative volume at dose, the dose-volume histogram (DVH).
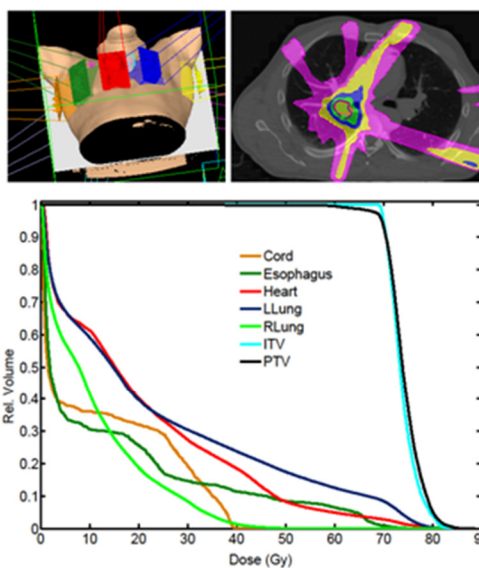
Figure 4 shows 3D- anatomy and dose, which can be combined to form a DVH. The DVH shown in Figure 4 includes the target (the PTV) and organs

at risk (OARs) typically considered in lung cancer RT including the spinal cord, esophagus, heart, and both lungs (where ipsi- and contra- lateral positions are defined with respect to the tumor).

A more recently introduced method to evaluate physical dose is the generalized equivalent uniform dose (*gEUD*)[45] which is mathematically equivalent to a generalized mean (or power mean) of dose with an organ-specific exponent *a*. Considering a structure composed of *n* voxels, where fractional dose to the ith voxel is $D_{fx,i}$, the *gEUD* of the structure is computed according to

$$gEUD = N_{fx} \left(\frac{1}{n} \sum_{i \in n} \left(D_{fx,i} \right)^{a_n} \right)^{1/a_n}$$

.Based on decades of published complication rates for patients who received RT, the QUANTEC (Quantitative Analysis of Normal Tissue Effects in the Clinic) reports[46] summarize normal tissue reactions to partial-volume irradiation. These summary reports build on the work of Emami *et al.*[47], who estimated NTCP based on reported patient outcomes and dose-volume parameters including dose-at-volume (for volume level X, dose at volume is DX) and volume-at-dose (volume at dose level X is VX). Simple evaluation metrics which describe 3D-dose on 3D-anatomy can be used to predict NTCP based on observed outcomes.

This work proposes a method of dose evaluation on lung cancer patient anatomy which uses mass rather than volume in evaluation. According to the LQ model, when cell density is proportional to physical density, dose-to-mass should be a more appropriate measure of radiation response in tissue. Dose-to-mass is discussed in Chapter 6.

2.3.1 Organs at Risk

Following the recommendations from the QUANTEC reports, dose-volume levels which indicate non-zero complication probabilities are described for the spinal cord[48], esophagus[49], heart[50], and lungs[51] in the next several sections. Organs are traditionally classified as serial or parallel organs (see, e.g. Chao *et al.*[52]). In serial organs, damage to any part of the structure will result in a loss of functionality of the entire structure. For parallel organs, a percentage of the structure must be damaged in order to lose functionality.

Spinal Cord

Spinal cord is considered a serial organ; the maximum dose to any region of the spinal cord has the potential to cause myelopathy and at high enough doses, paralysis. Based on data from conventional fractionation to the cervical spine, complication probability is 0.03% at *BED* = 45 Gy, or a physical dose of around 50 Gy[48] delivered in 2-Gy fractions. Assessing complication probability to spinal cord in hypo-fractionated therapy of cervical spine is inconclusive, according to the QUANTEC report.[48] However, 4 fractions resulting in a physical dose between 13 and 17 Gy (D_{fx}<4.3 Gy) has complication probability 0.3%±0.3%, based on outcomes from consistent treatments at Medical College of Virginia,[53] Massachusetts General Hospital,[54] and University of Virginia.[55] In these studies, 339 patients were treated to a 2-Gy equivalent BED between 57 and 61 Gy at per fraction doses between 3 and 5 Gy and one patient suffered from grade III myelopathy. In evaluations of spinal cord dose in subsequent chapters, maximum dose (D_{max}) to spinal cord is reported.

Esophagus

The esophagus shows parallel traits at low doses and serial traits at high doses. The most commonly observed effect of irradiation in the esophagus is acute esophagitis; however grade III-V esophageal toxicity is also a concern at high physical doses.[49] There is recent evidence that esophagus NTCP is related to mean structure dose exceeding 28 Gy.[56] Krafft *et al.*[57] indicate a correlation between complication and regional mean dose.[57] The studies of Singh *et al.*[58] and Qaio *et al.*[59] show maximum doses above 60 Gy predict high grade (≥III) esophageal toxicity in 3DCRT. Belderbos *et al.*[60] indicate that dose >35 Gy is a predictor of Grade 2 acute esophagitis from a study with 156 patients, Wei *et al.*[61] indicate volume at 20 Gy (V20) is a predictor of Grade 3 acute esophagitis at volumes exceeding 35% of esophagus based on outcomes from a 215 patient study. Based on these studies, in this dissertation esophagus volume (and mass) is evaluated at 20 Gy and 25 Gy. It is also of interest to note that esophagus motion has been measured between 5-9 mm during respiration, with magnitudes of motion dependent on the anatomic region.[62]

Heart

Heart irradiation has the potential to cause acute pericardial effusion and numerous late effects including congestive heart failure, ischemia, and coronary heart disease.[50] However, these effects are more commonly observed following left breast and lymphoma RT than following lung RT due to lung cancer morbidity, lung-cancer patient demographics, and other factors. Pericardial effusion, based on the studies of Wei *et al.*[61], occurs at pericardium doses >30 Gy. The report of Gagliardi *et al.*[50] shows that heart V25<10% results in <1% probability of cardiac morbidity. The heart is a (relatively) large and massive organ with many complex regions;

however cardiac doses above 30 Gy correlate with both acute (e.g. effusion) and late effects (e.g. cardiac-related morbidity). Heart volume and mass is evaluated in subsequent sections at 20 Gy and 30 Gy.

Lungs

Lung damage due to RT, and the associated symptoms, has proven difficult to describe and quantify. Marks *et al.*[51] specifically mention confounding disease, the physician's preference in prescribing steroids (which is defined as either Grade II or III pneumonitis depending on the protocol), and improved lung function due to tumor regression as confounding factors in recognizing lung damage due to RT. Due to lung-cancer patient mortality, late effects are not quantified. Other confounding issues arise from uncertainty in dose-volume estimates due to challenges in dose estimation in heterogeneous lung tissue and volume variation during respiration.[63] When a (single) planning image is used for dose-evaluation, the phase chosen for lung definition will influence the dose and volumes used to estimate DVH. Despite all of these factors, there is clear evidence that both mean lung dose (MLD) >10 Gy and lung volume >10% at 20 Gy (lung V20>10%) result in non-zero incidence of pneumonitis.[51] In this dissertation, dose to lung is typically evaluated using the V20.

2.4 GEOMETRIC UNCERTAINTY

Fractionated RT requires repeated alignment of the patient in the treatment room with respect to the LINAC. Inaccuracies and imprecision in setting up the patient in the coordinates of the LINAC results in what is termed setup error. Setup error is not considered in this work due to several factors, including inter-institution variability in techniques used to perform the patient

realignment. However, in order to implement the methods described herein clinically, accounting for setup error is necessary. This section briefly describes geometric uncertainty in the context of lung cancer RT.

Set-up error is a combination of random fraction-to-fraction positioning deviations and a systematic offset between the mean position of the treated patient and the patient geometry in planning images. The random and systematic components[64] each have a different effect in the delivered dose distribution, random errors blur the dose distribution, systematic offsets shift the mean location.[65] In order to ensure geometric uncertainty does not compromise dose delivery to the target, setup error is accounted for via the setup margin (SM), a spatial margin designed to encompass possible positions of the actual target and define the PTV.[15] The appropriate size of this margin depends on the magnitudes of both random deviations and systematic uncertainties. Margin formulas for SM often use a summation or quadrature summation of random and systematic components and are often tumor-site specific.[64] One source of systematic error is finite patient representations in simulation images due to discretization of anatomy into finite voxels, these voxels are typically 1-3 mm. Target delineation is also a source of systematic error in geometric uncertainty[66] and is a limiting factor in the elimination of geometric uncertainty.[64] Systematic error can be accounted for through inclusion of an internal margin (IM) in the SM, which is designed to account for delineation uncertainty and anticipated internal-motion not captured in simulation images.[15]

Random errors result in dose blurring and can be estimated through convolution.[67] An on-board imaging device can be used to image the patient in treatment position immediately prior to treatment and reduce random error. This approach is termed image guided RT (IGRT).

Patient alignment and repositioning in IGRT can be performed using bony anatomy or using structures of interest including implanted markers, nearby organs, or the tumor itself.[24,68–71]

Use of IGRT combined with immobilization devices suggests an institution-specific estimate of random error may be more appropriate than using population models.[64] Some examples of implementations include the study of Bissonette et al.[71], who utilized the VacLok immobilization cushion (Civco Medical Solutions, Kalona, IA) and indicated cone-beam CT (CBCT) based IGRT resulted in random and systematic error of 0.4 mm and 1.7 mm, respectively. A recent study by Grills et al.[68] used at least three CBCT scans; two scans to realign and verify realignment, and one scan following treatment, to estimate appropriate setup margins. The lung cancer patients were positioned in either a stereotactic body frame or an alpha-cradle[72] and a 4-parameter model[73] indicated margins between 2.2-2.4 mm medial-lateral, 3.2-5.3 mm anterior-posterior, and 3.9-4.3 mm superior-inferior (with variability based on the immobilization device) were suitable to account for geometric uncertainty due to random and systematic errors. The measured random deviations were less than 1.2 mm pre- and post- treatment using a stereotactic frame, and less than 1.6 mm pre- and post- treatment using the alpha-cradle in all directions.

Purdie et al.[70] also used repeat CBCT and demonstrated that geometric uncertainty was bounded by a Euclidean-norm distance of 5 mm when multiple CBCT images were acquired within 34 minutes of one another.   Beyond 34 minutes, however 6/10 patients showed 3D-norms between tumor points of interest >5 mm. Purdie et al.[70] used a "full-body vacuum pillow" inside of a stereotactic body frame (Elekta Oncology Systems, Stockholm, Sweden),

initially aligning the patient according to tattoos. Their results show alignment to bony anatomy is not an acceptable approach for IGRT of lung cancer.

In this work, for both locally advanced and early-stage lung cancer patients, the moving target is defined as a 3-5 mm of the expansion of the GTV, i.e. the combined microscopic extension of disease and the IM is 3-5 mm, so that CTV=GTV+IM. Due to inter-institution variability in patient immobilization devices, use of on-board imaging for IGRT, and plan design for locally advanced, conventionally fractionated RT; set-up error is not considered in this dissertation, i.e. SM = 0 and PTV=ITV+SM=ITV. Using the convention of Stroom *et al.*[74], the target surrogate is termed the representative target volume (RTV), this is either the CTV or the ITV.

Ideally, all institutions will use immobilization devices, minimize inherent spatial uncertainty, and accurately estimate geometric uncertainty in order to design a SM and ultimately an appropriate RTV. Alternatively, through probabilistic sampling of the actual moving target according to an assumed motion distribution, a PTV-like solution can be designed during plan optimzation.[75,76] Both methods lead to design of an appropriate target surrogate for dose-evaluation based on institution-specific implementation, and one must be used in order to implement the methods described herein clinically.

2.5 RADIOTHERAPY PLAN OPTIMIZATION

With structures defined on the planning image, a set of treatment beams (or continuous arcs) are designed and simulated on the planning image during the treatment planning process. The beam configuration and patient anatomy are input parameters for RT plan optimization. In ideal IMRT optimization, each beamlet, for all beams, is optimized for the patient-specific

anatomy to maximize dose to the target and minimize dose to healthy tissue. In reality, RTP-optimization is most often performed utilizing protocol-defined objectives for targets and OARs based on historical or hypothesized outcome data. The individual objectives are combined, often in a sum of squares formulation, to form a scalar-valued objective function (see, e.g. Wu and Mohan[77]). When the individual objectives of RT are conflicting, i.e. when two objectives trade-off, human interaction is necessary in order to make decisions based on the importance of each objective. The importance (of each objective) is expressed by weighting factors determined by the decision maker (i.e. dosimetrist, physicist, or physician). The weighting factors are assigned arbitrary values in order to achieve a desired result, and weight adjustment redefines the importance of objectives in an optimization problem. Considering this ill-defined specification, a general solution is not realizable.

In general, a compromise must be made in multi-objective optimization problems. The RT multi-objective optimization can be classified by a decision vector of beamlet weightings $\vec{b} \in R^n$, a set of n numeric objectives, f_n, with each objective mapped to an outcome $F_n\left(\vec{b}\right)$. The objective function value should reflect the utility of the combination of outcomes $\left\{F_n\left(\vec{b}\right)\right\}$. The goal of an optimization algorithm is to find the jth decision vector such that the combined utility of n outcomes is preferred to the combined utility of n outcomes resulting from some other decision vector $\vec{b}_{j \neq k}$, or

$$\left\{F_n\left(\vec{b}_j\right)\right\} \succ \left\{F_n\left(\vec{b}_{j \neq k}\right)\right\},$$ where the $\succ$ symbol means preference.

This does not imply that each of the *n* outcomes resulting from $\vec{b}_k$ are preferred to those which result from $\vec{b}_{j \neq k}$, but if the objective (or utility) function obeys stochastic dominance, at least one of the *n* outcomes resulting from the kth decision vector will be strictly preferred to those resulting from $\vec{b}_{j \neq k}$.

The objective function in RT optimization considered in this work is a scalar, weighted sum of least-squares penalty functions. The process of scalarization maps the multi-objective decision problem to a single value. For *N* objectives, the objective function is

$$\hat{O}\left\{F_n\left(\vec{b}\right)\right\} = O\left(\vec{b}\right) = \sum_{n \in N} w_n f_n\left(\vec{b}\right) \qquad\qquad 2.1$$

When trivial weightings are considered (e.g. $w_{n'} = 1$, $w_{n \neq n'} = 0$), a set of decision vectors can be found which optimize individual objectives. When weightings are non-trivial ($w_n \neq 0 \ \forall n$) the value of the scalar objective function does not necessarily relate to clinical value, i.e. a lower objective value does not imply a better plan. However, numerical optimization minimizes the objective function under the assumption that $O\left(\vec{b_j}\right) < O\left(\vec{b_k}\right)$ implies $\vec{b_j} \succ \vec{b_k}$.

In IMRT optimization for lung cancer, the primary objective (often treated as a constraint) is to irradiate the tumor to a tumoricidal dose; other objectives aim to spare healthy tissue including lung, heart, esophagus, and spinal cord. Consider a region of interest (ROI) labeled by the index *n* and represented by a collection of *i* voxels (in the planning image). If each of these ROI voxels has dose $d(i)$ and a prescription or tolerance dose D_n^{Rx} then the objective for this ROI is written

$$f_n\left(d\left(i \in n\right), D_n^{Rx}\right) = f_n = \sum_{i \in n} c_{i,n} \left(d\left(i\right) - D_n^{Rx}\right)^2 \qquad\qquad 2.2$$

The $c_{i,n}$ include Heaviside functions to penalize only voxels with dose above prescription levels (or below prescription in the case of the target) and also include proportionality constants.

The optimization implementation considered in this work is based on the Pinnacle³ ™ TPS (Phillips Medical Systems, Fitchburg WI). The optimizer utilizes the ORBIT objective functions described in Löf.[78] The vector of beamlet weightings which minimizes the objective function is searched via a quasi-Newton method similar to the Broyden-Fletcher-Goldfarb-Shanno (BFGS) method[79] and includes an iterative update of the inverse Hessian,[80] this method is described in more detail in Chapter 5. Once a solution with trade-off consistency between objectives is found, weight variation and re-optimization is performed to satisfy the planner, physicist, and physician to meet the overall goal of treatment. This 2-step process (a numerical optimization and planner adjustment) continues until a solution is deemed acceptable. This process is named the planning-loop, displayed in Figure 5.

In the numerical optimization stage, for many treatment planning systems, dose is calculated on the planning image, the geometric relationship between target and OAR voxels determines beamlet preferences, and the objective function is minimized. In the planner (or human) step, weight variation allows adjustment of the optimized plan and, in some cases, additional objectives are added. With new weights and possibly new objectives, a numerical re-
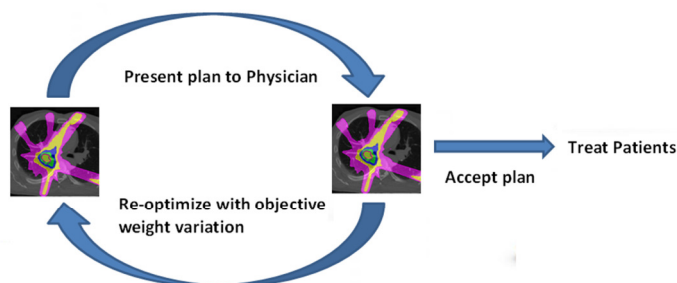
Figure 5. The planning loop requires numerical optimization in order to meet the physician's intent and may require several re-optimizations before accepted by the physician.

optimization is performed; this planning loop continues until a plan is deemed acceptable. This time-consuming process results in arbitrary variations in plan quality depending on institution-specific variables.

Use of fixed OAR objectives (e.g. Lung V20<30% or Esophagus D_{max}<60 Gy) results in no penalty for treating normal tissue up to the anticipated tolerance levels (e.g. there is no penalty for treating lung V20 to 29.9% or esophagus maximum dose to 59.9 Gy). By utilizing population data to estimate NTCP and guide optimization, the therapeutic ratio is not ensured to be maximized for individual patients. This is a departure from the basic goal of radiotherapy, and is investigated in Chapter 7.

Chapter 7 discusses methods to improve on plans which utilize fixed optimization objectives by minimization in order to approximate Pareto efficiency. Named for renowned economist Vilfredo Pareto, Pareto efficiency[81,82] means individual objectives cannot be further improved without a corresponding degradation to one or more other objectives. This approach is explored using multi-criteria optimization (MCO).[83] By pre-computing plans which minimize OAR objectives based on variable objective weights, MCO allows real-time planning and decision making without numerical re-optimization in the planning loop.

2.6 PATIENT COHORT

In this dissertation, a total of fifteen lung cancer patients are included in related publications

and manuscripts. The group includes
ten locally advanced (LA), non-small
cell lung cancer (NSCLC) patients and
five early stage, SBRT patients. All
patients were part of internal review
board-approved studies of lung
cancer RT at Virginia Commonwealth
University (HM-10395, HM-12533).

The LA patients (named P1-P10)
include moderate CTV motion, with
3D-norms ranging from 0.29 – 0.95
cm. Treatment plans did not include
lymph nodes. The SBRT patients (N1-

N5) include cases with 3D- motion
ranging from 0.18 cm to 1.4 cm
including 1 patient (N1) which was

Patient	Tumor Centroid Motion (cm)			ITV (cm^3)	Ratio (GTV/ITV)
(IMRT)	AP	LAT	SI		
P1	0.15	0.07	0.24	221.5	0.83
P2	0.21	0.13	0.22	294.8	0.89
P3	0.21	0.28	0.17	401.8	0.84
P4	0.08	0.24	0.31	60.2	0.78
P5	0.16	0.19	0.43	174.6	0.70
P6	0.08	0.07	0.57	174.4	0.81
P7	0.30	0.41	0.41	232.6	0.70
P8	0.32	0.25	0.56	105.1	0.80
P9	0.44	0.15	0.61	173.1	0.79
P10	0.36	0.16	0.86	442.4	0.82
(SBRT)					
N1*	0.07	0.11	0.41	56.5	0.89
N2	0.30	0.14	0.48	18.2	0.70
N3	0.12	0.10	0.03	35.2	0.97
N4	0.23	0.17	1.17	12.5	0.67
N5	0.15	0.19	1.52	83.8	0.62

Table 1. Patient Details. *This is a gated internal target volume (ITV) including only the 30% -70% phase-based GTVs.

treated using RT-gating. A few patient details are detailed in Table 1. The clinically delivered

plans were evaluated for the early stage patients considered.

3   Specific Aims

The aims of this dissertation are detailed in this chapter. The goal of these aims is to implement

and develop techniques which, when clinically implemented and applied to patient treatment,

have the potential to improve the therapeutic ratio of radiation therapy for time-dependent

anatomy. The aims specifically address elements of RT for lung cancer treatment including

dose estimation, plan and structure evaluation, and plan optimization.

3.1   AIM 1: MULTIPLE ANATOMY OPTIMIZATION (MAO)

The first aim of this study is to show that RT for time-dependent anatomy can be improved

through inclusion of all phase images from a 4DCT simulation, as opposed to using a single

planning image in the beam optimization. Specifically, Chapter 4 compares dose estimated on

entire 4DCT data-sets with dose estimated on individual planning images. Chapter 5 compares

plan optimization based on a single planning image with multiple anatomy optimization (MAO),

a method which utilizes the entire set of 4D-images in plan design.

Dose estimation is a fundamental requirement of modern RT planning. Differences between

planning image dose and accumulated dose delivered to time-dependent anatomy (based on

4DCT image-sets) are reported for the patient data-sets and motivate implementation of MAO.

The robustness of target dose due to interplay effects between patient breathing and inevitable phase-weight variations due to finite delivery time is also considered.

Unlike gating, breath-hold, and target tracking methods, which also have the potential to increase the therapeutic ratio compared to ITV planning, MAO is designed to be delivered under free-breathing conditions. Hence, MAO can be clinically implemented without additional complications inherent in solutions which require monitoring or control of patient breathing. MAO has the potential to generate a plan which is superior to single-image (3D) clinical plans in terms of dose accuracy, precision (or robustness), and can be delivered with current, conventional RT hardware. MAO and ITV plans are compared in Chapter 5 for ten locally advanced lung cancer patients.

3.2   AIM 2: DOSE TO MASS IN EVALUATION AND OPTIMIZATION

The second aim of this dissertation is to utilize mass-based metrics in radiation therapy plan evaluation and plan design, as opposed to using volume-based metrics. Structure mass is considered in the context of delineation consistency, dose-evaluation, and RT plan optimization in Chapter 6.

While structure volumes can physically vary in different respiratory phases, structure mass is constant. If structures delineated on 4DCT phase images are accurate representations of physical anatomy, then each structure mass should be constant as a function of respiratory phase. Inter-phase mass conservation of structures is evaluated in Chapter 6 based on physician-delineated and deformably-registered structures. Mass-variation over the course of treatment is also considered for one patient in Chapter 6.

Volume and density variations during respiration introduce ambiguity in dose evaluation for lung cancer anatomy. Evaluation of dose-to-mass, as opposed to dose-to-volume, will reduce this ambiguity and may be more closely related to the physical effects of radiation in tissues. Dose-to-structure volume and the DVH are compared to dose-to-structure mass and the dose mass histogram (DMH) in Chapter 6. DMH plots (relative) structure mass as a function of dose. DMH is a more appropriate evaluation of dose on mobile, heterogeneous structures.

Treatment plans are optimized based on DMH levels in Chapter 6. Using single-image, ITV-plans, optimized dose distributions are compared based on DVH- and DMH- objectives for eight locally advanced patients. Mass-based optimization (DMH-optimization) is essentially a functional optimization which assumes voxel importance is determined from the planning-image density. The validity of mass as a surrogate for voxel importance is also discussed.

3.3 AIM 3: TOWARD PARETO-EFFICIENT RADIOTHERAPY PLANNING

Aim 3 of this dissertation is to improve plan design and design-efficiency in RT plan optimization. This aim is addressed using multi-criteria optimization (MCO) and a pre-computed set of basis plans. Decision making is clarified by permitting rapid identification of conflicting objectives. Patient- and objective- specific variations are incorporated in plan design without the numerical re-optimization stage of the planning-loop by interpolating the MCO basis-set. Different MCO-bases, optimized based on different OAR-objectives, are also compared. Because MCO enables plan browsing in real time, the effects of delivering the plan to time-dependent anatomy can be analyzed during plan-selection without numerical re-

optimization. An application of MCO which allows for a clear decision environment for

radiation therapy of locally advanced lung cancer is developed in Chapter 7.

4   Dose Estimation in Time-Dependent Anatomy

Chapter 3 list of abbreviations:

3DD – 3D-dose

4DD – 4D-dose or accumulated dose

DIR – deformable image registration

DVF – deformation vector field

ETM – energy transfer method

w_p – anatomic phase weighting

D_p^a – dose to phase p due to aperture a

D_p^b - dose to phase p due to beam b

MU – monitor unit

MU_b – monitor unit per beam

DR – dose rate

N_p – number of phases

The first aim of this study is to show that dose estimation and plan optimization for RT in time-dependent anatomy can be improved through inclusion of all of the respiratory phase images acquired during 4DCT simulation. This chapter focuses on dose-estimation.

In current clinical practice, a single planning image is often used for dose computation in lung cancer radiation therapy despite widespread availability of 4DCT images. The total

(accumulated) dose delivered to moving anatomy may deviate from this single image estimate which allows for the possibility of inaccuracies in plan evaluation and optimization when using a single image for dose estimation. Following a brief introduction to dose computation and dose accumulation, differences between single image dose and accumulated dose are reported in this chapter.

Dose computed on a single image is termed 3D-dose (3DD). Clinical use of 3DD assumes the simulated dose is approximately independent of 4D-anatomic phase (i.e. the patient anatomy may change in time but the dose cloud is static) and delineated structures are independent of phase (i.e. a single contour is sufficient to represent a moving and deforming structure). Accumulated dose, or 4D-dose (4DD), computes 3DD on several anatomic images followed by accumulation. Accumulation is a dose summation after transformation to a common reference phase. The images and transformations are assumed to be true representations of the patient anatomy and motion. This assumption ignores uncertainty in the 4DD resulting from errors in the spatial transformations and from errors introduced by the method of dose accumulation, which is also discussed in this chapter.

The methods and results of submitted and published manuscripts which describe 3DD and 4DD differences are detailed in this chapter. Appendix A compares 3DD and 4DD for relevant structures in lung cancer anatomy for ten locally advanced patients. Appendix B focuses on the moving lung cancer target and shows that for a given patient, plan, and evaluation metric (e.g. DVH values or *gEUD*), 3DD can deviate from 4DD in the target. These studies imply evaluation of 4DD is necessary in assessment of dose to moving anatomy.

Finally, this chapter considers the effects of finite delivery time and patient specific breathing on 4DD. Potential deviations between the realized anatomy during each fraction and the anatomy recorded in 4DCT are reported, together with target dose variability resulting from these anatomic variations. In appendices A and C, 4DD variations are reported due to finite delivery time and patient-specific breathing for locally advanced patients (Appendix A) and for early stage SBRT patients (Appendix C).

4.1 COMPARING SINGLE IMAGE, 3D-DOSE AND ACCUMULATED, 4D-DOSE

Evaluation of dose to a moving, 4D tumor (or target) can be estimated by assessing dose to a larger, static structure which encompasses all possible tumor locations. This is a common method used in radiation therapy to account for set-up error. Treating the PTV to uniform prescription dose, assuming approximate conservation of anatomic mass along radiation path-lengths (or buildup) on different days of treatment, assures the target is also treated to a uniform dose. The tumor location varies during each fraction according to random and systematic geometric deviations from the planned tumor location, but always exists within the PTV. In this case, the PTV is the representative target volume (RTV) of the actual, moving target. Treating the entire PTV to a uniform dose, however, necessitates treating normal tissues to prescription dose. Furthermore, if prescription dose is not uniform in the PTV and/or mass and energy are not conserved in different realized anatomies, there is no assurance that the target will absorb the prescription dose without knowledge of the probability distribution of the target within the PTV. In this case, an estimate of accumulated dose, or 4DD, may be necessary.

4.1.1 Accounting for Geometric Uncertainty in Accumulated Dose

In order to evaluate 4DD on a moving lung cancer target while also accounting for setup uncertainty, the moving lung cancer target should be expanded by a setup margin (SM). This margin may be consistent with the SM used in ITV-PTV expansions, assuming the random and systematic components of setup error for the moving target and the ITV are equal. For example, if a 5 mm SM is applied to the ITV to account for random and systematic deviations in setting up the patient, then a 5 mm margin should also be applied to the moving target in 4DD evaluation in order to create an appropriate RTV. Dosimetric margins designed to specifically account for 3DD and 4DD differences (see, e.g. Hugo *et al.*[84]), however, do not need to be included in the RTV.

Admiraal *et al.*[85] compared 3DD and 4DD for ITV plans designed with zero PTV margin, i.e. PTV=ITV, RTV=CTV. For the ten SBRT patients considered, minimum dose to the moving target was consistent with the minimum PTV-3DD. Admiraal *et al.*[85] claimed the use of identical margins on the ITV and CTV in 3D- and 4D- dose estimation was a "worse-case scenario;" however, this scenario accounted for setup error in the actual, moving lung cancer target consistently with setup error in the ITV. Inclusion of systematic geometric uncertainty due to deformable image registration (DIR), discussed briefly in the next section, implies the RTV may require a safety margin different from the ITV-PTV margin.

Many published studies compare planned PTV-3DD (3D-dose to the PTV) to CTV-4DD (where the CTV is the moving target) without consideration of geometric uncertainty on the CTV.[86–93] For example, Guckenberger *et al.*[90] used a 0.5 cm ITV-PTV margin in SBRT treatment for early

stage lung cancer and reported no significant differences between the PTV-3DD and GTV-4DD for 7 patients. Rosu et al.[91] evaluated CTV-4DD in 3DCRT using a 1-cm ITV-PTV margin and show point doses can vary by >10% between 3DD and 4DD in the CTV, but differences in evaluation metrics such as *gEUD* may not be significant.

In estimating point doses in lung cancer anatomy, many studies suggest the differences in 3DD and 4DD may be significant to clinical outcomes.[93–96] In 7/15 patients presented by Starkschall et al.[93], dose to 99% of the CTV (CTV-D99) in 3D- and 4D- estimates differed by >3% of prescription. Two ITV-PTV margins were designed on different patients; the ITV was expanded by 0.5 cm if IGRT was used for patient positioning and by 1.0 cm if IGRT was not used. The patients planned with each margin method were not identified and the ITV-PTV margin was not correlated to 3DD-4DD differences as part of the published study. In physical measurement studies, which potentially include setup error, Vinogradskiy et al.[94] reported 4DD passing rates of measured dose using 5%, 3 mm-gamma criteria which were 8%-16% lower than the corresponding 3DD (static) passing rate. Berbeco et al.[95] conclude "there is the possibility of underdosing the tumor by several percent" based on film measurements of IMRT fields delivered on a mobile phantom.

For the locally advanced patients considered, simulation studies are performed without consideration of setup error in PTV definition (SM=0, PTV=ITV). Therefore, consistent with the study of Admiraal et al.[85], estimates of 4DD to the moving lung cancer target do not consider setup error. The reported CTV-4DD use SM=0 cm, consistent with the SM used to define the PTVs in the simulation studies. In analysis of SBRT patient images, the clinically delivered dose distribution is evaluated. The target surrogate (or RTV) for these five patients is a 0.3-0.5 cm

expansion of the GTV (RTV=GTV+0.3 cm or RTV=GTV+0.5 cm) consistent with the ITV-PTV expansion used for each patient.

4.1.2 Deformable Image Registration and Dose Accumulation

The 4DD estimates in this dissertation and in related publications are weighted sums of individual phase-doses computed on ten 4DCT breathing phase images. Prior to summation, the phase-image doses are transformed to a common reference phase (designated by *ref*). The transformations are calculated according to deformable vector fields (DVFs) defined at voxel indices in the *ref* image to corresponding points in each of the other 9 phase images. DVFs are calculated using deformable image registration (DIR). Figure 6 is a graphical representation of DIR for accumulation of dose at a single point (labeled by A); this common anatomic point is mapped from spatial positions in several images. The DVF is a collection of these vectors which map anatomic voxel positions in one image to their positions in another image.

The DIR algorithm used in this work is a variant of the Demons algorithm introduced by Thirion.[97] The algorithm is implemented in the Insight Tool Kit[98] which has been integrated in a research version of the Pinnacle[3] TPS (version 9.100). The implementation of the Demons algorithm is described in Vercauteren[99] and Dru and Vercauteren.[100] In summary, the method minimizes differences between image intensity in the log domain and includes Gaussian regularization to generate smooth DVF vector fields.
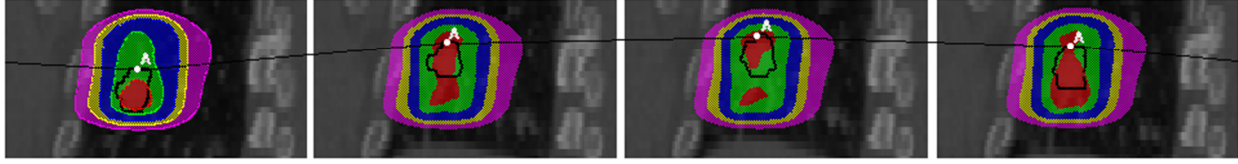
Figure 6. Deformable image registration (DIR) creates deformation vector fields (DVFs). A single vector is shown as the line between images, the vector maps a common anatomic point or dose point (point A) from different images.

For dose calculated on 4DCT-phase p labeled by D_p with a weight w_p (which is normalized so that $\sum_p w_p = 1$), and a DVF vector which maps a point at position $\vec{r}$ defined in the designated *ref* image to a point $\vec{r}\,' = \vec{r} + \vec{v}_{ref \to p}(\vec{r})$ in phase-image p. The accumulated dose is estimated:

$$4DD_{ref}(\vec{r}) = \sum_p w_p D_p\left(\vec{r} + \vec{v}_{ref \to p}(\vec{r})\right) \qquad\qquad 4.1$$

This approach interpolates phase doses (D_p) at vector positions $\left(\vec{r} + \vec{v}_{ref \to p}(\vec{r})\right)$ and is used in all reported 4DD estimates in this dissertation and related manuscripts. For purposes of comparison, this value of 4DD is assumed to be the ground truth value of dose to moving and deforming anatomy. Interpolation of dose as presented, however, can introduce errors in the accumulated dose due to inconsistent summation of the ratio of energy deposited in voxel mass when using interpolation. Siebers and Zhong[101] presented a Monte Carlo-based dose calculation algorithm, the energy transfer method (ETM), in order to more accurately consider energy deposition in mass for accumulation. Another Monte-Carlo-based method of estimating 4DD was presented by Heath *et al.*[102] in which a voxel-warping method was used to calculate volume overlap between deformed reference voxels. Dose was accumulated via scoring in tetrahedral voxels. Heath *et al.*[92] compared a voxel-warping approach to ETM and

demonstrated equivalence when the DVF is exactly known. However, when the DVF fails to conserve mass between the reference and phase image, the 4DD resulting from each method will deviate. Yan et al.[103] show, for mass conserving image pairs, that a similar method can be used to identify errors in the corresponding DVF.

Estimating DVF errors and uncertainty is outside the scope of this dissertation, but sufficiently accurate DVFs so as to not introduce clinically significant dose errors is a precondition of clinical implementation for many of the techniques described herein. Analogous to the inclusion of systematic delineation error in the RTV, uncertainty in target definition due to DIR errors must also be included in the definition of the target when evaluating 4DD. If this systematic uncertainty is not included in target definition, the 4DD estimate of dose may not be a reliable surrogate of actual dose received by the target. The utility of DIR for clinical implementation of the methods presented herein will be determined by the algorithm's ability to delineate time-dependent targets and normal structures accurately and efficiently as compared to physician delineation. As discussed in Chapter 6, consideration of structure mass is one method to compare DIR- and physician- defined structures.

In evaluation of 4DD in this work and in related publications, the uncertainty in target definition, defined by either an expert physician or by the Demons DIR algorithm, is accounted for by a 0.5 cm expansion of the GTV. In this work, for locally advanced patients, RTV = CTV = GTV + 0.5 cm. This 0.5 cm margin is designed to include microscopic extension of the GTV, internal margin (IM), and delineation uncertainty due to either physician contouring or due to DVF errors. This 0.5 cm margin may be a reasonable estimate if microscopic extension

is, e.g. 0.4 cm, delineation uncertainty is 0.2 cm, and IM is 0.2 cm ($\sqrt{0.4^2 + 0.2^2 + 0.2^2} = 0.5$ cm). However, uncertainty in physician delineated structures and structures defined according to DIR may not be equivalent.

4.2   COMPARISON OF SINGLE IMAGE, 3D-DOSE AND ACCUMULATED DOSE

In the following section, differences between 3DD and 4DD for the patient cohort are reported. The 3DD is estimated on different planning images including the aCT-image, the inhale phase image (00%), and a mid-ventilation phase images (30%) for the LA patients. 3DD and 4DD are compared to the clinically delivered, SBRT plan for the early-stage patients. The 4DD is calculated according to eq. 4.1 and evaluated on either the inhale or exhale 4DCT phase. Mean differences and standard deviations about the mean are tested for significance using the students t-test with probability of rejecting the null hypothesis at a 5% confidence interval.

4.2.1   Results: Locally Advanced Patients

Three dimensional, ITV-plans are optimized based on the aCT-image, the inhale phase image (00%), and mid-ventilation phase images (30%) to create three plans for each of the ten LA patients. Dose voxels are 0.3x0.3x0.3 cm^3 and cover the entirety of the lungs. Following plan optimization, 3DD is computed on each of the other 9 phase images and dose is accumulated to the inhale phase image to estimate 4DD. The 4DD is evaluated on physician-defined structures on the inhale phase. 3DD and 4DD differences are summarized, based on the results of Appendix A.

Mean dose differences between 3DD and 4DD (i.e. <3DD> - <4DD>) for lung, esophagus, and heart are less than 1 Gy for 116 of 120 estimates (10 patients x 3 plans x 4 OARs) and relative OAR volume differences at fixed 3DD and 4DD, and maximum dose (D_{max}) to the spinal cord differ by less than 3% in 147/150 estimates. The range of volume differences in ipsilateral lung V20 is -3.2% to 3.5%, in contralateral lung V20 is -2.1% to 3.5%, in esophagus V25 is -0.2% to 1.3%, and in heart V30 is -3.2% to 1.2%. These findings suggest that dose-volume estimates to time-dependent OARs can be approximated to within ±3% from single image, 3DD estimates independently of planning image. Starkschall *et al.*[93] found similar results (i.e. small 3DD-4DD differences) for OARs in a 15 patient study, with the exception of spinal cord D_{max} in 2/15 cases.

Comparing 3DD and 4DD for the lung cancer target (the CTV), 3DD-4DD>0 in 28/30 estimates. The range of mean dose differences between 3DD and 4DD in the CTV is -0.1 to 1.8 Gy ($p=10^{-7}$) with 3DD-4DD >1.7 Gy in 2 of 30 estimates. Target mean dose differences between 3DD and 4DD are independent of the ITV-planning image, with a mean difference of 0.5 Gy for plans on both 0% phase (± 0.4 Gy, $p=0.002$) and 30% phase (± 0.4 Gy, $p=0.007$), and 0.7 Gy ± 0.4 Gy ($p=0.001$) when planned on the aCT. Figure 7 shows estimated dose differences between 3DD and 4DD for the ten locally advanced patients for the CTV-target and OARs. It can be visually verified from the figure that OAR 3DD-4DD are small compared to the CTV 3DD-4DD, which also shows a consistent trend of 3DD > 4DD.
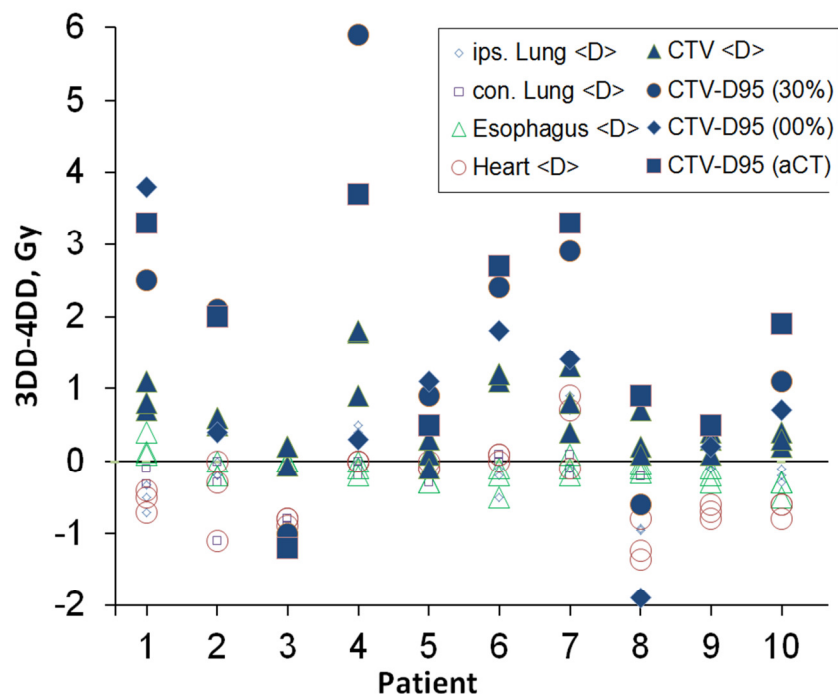
Figure 7. Dose differences between 3D- and 4D- dose for ten locally advanced patients. The 3D-dose is calculated on three different planning images, the 4D-dose is computed according to equation 4.1 and accumulated to the inhale phase image.

For dose-volume comparisons, including dose to 95% of the CTV (CTV-D_{95}) and CTV-volume at 70 Gy (CTV-V70), 3DD systematically overestimates the 4DD in the cases considered. The differences exceed 2.1 Gy (or 3% of prescription) for at least one plan for 4/10 patients. Average differences in CTV-V70 = 3.4% ± 4.9% ($p=10^{-4}$) and are independent of the planning image ($p > 0.2$ in all comparisons of the difference distributions). Correlations between the difference in 3DD and 4DD and 3D-motion of the CTV are not evident ($r^2 = 0.002$), nor is CTV to ITV ratio an indicator 3DD-4DD differences ($r^2 = 0.124$). These differences indicate that the CTV-3DD is not an appropriate surrogate of CTV-4DD.

The purpose of planning dose to the PTV is to ensure the moving target receives the prescription dose. In 27/30 plans considered, PTV-3DD$_{95}$ > CTV-4DD$_{95}$. The CTV-4DD$_{95}$ is less than PTV-3DD$_{95}$ by 0.51 Gy in the aCT plan of P1, by 1.08 Gy on the aCT plan of P4, and by 0.54

on the 30% plan for P7. The range of differences between PTV-3DD$_{95}$ and CTV-4DD$_{95}$ is -5.39 Gy to 1.08 Gy, with magnitude of differences >3% of prescription in 19/30 plans. The difference distributions of PTV-3DD$_{95}$ and CTV-4DD$_{95}$ are significantly different from zero, with average, standard deviation, and probability of rejecting the null hypothesis of -3.05±1.82 Gy, $p=5 \times 10^{-4}$ when planning on the 30% phase, -1.47±1.87 Gy, $p=0.03$ when planning on the aCT image, and -2.23±1.60 Gy, $p=0.002$ when planning on the inhale phase image. Figure 8 shows the PTV-3DD$_{95}$ for each plan, compared the CTV-4DD$_{95}$.
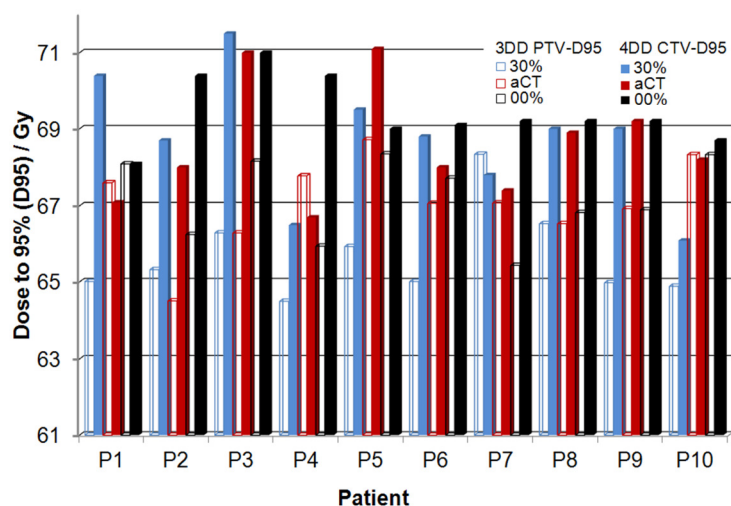
Figure 8. Dose to 95% of PTV based on the planning image 3D-dose, and accumulated dose (4DD) to the moving CTV based on ITV-plans optimized on the 30% phase image, on the average CT (aCT) image, and on the 00% phase image.

Appendix B discusses 3D- and 4D- dose differences for five of the LA patients planned with the ITV-method on aCT and 30%-phase images including comparison of biologic metrics such as gEUD[45] evaluated on the moving target (the CTV) and the PTV. Differences between CTV- 3DD and 4DD for gEUD($a=-5$) (corresponding to a radiosensitive target) range from -6.5 Gy to 3.8 Gy. For $a=-20$, representing an aggressive tumor, 3D- and 4D- differences in CTV range from -3.9 Gy to 9.6 Gy. Appendix B also shows that planning on the aCT decreases 3DD-4DD gEUD differences compared to plans designed on the mid-ventilation image in 12 of 15 CTV-gEUD estimates.

4.2.2   Results: SBRT Patients

Clinically planned and delivered SBRT dose distributions are compared to accumulated, 4DD for

five early stage patients in Appendix C. In all cases considered, the clinically planned target

differed from the ITV defined as the union of phase-based GTVs, which invalidates the PTV

surrogate for target coverage. In two cases, a MIP image was used to define the target; in

another case a single phase-image was used to define the target. Figure 9 shows the clinically

planned PTV, defined as a uniform expansion of a target defined in a MIP image, and the PTV

defined as a union of phase-based GTVs with a 0.5 cm expansion. Target evaluation in this

dissertation is always carried out on the PTV defined as a 0.3-0.5 cm expansion of the ITV

(defined as a union of phase-based GTVs); where the SM expansion is selected in order to

closely match the clinically planned PTV.
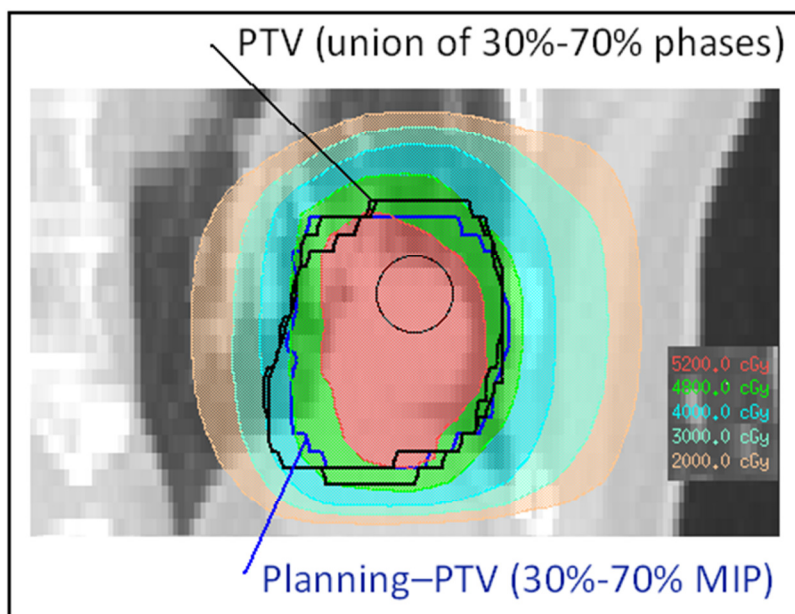
Figure 9. A coronal slice of patient N1 showing contour differences between the planning target volumes (PTV) defined in three different ways. The planning image contour is defined on a MIP image (blue); the PTV defined as an expansion of the ITV is shown in black for physician and DIR-based GTV contours.

The target RTV is defined as the exhale-phase GTV expanded by 3-5 mm and is designated the CTV. Figure 10 shows the 3DD PTV-D$_{95}$, 3DD CTV-D$_{95}$, and 4DD CTV-D$_{95}$. In all five patient cases considered, the 3DD CTV-D$_{95}$ is within 1 Gy of the 4DD CTV-D$_{95}$ and the PTV-3DD$_{95}$ > CTV-4DD$_{95}$. For OARs, the differences in dose and volume at dose are shown in Figure 10. Similar to the locally advanced cases, differences between OAR structure volumes evaluated at 3DD and 4DD is less than 3% in all estimates. The only difference of note is the spinal cord D_{max} for N2, for which the 4DD$_{max}$ is greater than the 3DD$_{max}$ by 1.8 Gy; however both doses are less than 5 Gy which are not significant cord complications.
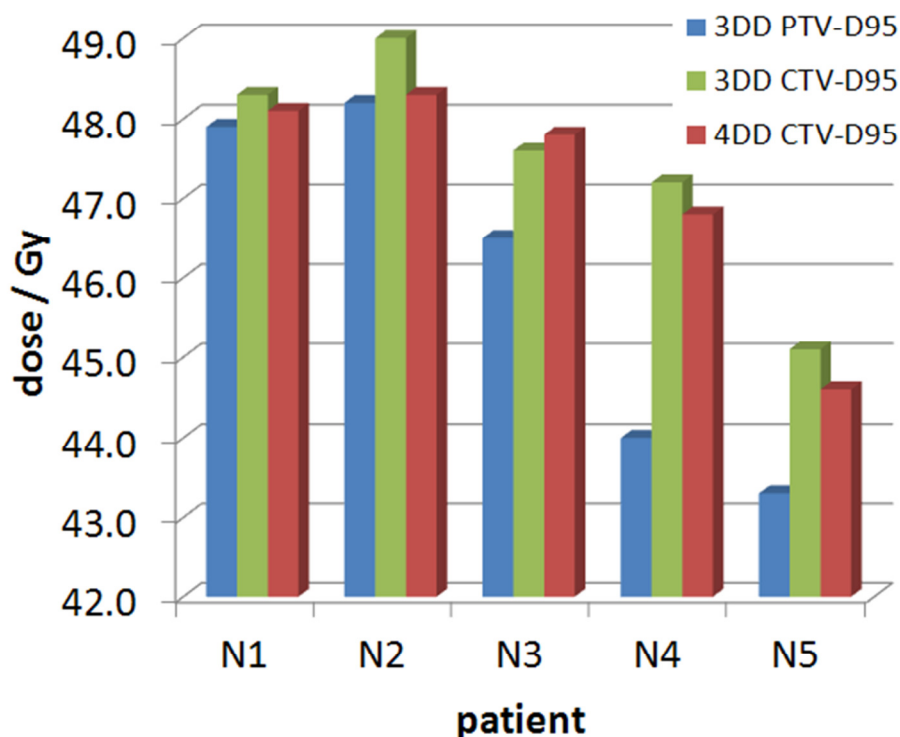
Figure 10. Dose to 95% of the PTV and CTV, based on 3D- and 4D- estimates for the early stage SBRT patients. Neither the 3D- estimate of CTV-D$_{95}$ nor the PTV-D$_{95}$ are reliable surrogates for dose to the moving CTV.

Table 2 Planned, single image 3D-dose (3DD) compared to accumulated, 4D-dose (4DD) for organs at risk for five early stage SBRT lung cancer plans.

Patient:	N1		N2		N3		N4		N5	
	3DD	4DD	3DD	4DD	3DD	4DD	3DD	4DD	3DD	4DD
spinal cord (max. Gy)	7.38	7.38	3.2	5.0	6.3	6.7	6.8	6.8	10.5	10.2
Ips. lung (V10)	0.23	0.24	0.26	0.27	0.23	0.23	0.18	0.18	0.26	0.26
con. Lung (v5)	0.02	0.02	0.01	0.01	0.06	0.06	0.01	0.01	0.19	0.2
heart (V5)	0.25	0.23	0.34	0.34	0	0	0.12	0.11	0.53	0.5
Esophagus (V5)	0.18	0.18	0.17	0.19	0.18	0.21	0.02	0.01	0.37	0.39

The CTV-4DD$_{95}$ is consistently greater than the planning dose to the PTV in the cases considered, but is less than the CTV-3DD$_{95}$ by in 4/5 cases (maximum of 0.7 Gy difference, or <1.5% of prescription).

4.2.3 Summary: 3D- and 4D- Dose

Consistent with ICRU-62,[15] coverage of a designated target surrogate, e.g. the PTV, should ensure coverage to the actual target. It is shown in Appendix A and B that the relationship between dose to the moving lung cancer target and dose to the target surrogate (the PTV) is not obvious, and is patient and plan-dependent. For different plans and planning images, the dose to the moving target can be greater than, less than, or equal to the PTV dose. According to the results of this dissertation, under-dosing 95% volume of the moving lung cancer tumor is not likely, but is possible. Increasing D95 of the moving target by values >2.5% of the 3DD PTV-D95 surrogate, however, is likely to occur. This was observed in 19/30 LA plans and 3/5 SBRT plans evaluated.

The observed under-dosing of the moving target in the LA plans, compared to the PTV, appears to violate the premise of ITV planning; that a uniform dose to the ITV will also ensure a uniform dose to the moving target. However, the dosimetric tolerance in the (larger) target surrogate allows for the possibility of under-dosing the CTV. Reducing dose in the PTV through prescribing to 95% of the PTV volume, rather than prescribing to a minimum dose, enables reduction in surrounding OAR dose and reduces the volume of normal tissue at prescription. However, the volume of the PTV is larger than the volume of the moving CTV, so that 5% tolerance in the PTV could result in a relatively larger cold-spot in the actual moving target, depending on the time the target resides in each region of the PTV.

Figure 11 shows a motion-probability density function (PDF) for the breathing pattern of patient P1. The marker moves a total of 1.8 cm, but spends about twice as much time in the spatial region near 1.4 cm (which corresponds with end-of exhale,
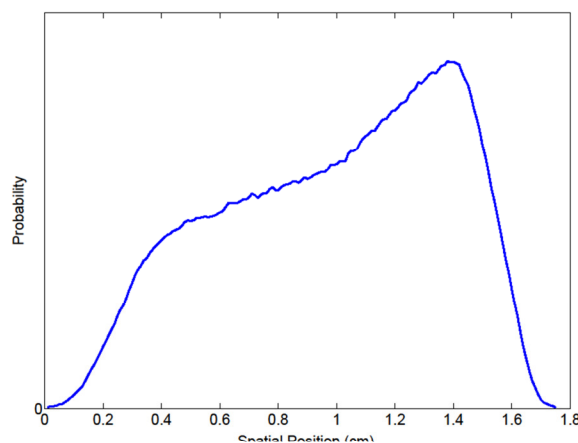
Figure 11. A probability density function of a patient breathing pattern. An ITV-optimized dose distribution assumes this PDF is uniform across all spatial positions.

50% phase) than the region near 0.4 cm (near the end-of-inhale, 00% phase). If the ITV plan under-doses a spatial region of high probability (e.g. near 1.4 cm), CTV coverage may be compromised. Because an ITV-plan assumes a uniform distribution of the target within the ITV, it cannot take advantage of a region of low/high probability and may be susceptible to 3DD/4DD dose differences. However, minimum dose to a moving target can be estimated by

single image, 3D calculations if two conditions are met: (1) approximate conservation of mass between the planning image density and patient density on the day of treatment; and (2) the entire ITV region is treated to the minimum dose.

The hypothesis of ITV planning, that a minimum dose to the ITV will ensure minimum dose to the PTV, is confirmed in the SBRT cases examined. However, the LA, ITV-plans show under-dosing the moving CTV is possible, but not likely, when the PTV is not treated to a minimum dose. If a PTV cold-spot coincides with a region of high probability for the CTV, the CTV can be under-dosed. Far more likely, according to the results of Appendices A, B, and C, is delivering a higher dose to the CTV than indicated by the PTV-dose. The deviations in the delivered target dose will propagate into uncertainty among lung cancer outcome studies which aim to tie a dose-level to local control or survival. In OARs, however, for both LA and early stage patients, 3DD-4DD differences are small. OAR volumes at fixed 3DD and 4DD differ by less than 3.5% in all cases considered.

Dose estimated according to equation 4.1 assumes the anatomic weightings per phase are independent of finite delivery time and that the distribution of 4DCT phases realized during treatment is identical to what is sampled at the time of simulation. This may be a reasonable estimate for fractionated therapy with a consistent breathing pattern, where patient breathing is sufficiently sampled to reproduce anatomy which matches the distribution recorded during 4DCT simulation. However, unless the beam-on time is correlated to the breathing pattern, the equi-weighted phases will never be realized in each individual fraction. Methods to estimate the effects of finite delivery time on accumulated dose are investigated in the following sections.

4.3   SAMPLING 4D-ANATOMY BASED ON FINITE DELIVERY TIME AND PATIENT-SPECIFIC BREATHING

In order to estimate the accumulated dose (4DD) in equation 4.1, an estimate of the probability of treating each phase image (w_p) is required. Equation 4.1 assumes the phase (or anatomic) weights are independent of finite delivery time. By estimating the dose distribution and anatomic weightings for each aperture (or collection of beamlets), the effects of finite-delivery time on dose can be estimated prospectively. This effect is commonly called the interplay effect, i.e. the effect of interplay between anatomic motion and non-uniform dose delivery. Physical measurements of dose to a moving dosimeter (dose detector) allows for estimation of the interplay effect (see e.g. Jiang *et al.*[104] or Berbeco *et al.*[95]). For a fixed aperture sampling rate, previous studies have used MLC-logged output and exit-fluence measurement to estimate dose to time dependent anatomy retrospectively[105–107] and prospectively.[107,108] Based on measurement and simulation, the effects of MLC interplay have been shown to have a negligible effect on the total dose due to fractionated sampling.[104,109] However, the magnitude of this effect is dependent on several factors including the dose distribution, the dose-rate, the fractionation schedule, and delivery techniques (e.g. dynamic MLC motion, step-and-shoot MLC delivery, etc).[110,111]

In order to estimate 4DD and variability in 4DD due to the effects of fractionated delivery, patient breathing, and delivery conditions (including dose-rate and optimized monitor units), plausible sampling of the patient anatomy is investigated in this section. Dose to anatomic phase *p* due to aperture *a* is designated D_p^a and is weighted by a sampled probability of w_p^a.

4DD can be estimated as:

$$4DD_{ref}(\vec{r}) = \sum_{a}\sum_{p} w_p^a D_p^a \left(\vec{r} + v_{ref \to p}(\vec{r})\right) \qquad\qquad 4.2$$

In appendices A and C, 4DD is estimated including the effects of finite beam-on time and non-uniform delivery on a per-beam basis, not on a per-aperture basis. A per-aperture sampling of anatomic phase weights and a per-aperture dose calculation, as in equation 4.2, in addition to the effect of finite delivery time and non-uniform delivery, will estimate the interplay effect between MLC motion and anatomic motion. However, interplay between MLC and anatomic motion is beyond the scope of the current work. Such an estimate must also consider the MLC motion sequence (or the order or apertures) which delivers each optimized beam fluence.[111]

Estimating 4DD on a per-beam basis assumes the collections of apertures which compose each beam are realized for the entirety of each beam-on time. The 4DD, in this section, is estimated as a sum of deformed doses per-beam b, per phase p (D_p^b), with phase-weightings w_p^b according to

$$4DD_{ref}(\vec{r}) = \sum_{b}\sum_{p} w_p^b D_p^b \left(\vec{r} + v_{ref \to p}(\vec{r})\right) \qquad\qquad 4.3$$

The difference between equation 4.1 (used to estimate 4DD in the previous section) and equation 4.3 is the latter considers beam-on time and per-beam weightings of each beam dose, rather than per-phase weightings of the combined dose from all beams on each phase. The two 4DD estimates will diverge when beams deliver dose to the ITV non-uniformly and per-beam phase weights vary, inter-phase. As an example, consider superior-inferior tumor motion defined in two phase images, *p1* (tumor in a superior location) and *p2* (tumor in an inferior position) with weights *w1* and *w2*. Assume beam 1 (*b1*) delivers dose only to the superior

region of the ITV, *b2* only two the inferior region, dose to the tumor due to each beam in each

phase is:

$$D_{p1}^{b1} = 1 , D_{p1}^{b2} = 0$$
$$D_{p2}^{b1} = 0 , D_{p2}^{b2} = 1$$

According to equation 4.1, 4DD is independent of beam-on time and dose to each phase is

estimated as

$$D_{p1} = \sum_{b=b1,b2} D_{p1}^{b} = 1$$
$$D_{p2} = \sum_{b=b1,b2} D_{p2}^{b} = 1$$

Then $4DD = \sum_{p=p1,p2} w_p D_p = w_{p1} + w_{p2} = 1 \ \forall w_p$, independent of per-fraction weight variations.

However, according to equation 4.3, $4DD = \sum_{b=b1,b2} \sum_{p=p1,p2} w_p^b D_p^b = w_{p1}^{b1} + w_{p2}^{b2} = [0,1]$, i.e. the dose

can vary from 0 to 1 depending on the sampled phase-weights per beam, per fraction.

For eight patients (4 LA, 4 SBRT), 4DD is estimated according to equation 4.3. Before estimating

4DD, however, an estimate of weight variations per fraction, per beam, is necessary.

4.3.1 Methods to Estimate Variability in Anatomic-Phase Weights

The variation in anatomic weights during each beam of each fraction can be estimated from the

total beam-on-time as the product monitor units per beam (MU_b) and the dose rate (DR), and a

reproducible patient breathing period (T) divided by the number of fractions. For ten phases

per breathing period (N_p=10), the expectation value of the number of anatomies seen by each

beam during each fraction is

$$\langle n_{ana}\rangle = \frac{MU_b \times N_p}{N_{fx} \times DR \times T}.$$
4.4

By randomly sampling the beam-on starting phase for each fraction, the realized weights during each fraction will fall between a minimum (w_p^{min}) and maximum (w_p^{max}) of

$$w_p^{min} = \text{floor}\left(\frac{\langle n_{ana}\rangle}{N_p}\right)\Big/\langle n_{ana}\rangle; \quad w_p^{max} = w_p^{min} + 1\Big/\langle n_{ana}\rangle.$$

Using these min- and max- values to estimate per-fraction variability allows for a simple assessment of anatomic weightings, assuming a reproducible breathing pattern. In reality, breathing patterns are not perfectly reproducible.

By sampling actual patient breathing patterns for durations determined from beam-on times estimated from controllable, machine-specific parameters, a more realistic value of phase weights can be estimated for each patient, for each fraction. An interface to the Pinnacle[3] TPS was constructed as part of this dissertation which utilizes patient-specific breathing patterns, as captured by the RPM infrared camera, to determine patient-specific, per-beam phase-weights for each fraction.

The RPM infrared camera samples breathing amplitudes at 33 Hz with each point labeled with a phase (between 0 to π) determined from peak inhale and exhale positions. The beam-on data defines the equi-weighted, 4DCT phase images. Variations of phase-weights, based on sampling portions of the breathing pattern normalized according to the beam-on data, are used to estimate per-beam, per-phase weight variations and ultimately variations in 4DD. Figure 12 shows the RPM-interface and the weights from sampling the entire beam-on data set (left, the

weights are defined as equal for the beam-on set) and a portion of the breathing data (right)

based on a random starting phase and beam-on time determined from MU_b, number of

fractions, and dose-rate.
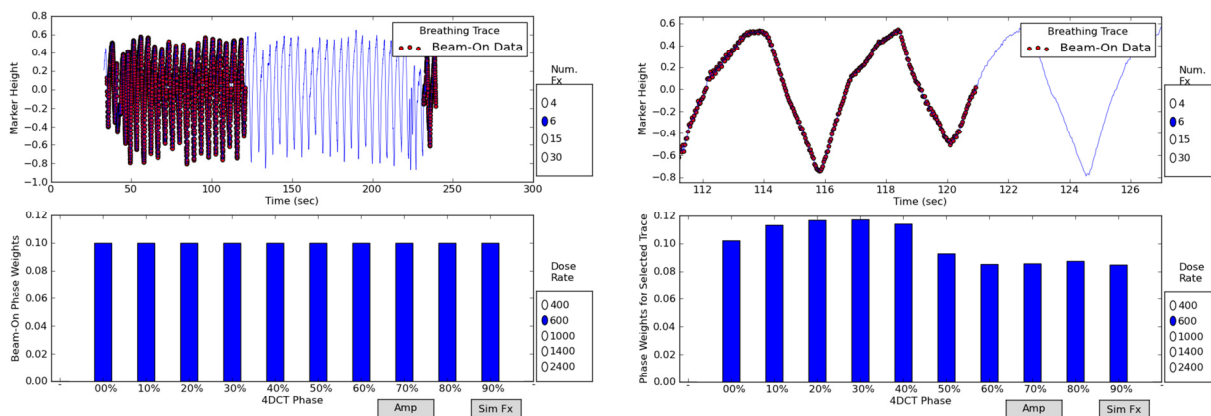
Figure 12. A breathing-data interface to the Pinnacle[3] TPS is shown. The beam-on data is used to establish the equal phase weightings sampled in 4DCT (left). By sampling a portion of the breathing pattern the phase-weights are reassigned (right).

The method of sampling the patient-specific breathing patterns in this dissertation assumes

that the assigned phases are independent of the sampled amplitude, i.e. that the RPM-assigned

phases are labeled correctly with respect to reconstructed phase images. In fact, the

reconstructed 4DCT phase images may be more closely related to the amplitude of the

breathing trace at the time the images are captured. For example, in the right-panel of Figure

12, the minimum amplitude at (time =) 120 seconds is approximately -0.6 cm in amplitude,

whereas the surrounding exhale peaks display -0.8 cm amplitude. This work assumes all of

these minima positions represent the maximum exhale phase-image (50%). An alternative

method assumes the 4DCT phase is a function of amplitude, so that the exhale-peak at -0.6 cm

may, in-fact, identify weightings for a different phase (e.g. 30%).

For the 8 selected patients, 4DD is calculated according to equation 4.3. Per-beam phase-weightings are estimated for LA patients for 30 fractions at 2 dose-rates: 600 and 1000 MU/min and for four fractions and 3 dose-rates for SBRT patients: 1000, 1400, and 2400 MU/min. For the LA patients, the MUs from the 30%-ITV plan are varied to achieve a minimum of CTV-4DD$_{95}\approx$70 Gy. For the SBRT patients, the clinically planning MUs are used to estimate phase-weight variations.

4.3.2   Accumulated Dose Estimation with Varying Phase-Weights

Figure 13 shows the average anatomic weights which may be realized over 30 fractions as a function of beam monitor units, according to equation 4.4. The error-bars show two standard deviations about the mean (which converge to the 4DCT sampled equal weights of 0.1 in all cases); the standard deviations show the range of weights which will be realized during each fraction. When beam-on time per fraction is an integral number of breathing periods the standard deviation goes to zero. For the four LA patients, the median MU_b=3846 MUs, the mean is 5467 MUs, and the range is 1,555 to 16,034 MUs.

In
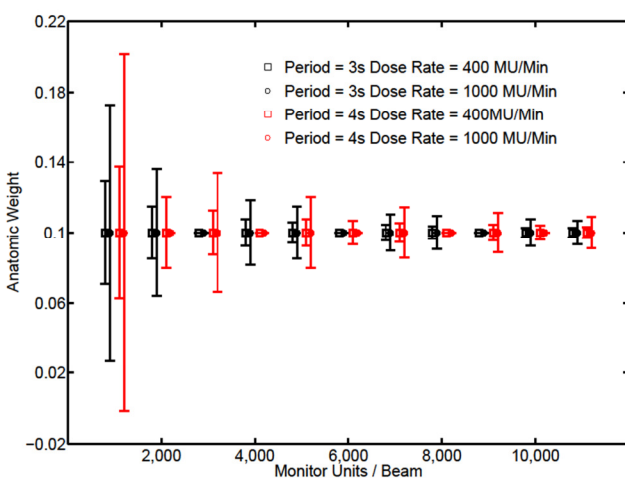
Figure 13. Average inter-fraction phase-weights, and two standard deviations sampled over 30 fractions based on random starting phase. The standard deviation goes to zero when the beam-on time is an integral number of breathing periods for each fraction.

the four hypo-fractionated SBRT plans, delivering treatment in four fractions at 1,000 MU/min is a typical approach, however new technology delivers up to 2,400 MU/min.[112] For the four SBRT patients considered in this study, clinically optimized monitor units per beam per range from 436 up to 1508. Figure 14 shows anatomic weight variations per beam per fraction, based on delivering to ten anatomies (N_p=10) over four fractions (N_{fx}=4) at variable dose rates and breathing periods according to equation 4.4. In the patient cases considered, weight variations from 10%-20% will be observed during each fraction for all patients, even if the patient breathing pattern is perfectly reproduced throughout treatment.

For both LA and SBRT patients, sampling patient-specific breathing patterns shows similar variability revealed in Figures 13 and 14 with common per-fraction weight variations between 0.09 and 0.11 for LA patients and >20% variations about the mean weights (0.08 to 0.12) in hypo-fractionated, SBRT treatment. However, the effect of fractionation results in average phase-weights which approach 0.1 as sampled in 4DCT.

Two methods are used to estimate the variability in dose to the target (4DD$_{95}$), defined as the standard deviation in 4DD$_{95}$ for each of the eight patients. In the first method, termed the 3-sample approach, three samples of 4DD$_{95}$ are averaged and used to compute the standard deviation. The three samples are (1) nominal weightings (w_p = 0.1) on all phases, (2) w_p = 0.11 on the five phases surrounding inhale (i.e phases 80%, 90%, 00%, 10%, and 20%) and 0.09 on the phases surrounding exhale, and (3) w_p = 0.09 on the phases surrounding inhale while the phases surrounding exhale have w_p = 0.11. This method of estimating the effects of interplay

shifts the weights between different portions of the respiratory cycle where dose differences, in all likelihood, are at a maximum.
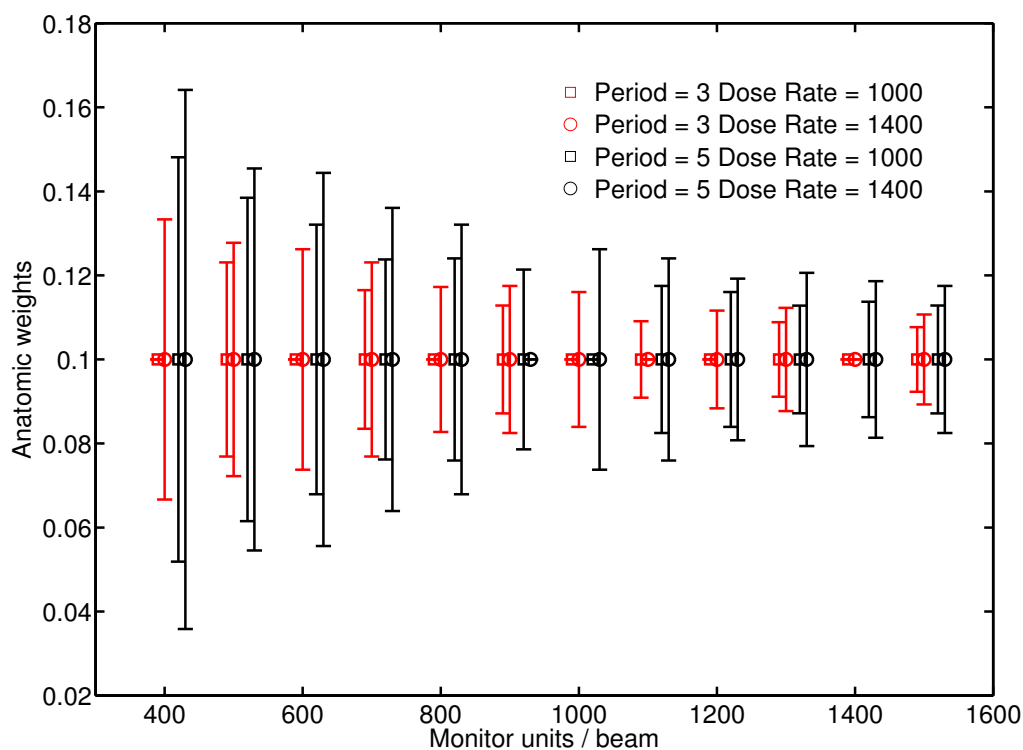
Figure 14. Anatomic phase-weightings and inter-fraction variations based on delivering radiation to 10 different anatomies in four fractions.

In a second method to estimate the standard deviation in $4DD_{95}$, the patient breathing patterns are sampled ten times to estimate inter-fraction phase weights. The ten weight samples are used to compute ten samples of target $4DD_{95}$ and are averaged. The variability in $4DD_{95}$ is reported using the standard deviation of the ten samples for the eight patients.

4.3.3   Results: Effects of Weight Variations on Accumulated Dose

The three sample approach to estimate variability in accumulated dose results in equal or larger variations than sampling patient specific breathing patterns for the four LA patients. The standard deviations about the mean CTV-4DD$_{95}$ (<CTV-4DD$_{95}$>), based on the 3-sample approach for the four patients are 0.01 Gy, 0.01 Gy, 0.2 Gy, and 0.6 Gy. Sampling patient-specific breathing patterns for 30 fractions at a dose rate of 600 MU/min and 1400 MU/min, for ten samples, results in standard deviations which are less than or approximately equal (to within 0.01 Gy) to the 3-sample approach. The mean dose and standard deviation about the mean are reported in Table 3 for the LA and SBRT patients based on sampling patient-specific breathing patterns. In all cases, the standard deviation in 4DD$_{95}$ is less than 0.5% of the equi-weighted estimate based on equation 4.1.

Despite the sampled weight distributions varying by >50% of the nominal values (i.e. from 0.05 to 0.15) in sampling patient breathing patterns dose rates ≥1400 MU/min, the 4DD$_{95}$ varies by less than 0.32 Gy in the LA plans and by less than 0.26 Gy for the SBRT patients. The standard deviation in 4DD$_{95}$ increases by a factor of at least 2 for delivery at 2400 MU/min compared to delivery at 1400 MU/min. However, even at high dose-rate, the variability in 4DD$_{95}$ is negligible.

Table 3. Average and standard deviation (σ) of accumulated dose to 95% of the target (<4DD$_{95}$>) based on ten simulated deliveries. The variations in total dose are negligible in all cases.

	N$_{fx}$	<4DD$_{95}$> $\pm$ σ (Gy)		
Dose Rate (MU/min)		1000	1400	2400
N2	4	48.43±0.01	48.45±0.03	48.40±0.08
N3	4	47.73±0.01	47.73±0.02	47.76±0.11
N4	4	47.58±0.04	47.57±0.04	47.66±0.26
N5	4	46.10±0.02	46.09±0.02	46.01±0.07
Dose Rate (MU/min)		600	1400	
P3	30	70.15±0.01	70.15±0.01	
P5	30	71.65±0.32	71.71±0.32	
P6	30	72.11±0.02	72.08±0.02	
P10	30	68.66±0.01	68.66±0.02	

4.3.4   Summary: Effects of Finite Delivery Time and Patient Breathing on Accumulated Dose

Weight variations due to finite delivery time, non-uniform delivery, and interplay with patient breathing have a negligible effect on target 4DD$_{95}$. Standard deviations in mean CTV-4DD$_{95}$ based on sampling ten deliveries are less than 0.32 Gy in all cases considered even when delivered at dose rates up to 1400 MU/min for LA patients and up to 2400 MU/min for hypo-fractionated, SBRT patients. Simulating as few as three scenarios, considering 10% weight variations between different portions of the breathing cycle, results in larger standard deviations in mean CTV-4DD$_{95}$ than sampling patient-specific breathing for the cases

considered. This implies that a simple evaluation of a few extreme scenarios may bound estimates of 4DD variability due to finite delivery time.

Further studies are needed to estimate 4DD variability due to interplay effects. Several effects were not considered in this preliminary study including the effects of mis-labeled breathing phase, biologic effects of inter-phase dose variation, and per-aperture, MLC interplay. Incorporating these effects into 4DD estimation is a future goal. A per-aperture sampling and 4DD estimation methods are analogous to the per-beam approach, but requires dose distributions computed for each aperture. Once the per beam phase sampling is complete, the per-aperture weightings are a subset of these weightings which depend on the MLC leaf sequence. Consideration of the leaf sequence and appropriate temporal resolutions will allow an estimate of MLC interplay effects. The breathing interface to the treatment planning system creates possibilities for these and other studies.

4.4 CONCLUSIONS: DOSE ESTIMATION IN TIME-DEPENDENT ANATOMY

This chapter focused on improving single planning image dose estimates (3DD) using all 4DCT phase images and estimating accumulated dose (or 4DD). Using a single image to estimate dose, when 4D-data is readily available, may be justified if differences in 3DD and 4DD are insignificant to clinical outcomes. However, this chapter shows target 4DD can be less than, greater than, or equal to 3DD for several different 3D-RTVs (e.g. the stationary target or the PTV) and several different dose-evaluation metrics (e.g. dose at fixed volume, volume at fixed dose, and *gEUD*). In fact, target dose deviated from PTV dose by >3% in 19/30 cases considered for locally advanced patients and in 3/5 SBRT cases considered. This implies that dose

accumulation is a necessary component of RT to time-dependent anatomy and can improve

knowledge of dose delivered to time-dependent anatomy.

5 Multiple Anatomy Optimization of Accumulated Dose

MAO – Multiple Anatomy Optimization

PTP – Probabilistic Treatment Planning

EV – Expectation Value

PDF – Probability Density Function

MIGA – Multiple Instance Geometric Approximation

RC – Robust Counterpart

The first aim of this study is to show that RT for time-dependent anatomy can be improved

through inclusion of all 4DCT phase images for dose-estimation and plan optimization. This

chapter focuses on plan optimization which incorporates all 4DCT phase images, as opposed to

plans optimized on a single planning image. Based on the results of the previous chapter,

under-dosing a moving lung cancer target is possible if the entire PTV is not treated to a

minimum dose. This implies, in order to ensure the moving target is covered; regions of normal

tissue must be treated to a tumoricidal dose. By optimizing the accumulated dose (or 4DD)

based on a known motion pattern, it is possible to incorporate patient-specific motion in plan

design and potentially increase the therapeutic ratio. Radiotherapy plan optimization of the accumulated dose distribution is introduced in Appendix A as multiple anatomy optimization (MAO) and is discussed in this chapter. MAO is a method of probabilistic treatment planning (PTP) which has been researched extensively in RT, but has not been clinically implemented.

5.1 INTRODUCTION

Probabilistic treatment planning (PTP) integrates a probability density function (PDF) of multiple anatomic instances into an optimized dose distribution. Statistical characteristics of the dose distribution evaluated on planning structures can be inferred from a known PDF of the occurrence frequency of variant anatomies, including an estimate of the dose expectation-value (dose-EV). Li and Xing[113] introduced a method to optimize dose-EV using organ specific, Gaussian PDFs. Birkner *et al.*[114] proposed a similar method to account for rigid motion which optimized the dose-EV based on measured random and systematic set-up error. Birkner *et al.*[114] proposed an adaptive routine relying on information gathered throughout treatment, as opposed to use of a single planning image. McShan *et al.*[115] introduced a method termed a multiple instance geometry approximation (MIGA). MIGA calculated dose on multiple anatomic instances and computes an expected dose, this is consistent with the MAO approach described herein.

After the introduction of 4DCT for lung cancer simulation, methods of optimizing the accumulated dose using 4DCT data were described by Trofimov *et al.*[31] In their work, a dose-EV approach is introduced based on two methods of dose estimation, (1) a weighted sum of dose kernels computed on 4DCT images (similar to MIGA) and (2) a convolution approach, where the

motion PDF is convolved with a planning image, 3D-dose.[109,116] The two methods are equivalent if the motion is rigid for all anatomy. Plans generated via the motion kernel method were compared to margin-based plans, gating plans, and idealized tracking plans for one lung and one liver case. The comparison showed that motion-kernel methods can produce plans comparable to idealized gating and tracking in terms of target coverage and OAR sparing.

Zhang et al.[117] compared target tracking and a dose-EV approach (named 4D-inverse planning) using a convolution dose calculation. Their work also demonstrated that 4D-optimization can achieve similar target coverage and OAR sparing to target tracking without necessitating delivery synchronization with breathing for four patients. Söhn et al.[118] compared lung cancer plans optimized based on the ITV method, idealized-tracking, and a weighted sum of dose kernels for one patient and also show potential to spare OARs using PTP. While the potential advantages of incorporating 4D- information (and estimating the dose-EV) in RT optimization have been shown by these studies, there is concern about the validity of these, and other 4D-planning approaches due to variability and uncertainty in the motion PDFs.

For a known PDF, Unkelbach and Oelkfe introduced dose-EV optimization for assumed Gaussian distributions[119] and for estimated data using Bayesian inference.[120] By simultaneously optimizing dose-EV and minimizing dose variance, their method achieved robustness against uncertainty in the PDF. Heath et al.[121] implemented these methods for lung cancer RTP and included uncertainty in patient breathing. They compared optimized solutions to worst-case optimization (see e.g. Fredrikkson et al.[122]) and a margin-based approach. Heath et al.[121] demonstrated that target dose can be compromised in the presence of uncertainty if the dose-

EV is optimized without consideration of the dose variance. A similar result was shown by Sheng et al.[123] in a simulation study.

Chan et al.[124] and Bortfeld et al.[125] optimized dose-EV and included uncertainty in patient breathing using a robust counterpart (RC) approach[126] in which the objective function is redefined in terms of robust parameters. Nohadani et al.[127] investigated stochastic optimization and applied the method to the lung cancer RT optimization problem including uncertainty in the patient breathing pattern. Mulvey et al.[128] was one of the first to consider stochastic optimization for problems with uncertain parameters, a method in which several solutions are generated with different sensitivities to uncertain parameters. For a given parameter variation, solutions below a threshold of sensitivity were called robust. The threshold should depend on the level of risk, and the level of risk in the RT optimization problem depends on the intent of treatment, uncertainty in the TCP and/or NTCP, clinical significance based on calibration tolerances, and several other factors.

The collection of reviewed literature which presents and compares methods of MAO for lung cancer RT optimziation[31,117,118,121,125,129] includes a total of 12 lung cancer patients. Among this patient cohort, 3D-motion ranges from 0.8 cm to 2.9 cm, including 9/12 patients with 3D-motion >1.1 cm and 5/12 with 3D-motion >1.6 cm. In fact, only Heath et al.[121] considered patients with tumor motion <0.9 cm (2 of 5 total patients considered). Despite moderate CTV motion, Heath et al.[121] indicated a potential to spare ipsilateral lung mean dose (from 3.8 Gy to 2.7 Gy and from 5.4 Gy to 5.2 Gy) and reduce ipsilateral lung V20 (from 23% to 20% and 7% to 4%) for these patients. It is intuitive that the MAO approach will benefit patients which exhibit large tumor excursions (e.g. >1cm) because the proportion of healthy tissue within an ITV is

directly proportional tumor excursion.   However a recent study of 250 lung cancer patients shows evidence that approximately 90% of all lung tumors move <1 cm.[130] This suggests the patient population presented in studies of 4D-optimization is not representative of the lung cancer patient population and that the benefits of an MAO approach may not yet known for >90% of all lung cancer patients.

This work implements MAO in in a research version of the Pinnacle[3] commercial TPS. The proposed method uses a single, 10-phase 4DCT image set for planning and computes dose on all phase images, analogous to the MIGA method. The accumulated dose (or 4DD) is optimized for the ten locally advanced (LA) lung cancer patients. MAO plans are compared to ITV plans for these ten LA patients all presenting <1 cm motion (detailed in Table 1).   Target dose robustness based on the MAO dose distribution due to finite delivery time and sampling patient-specific breathing patterns is also examined.

5.2 METHOD OF MULTIPLE ANATOMY OPTIMIZATION (MAO)

The general objective function in eq. 2.1 is combined with individual objectives specified in eq. 2.2 to write the MAO objective function as

$$O\left(\vec{d}^{\,\mathbf{4D}}\right) = \sum_{n \in N_{ROIS}} w_n \sum_{i \in n} c_{i,n} \left(d_i^{4D} - D_n^{RX}\right)^2.$$

5.1

The sums are carried out over i 4DD values (d_i^{4D}) which define dose to the nth structure; each structure has a prescription $D_n^{RX} \; \forall i \in n$. Consistent with the ORBIT implementation, the $c_{i,n}$ include a proportionality constant and a Heaviside function defined such that

$$\Pi(x) = \begin{cases} 0 \text{ if } x \leq 0 \\ 1 \text{ if } x > 0 \end{cases}$$

For maximum and minimum dose objectives, the constant for voxel *i* of relative volume $\varDelta v_i$ within the nth ROI is

$$c_{i,n} = \varDelta v_i \frac{\Pi\left(\mp d_i^{4D} \pm D_n^{Rx}\right)}{\left(D_n^{Rx}\right)^2}.$$

The relative volume of each voxel, $\varDelta v_i$ is less than 1 when part of the ith voxel is outside the ROI, and is equal to 1 in all other cases. The argument of the Heaviside function flips signs of the dose value and dose prescription depending on whether the objective is a minimum or maximum dose objective.

For dose volume objectives, there is a 2nd term in the $c_{i,n}$ coefficient which includes volume of the ROI at or above a specified accumulated dose level. The relative volume at prescription dose is

$$V\left(\vec{d}^{4D}\right) = \frac{\sum_{i \in n} \Pi\left(d_i^{4D} - D_n^{Rx}\right) \varDelta v_i}{\sum_{i \in n} \varDelta v_i}$$

and the coefficient for minimum and maximum DVH objectives is

$$c_{i,n} = \frac{\Pi\left(\mp d_i^{4D} \pm D_n^{Rx}\right)\Pi\left(\mp V(d_i^{4D}) \pm V_n^{Rx}\right)}{\left(D_n^{Rx}\right)^2}$$

where V_n^{Rx} is the volume prescription level. If the ROI volume at prescription dose is acceptable, no voxels are penalized. If the volume at prescription dose is not met, only voxels with dose

below dose-prescription are penalized for targets, voxels with dose above dose prescription are penalized for OARs.

Consistent with the BFGS method (Radiotherapy Plan Optimization, page 19), the gradient of the objective function with the respect to the vector of beamlet weights, $\vec{b}$, is calculated and used to estimate the inverse Hessian. The gradient of the objective function defined in eq. 5.1, for a collection of p phase images and a vector of accumulated dose $\vec{d}^{4D}$ (=4DD) is

$$\frac{\partial O(\vec{d}^{acc})}{\partial \vec{b}} = \frac{\partial}{\partial \vec{b}}\left(\sum_{n \in N_{ROIS}} w_n \sum_{i \in n} c_{i,n}\left(d_i^{4D}(\vec{b}) - D_n^{Rx}\right)^2\right) = \sum_{n \in N_{ROIS}} 2w_n \sum_{i \in n} c_{i,n}\left(d_i^{4D} - D_n^{Rx}\right)\frac{\partial \vec{d}^{4D}}{\partial \vec{b}}$$

Focusing on the last term on the right hand side, $\vec{d}^{4D}$ is computed as a weighted sum of per-beam phase doses D_p^b each weighted by w_p^b:

$$\vec{d}^{4D} = 4DD_{ref}(\vec{r}) = \sum_b \sum_p w_p^b D_p^b\left(\vec{r} + v_{ref \leftarrow p}(\vec{r})\right)$$ with $\vec{r}$ parameterized at each of i spatial positions.

The jth beamlet deposits dose to the ith voxel of phase p according to the according to the dose deposition coefficients K_p^{ij}, however the i voxels are rearranged according to the DVF, $v_{ref \rightarrow p}(r_i)$ at the indexed positions r_i. The 4DD at voxel i in the reference image due to beamlet j is

$$d_i^{4D} = \sum_b \sum_p w_p^b K_p^{i'j} b_j$$ with i' determined from $r_i' = r_i + v_{ref \rightarrow p}(r_i)$. The rearranged dose deposition coefficients to phase p, $K_p^{i'j}$ can be written as a matrix $\tilde{K}_p$, then the 4DD vector is written

$$\vec{d}^{4D} = \sum_p \tilde{K}_p \left(\vec{w}_p \circ \vec{b} \right)$$ with $\circ$ the element by element, Hadamard multiplication between a vector of

phase weights $\vec{w}_p$ with elements w_p^j, each representing the probability of encountering the pth

phase anatomy for the jth beamlet. Then

$$\frac{\partial}{\partial \vec{b}} \left(\sum_p \tilde{K}_p \left(\vec{w}_p \circ \vec{b} \right) \right) = \sum_p \hat{K}_p \left(Id \right)_{jxj} \vec{w}_p = \sum_p \hat{K}_p \hat{w}_p \approx \sum_p w_p \tilde{K}_p = \left\langle \tilde{K} \right\rangle \qquad 5.1$$

Where the weight matrix, $\hat{w}_p$, has the anatomic weights for each beamlet along its diagonal.

The right hand side assumes the anatomic weights are constant for all beamlets (i.e.

independent of beam-on time) and is reduced for clarity, so that the weighted sum of deformed

dose deposition coefficients is approximated by $\left\langle \tilde{K} \right\rangle$. The deformation and interpolation (to

perform accumulation) of the dose-deposition kernels, rather than the dose itself, was first

discussed in Trofimov *et al.*[31] The gradient with respect to the jth beamlet is

$$g_j^b = \sum_{n \in N_{ROIS}} 2 w_n \sum_{i \in n} c_{i,n} \left(d_i^{4D} - D_n^{Rx} \right) \left\langle \tilde{K} \right\rangle_{ij} = \sum_{n \in N_{ROIS}} 2 w_n \sum_{i \in n} c_{i,n} \Delta_i \left\langle \tilde{K} \right\rangle_{ij}$$

Where the superscript b is used to indicate beamlet space, and Δ_i is the difference between the

i^{th} voxel dose and the prescription dose. The $\left\langle \tilde{K} \right\rangle$ transforms the gradient of the objective

function from dose-space to beamlet space. The gradient is estimated in dose space with each

element defined according to

$$g_i^d = \sum_{n \in ROIs} 2 w_n \sum_{i \in n} c_{i,n} \left(d_i^{4D} - D_n^{Rx} \right) \qquad 5.2$$

where $\vec{g}^d$ denotes the gradient defined in dose space. In the BFGS-implementation, the Hessian

is initialized with an identity matrix and updated at each iteration. Following the work of Löf *et*

al.[80], the Hessian is initialized to the identity matrix and a line search algorithm[131] is used

determine the step size λ, the optimization algorithm is:

1. Compute the gradient according to 4.2, define an update

$$\vec{u}^d = -\hat{H}\vec{g}^d$$

   With a corresponding beamlet update of $\vec{u}^b = -\left(\hat{H}\vec{g}^d\right)^T K$

2. Line search for the step size λ, based on $\vec{d}' = \vec{d} - \lambda\vec{u}$

   a. If $d(i) < 0$ set $d(i) = 0$

   b. Compute the new gradient, $\vec{g}'$ according to 4.2, based on $\vec{d}'$

   c. Test Wolfe conditions (see, e.g. Nocedal and Wright[79], Chapter 3) for constants $c_1, c_2,\ 1 > c_2 \geq c_1 > 0$.

   $O\left(\vec{d}'\right) \leq O(d) + c_1\lambda\left(\vec{g}^d\right)^T \vec{u}^d$, the Armijo condition.

   $\left(\vec{g}^{d'}\right)^T \vec{u}^{d'} \geq c_2\left(\vec{g}^d\right)^T \vec{u}^d$, the curvature condition.

      i. If met, accept, go to (3)

      ii. If not met, try new λ (up to 20 times)

3. Accept solution and end optimization, or continue to 4.

4. Define $\delta = \vec{d}' - \vec{d},\ \gamma = \vec{g}' - \vec{g}$ and update $\hat{H}$

$$\hat{H} = \hat{H} + \frac{\delta\delta^T}{\delta^T\gamma}\left(1 + \frac{\gamma^T\hat{H}\gamma}{\delta^T\gamma}\right) - \frac{\delta\gamma^T\hat{H} + \hat{H}\gamma\delta^T}{\delta^T\gamma}$$

    5.   return to (1)

The MAO algorithm computes the accumulated dose at each step size (step 2), according to equation 4.1, so that the 4DD and the 4DD-gradient must meet the Wolfe conditions. The initial approximation of the Hessian in MAO is determined by continuing a single image, ITV-based optimization. The current implementation of MAO does not directly access the dose deposition coefficients and therefore does not use the deformed dose-deposition coefficients described in equation 5.1 which results in an inaccurate beamlet update, $\vec{u}^b$, (in step 1). This often results in several line searches per iteration, and often exhausts 20 attempts (as in 2.c.ii above) in which case the search direction is changed. By integrating the deformed dose-deposition coefficients in the numeric optimizer of the Pinnacle[3] TPS, the efficiency of the method will be improved.

Implementation of MAO, as described herein and in Appendix A, has reference-phase dependence. In computation of the gradient and the objective function, the reference phase determines which voxels are included (i.e. which violate prescription) and which voxels are assigned to each structure. For example, the Heaviside function is zero-valued in the reference phase but the corresponding position in other phases has $c_{i,n} \neq 0$. In order to ensure all target voxels are included in the gradient and objective function calculation, the obejctives on structures which overlap the PTV are defined as non-zero for all dose distributions. If an

objective reaches zero-value, the volume level at prescription, V_n^{Rx}, is reduced in 5% increments until a non-zero objective value is found. In heart, for example, the dose-volume prescription at 30 Gy is reduced to 0% if necessary. This ensures all voxels of the PTV are included in each optimization step, even if these voxels enter the objective function as OARs.

5.3 MULTIPLE ANATOMY OPTIMIZATION (MAO) IMPLEMENTATION

The three-phase phantom shown in Figure 15 is used to demonstrate possible advantages in MAO-planning compared to the ITV method. A region of the image which includes a target (a 2 cm water sphere) moves rigidly and is defined in left, middle, and right phases. There is a phase-dependent relationship between the target (green) and the OAR (red) in the phantom.
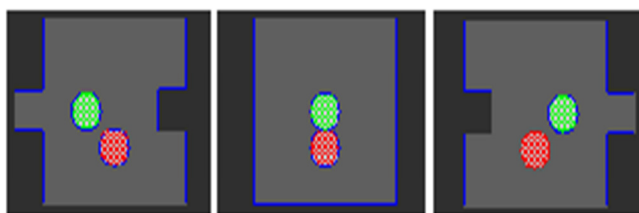
Figure 15. A 3-phase phantom which includes a moving target (green) and a fixed OAR (red).

All plans are optimized to deliver 70 Gy to the target. The OAR is also a water equivalent sphere and is stationary in all phases; plans include a max-dose objective of 45 Gy on the OAR (similar to a spinal cord objective). The surrounding 10^3 cm^3 cube has CT#=300, similar to lung, and the optimized plan includes a non-zero dose-volume objective at 20 Gy (V20<0.15).

The ITV-plan is designed to deliver 70 Gy to the union of phase-defined targets, while the MAO solution is designed to treat the moving target to 70 Gy. Figure 16 shows the ITV solution (top left) and the MAO solution (bottom left) assuming equal phase weightings. The MAO solution uses phase-specific dosimetry so that the accumulated dose (bottom right) achieves the OAR objective (OAR D_{max}<45 Gy) and avoids treating the target in the reference phase.
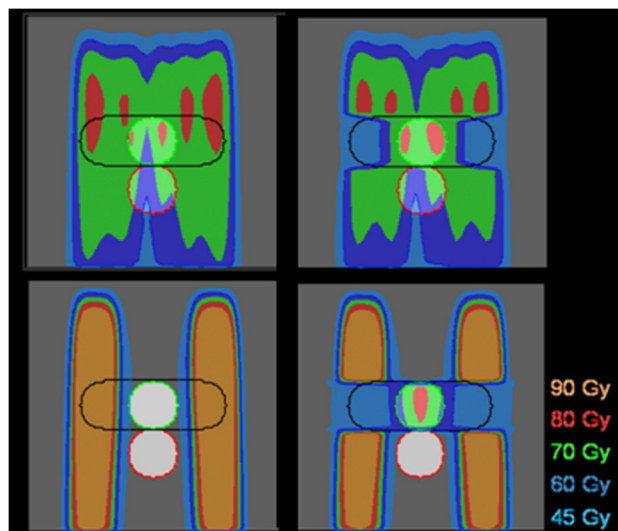
Figure 16. Optimized dose distributions using the ITV method (top left) and MAO (bottom left). MAO avoids treating the OAR in all phases, but the accumulated dose (right images) meets prescription.

The MAO solution reduces the volume at prescription dose but also increases maximum dose in the surrounding cube. This is an example of a potential advantage of MAO compared to ITV planning. If there is a time-dependent relationship between an OAR and a moving target, MAO will incorporate this information in plan design and preferentially treat regions which avoid the OAR.

Another possible advantage of MAO is the ability to incorporate the target PDF in the optimized solution. The ITV method assumes the target is uniformly distributed within the ITV, i.e. all regions of the ITV are equally weighted. If the CTV is non-uniformly distributed in the ITV, MAO can preferentially treat the target in spatial locations of high probability and avoid treating

regions of low CTV-probability. In order to show this effect, the phantom phase weights are shifted from equal weightings, i.e. w_p = (0.33, 0.33, 0.33), to unequal weights w_p = (0.2, 0.1, 0.7). The ITV solution is unchanged, whereas the MAO solution preferentially treats the target in the region where it spends the most time. Shown in Figure 17, the accumulated dose (right) meets prescription and reduces V20 on the surrounding cube from 26% to 22%. The MAO dose distribution follows the PDF distribution, preferentially treating in the right phase with higher CTV-probability.
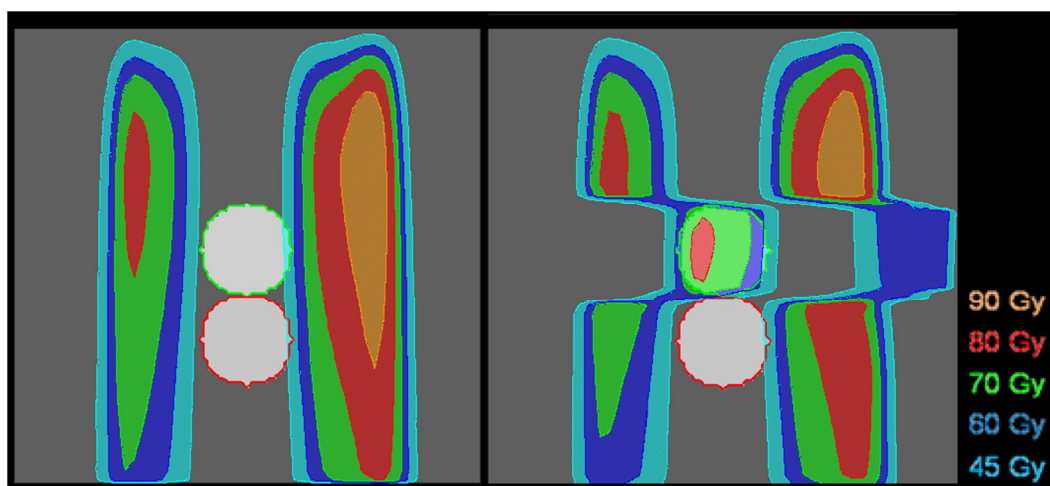
Figure 17. An example of an MAO dose distribution (left) and accumulated on the reference phase (right). The target spends 70% of the time in the right phase and 20% of its time in the left phase, and MAO shifts the dose towards the right phase.

5.3.1 Results: Comparison of MAO and ITV Plans

In Appendix A, MAO plans are generated and compared to ITV plans for the ten LA patients. ITV plans are designed on the inhale phase (00%-ITV plan), the mid-ventilation phase (30%-ITV plan), and the aCT (aCT-ITV plan) as described in chapter 4. Plans are compared at optimized-MU values and, by adjusting MUs in the 30%-ITV plan, at fixed CTV-4DD$_{95}$. Increasing MUs in an

ITV-plan can ensure accumulated dose meets prescription and clarifies potential advantages of MAO plans in terms of OAR sparing.

At optimized monitor units, MAO increases 4DD-V70 by an average of 3.5% (±4.3%, p=0.01) compared to ITV plans. Increased D_{95} with MAO planning is not significant in the patient population, on average 0.35 Gy ± 1.27 Gy (p=0.8), but is increased by at least 1 Gy in 8 of 30 comparisons (10 patients, 3 ITV plans each). At fixed CTV-4DD$_{95}$, the MAO plan is superior to the 30%-ITV plan in 5/10 cases in terms of OAR sparing by at least 3% volume at fixed dose.

For P3, with 3D motion just 0.39 cm, there were clear advantages in MAO planning. At optimized monitor units, MAO meets the CTV-4DD$_{95}$ prescription, whereas the 30%-ITV plan treats CTV-4DD$_{95}$=71.5 Gy. By reducing target D95 to 70 Gy, ipsilateral mean lung dose is reduced by 2.2 Gy, a reduction in V20 of 7%, even though 3D motion for this case is just 0.39 cm. At fixed CTV-4DD$_{95}$ for P3, ipsilateral lung V20 is reduced from 48% to 41%, esophagus V25 from 12% to 7%, heart from 28% to 25%. DVH curves for the MAO- and ITV- plans are shown in Figure 18.
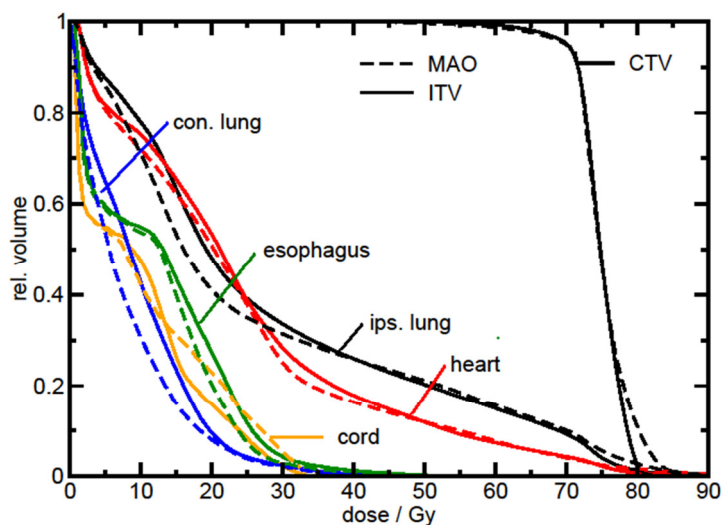
Figure 18. Dose volume histogram (DVH) for P3 based on the 30%-ITV plan and an MAO plan. At fixed dose to 95% target volume (CTV-D$_{95}$), MAO spares all OARs at objective dose levels.

In two other cases, ipsilateral lung volume at 20 Gy (V20) is reduced by >4% volume. For the other two patients which show >3% OAR volume sparing in MAO compared to ITV, esophagus V25 is reduced by >3%. Using the

Pearson correlation coefficient, the potential for OAR sparing using MAO compared to the ITV method is not correlated to 3D-motion ($r^2 = 0.08$, $p = 0.8$). The lateral motion showed a weak correlation ($r^2 = 0.42$, $p = 0.2$), the largest CTV motion is measured in the lateral direction for P3 (0.28 cm) and P7 (0.41 cm) and MAO reduces a combined total of all OAR volumes at prescription levels by 16.3% and 5.9% for these cases.

There is less than 3% improvement in combined OAR volume sparing in 5/10 cases considered. However, MAO is always superior to the ITV method in terms of OAR sparing at fixed CTV-4DD$_{95}$, even if this sparing is small (e.g. <3% volume). For P1 and P2, this may attributed to 3D-CTV motion which is on the order of the voxel size (~0.3 cm). P7 is a unique case, different from others because the patient presents an extended lesion with central and peripheral components extending from the inferior airway to the diaphragm; MAO showed little benefit in treating these lesions. Patients P8 and P9 present 3D-motion of 0.7 cm and 0.8 cm, respectively, and while MAO reduces ipsilateral lung V20 by 2% in each case compared to the 30%-ITV plan, MAO does not reduce dose in other OARs. For each of these patients, both presenting central lesions, there is little benefit to an MAO approach.

Figure 19 shows MAO plans optimized on the inhale, 00%-phase (top left) and an MAO plan optimized on the 30%-phase (bottom left) for P10. The reference phase dependence of the MAO solution is clear in this case in both the optimized solution (left) and the accumulated dose (right).

In MAO as implemented in this dissertation, dose-voxels enter the objective function as components of either the CTV, of an OAR, or of both. The optimizer aims to reduce dose in voxels which are included as OARs, and increase dose in voxels included as target. This leads to

hotspots in the reference-phase CTV and cold-spots outside of the reference phase CTV. This reference-phase dependence biases solutions and may not lead to globally optimal solutions. Methods to generate a solution independent of reference phase structures are focus of future studies. Considering dose updates on each phase and combining these updates is one approach to generate a solution independent of reference-phase structure definitions.
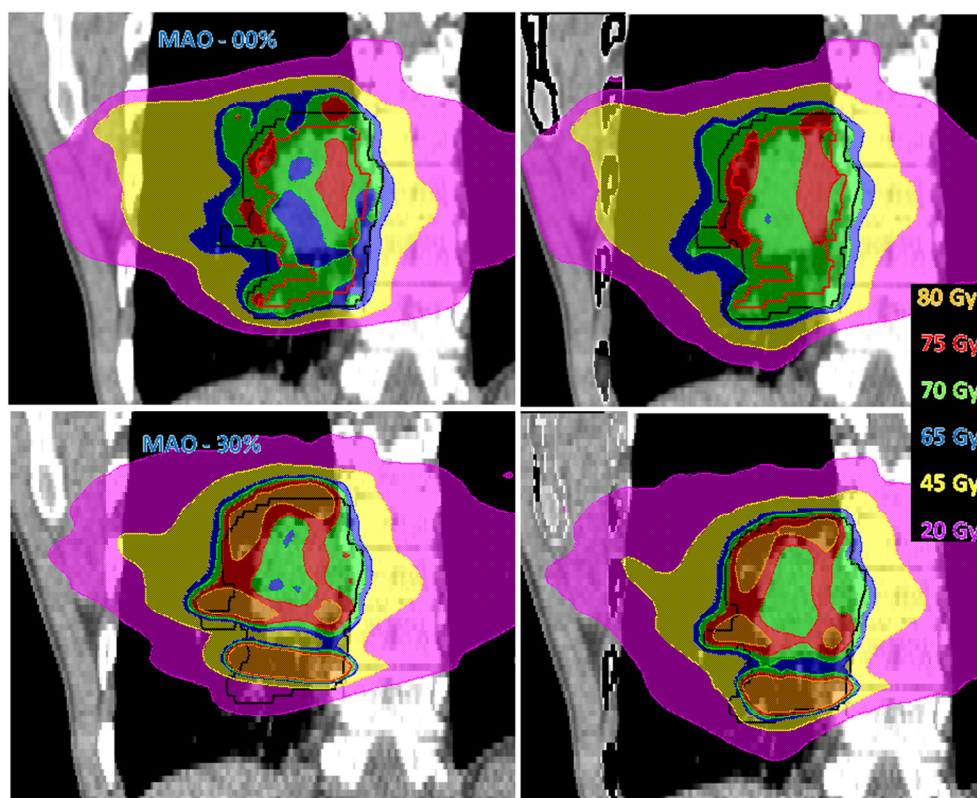
Figure 19. The MAO solutions are shown on the left as optimized with a 00%-phase assigned as the reference (top) and a 30%-phase reference (bottom). The solutions are clearly different, as are the accumulated dose distributions (right).

5.3.2 Results: Effects of Interplay on MAO Dose Distributions

The sensitivity of target dose with respect to finite delivery time and patient-specific breathing is estimated using the same methods described in Chapter 4. Two analyses are carried out, the first method uses the 3-sample approach of CTV-4DD$_{95}$ values (equal weights for all phases, and 10% weight variations distributed over inhale and exhale); in the second analysis, 10 simulated deliveries are carried out based on sampling patient-specific breathing patterns for 30 fractions. Two dose rates are considered, 600 MU/min and 2400 MU/min, which span a range of clinically relevant dose-rates (600 MU/min) and a high dose rate (2400 MU/min) which could potentially be used clinically. For four MAO-optimized plans which show potential to spare OARS compared to ITV plans, the standard deviation in CTV-4DD$_{95}$ based on the two analyses are reported.

The variance in CTV-4DD$_{95}$ using the 3-sample approach is 1.4 Gy for P3, more than double the ITV-plan CTV-4DD$_{95}$ standard deviation of 0.6 Gy using the same approach, the 3-sample method. This is the only case, however, with standard deviation about the mean >0.2 Gy. Similar to the ITV plans, simulating 10 deliveries by sampling the patient specific breathing patterns reduced the standard deviations in accumulated dose compared to the 3-sample approach. This implies the MAO dose distributions, in many cases, are not susceptible to target dose deviations due to PDF variations.

5.4 SUMMARY

For half of the patients considered, MAO shows the ability to spare individual OARs by at least 3% volume compared to ITV plans, whereas for five other patients, little to no benefit was evident. Identifying a population of patients which will benefit from MAO planning is an important element of clinical implementation. Clinical protocols require categorization of patients based on identifiable features, e.g. many clinics use respiratory gating when lung tumor motion is >1 cm. Methods need to be developed which can identify patients which will benefit from MAO and Appendix A shows this is not a trivial identification, 3D-motion did not correlate with MAO's potential to spare OARs in the cases considered. For patients exhibiting large motion (>1 cm), other studies have shown MAO offers benefits in terms of OAR sparing. Based on the results of this work, it is clear MAO may benefit patients which display moderate CTV motion as well.

Phantom studies show MAO can incorporate the target PDF and time-dependent relationships between target and risk structures in plan design. Identifying the target PDF – and its departure from a uniform distribution – may be an indicator of potential improvements. Variations in relative overlap of targets (including uncertainty) and OARs as a function of phase may also correlate to potential improvements using MAO, compared to the ITV method.

Concerns about PDF reproducibility over the course of treatment may not be warranted for all MAO plans. Simulated delivery of MAO plans indicated that variations in CTV-4DD$_{95}$ exceeding 1 Gy are possible due to finite delivery time and patient-specific breathing. However, in ¾ cases, the standard deviation of CTV-4DD$_{95}$ based on 10 simulated deliveries is less than 0.10 Gy

delivered at 600 MU/min and less than 0.13 Gy delivered at 2400 MU/min. Fractionated sampling of patient-specific breathing patterns resulted in a smaller standard deviation in CTV-4DD$_{95}$ than using a simplified, 3-sample approach. For the one case that did show a large variation in CTV-4DD$_{95}$, robust optimization may be a viable solution. Several methods of robust optimization have been implemented for lung cancer RTP[121,124,125,129,132] and is an active area of interest.

The previous chapter showed dose estimation which includes all phases of 4DCT can deviate from single image estimates. This chapter shows optimized dose distributions which include 4DCT data are superior to optimized dose-distributions which use a single planning-image. MAO plans can ensure target coverage is achieved without necessitating a homogeneous dose distribution to the entire ITV. Moreover, MAO plans have the potential to spare OARs and increase the therapeutic ratio, consistent with the overall goal of this dissertation.

6 Dose to Mass in Lung Cancer Radiation Therapy

DMH – Dose Mass Histogram

V_{ROI} – volume of a region of interest

M_{ROI} – mass of region of interest

$D95_V$ – dose to 95% structure volume

$D95_M$– dose to 95% structure mass

The second aim of this dissertation is to utilize structure mass in lung cancer RT treatment planning, as opposed to using structure volume. In this chapter, structure mass is used to estimate delineation consistency, dose-evaluation, and is used in RT plan optimization.

According to the linear quadratic (LQ) model, assuming cell density is proportional to physical density, dose-to-mass is a more appropriate measure of radiation response in tissue. Moreover, there is ambiguity in defining volume and dose-to-structure volume during respiration due to several factors including physical volume variations and delineation inconsistencies. Physically, mass is conserved during respiration and motivates the dose-mass-histogram (DMH) for IMRT evaluation. Analogous to the DVH, the DMH transforms 3D-anatomy and dose into a simple 2D-graph; the cumulative DMH plots relative structure mass as a function of dose level. In section 6.1, differences in DVH and DMH are presented based on planned, 3D-dose distributions and based on accumulated, 4DD for SBRT patients.

Consistent and efficient structure definition in time-dependent anatomy is a hurdle which must be overcome in order to implement 4D-RTP methods such as MAO. Delineating relevant structures on (e.g. ten) phase images in a 4DCT image set is too time-consuming for clinical implementation. Deformable image registration (DIR) offers an automated method to handle structure definition on multiple phase images but DIR validation remains a challenge. In section 6.2, structure mass as a function of respiratory phase is examined. Inconsistencies in structure mass will arise due to delineation inconsistencies and/or images which do not represent physical anatomy.

Finally, section 6.3 considers optimization of dose-to-structure mass. Each voxel of each structure is assigned an importance weighting designated by the voxel density. The method preferentially treats massive regions of the PTV while avoiding massive regions of normal tissue, showing the potential to increase the therapeutic ratio for lung cancer patients. The introduced model of functional optimization can also be used to design RT plans based on an arbitrary importance weighting distribution.

These sections utilize mass, as opposed to volume, in order to present more consistent dose-evaluation metrics, more consistent structure delineation, and a potentially better method of optimizing dose distributions in heterogeneous anatomy.

6.1   DOSE-TO-MASS AND THE DOSE MASS HISTOGRAM

In 2005, Nioutsikou *et al.*[63] described the opacity in defining lung volume and dose to lung volume during respiration. Through phantom experiments, they indicated dose to volume is not a relevant quantity for evaluation of lung dose. Nioutsikou *et al.*[63] contended that they

agree with Butler *et al.*[133], that dose-to-mass and the DMH are more appropriate quantities in evaluation of lung cancer RT than dose-to-volume and the DVH. Butler *et al.*[133] used dose-to-mass evaluation in a study on gated lung cancer RT because the entire lung was not consistently imaged in the included datasets. Mavroidis *et al.*[134] described the magnitude of uncertainty in estimating the DVH of lung based on Gaussian dose distributions due to volume variations. The authors assess the difference between DVH and DMH using two phantoms, one homogeneous and one heterogeneous, and show up to 40% differences between DMH and DVH in the heterogeneous phantom. In a second analysis, a patient case was examined using a pair of opposed-tangential fields; the resulting differences in DMH and DVH were approximately 5% across the entire dose range.

During respiration the volume of lung varies and serves as an example of a limitation of the DVH. Dose-to-mass is a more precise evaluation metric if structure mass, as represented by 4DCT, is constant during the breathing cycle. However, differences between DVH and DMH are not solely due to volume variations. The distribution of density differences between the irradiated set of voxels and the average density of all voxels which compose a structure will create DVH and DMH deviations, even in constant volumes. An ROI volume is the sum of each of the voxel volumes which compose the structure, or $V_{ROI} = \sum\limits_{i \in ROI} v_i$ and the mass of an ROI is defined as the sum the individual voxel masses, $M_{ROI} = \sum\limits_{i \in ROI} \rho_i v_i$.

For anatomy with homogeneous density, any irradiated subset of structure voxels will contain equal proportions of mass and volume and results in equal DVH and DMH at all dose levels. Partially irradiated heterogeneous structures will show DVH and DMH differences that are

patient and radiation-path specific which do not depend on volume differences. No

generalization can be made about DVH and DMH differences, as the irradiated volume may be

more dense than the structure-mean (and DMH>DVH) or less dense than the structure-mean

(with DMH<DVH).

Assuming an ROI is composed of voxels of fixed volume, v, the cumulative DVH is

$$\text{DVH}(D) = \sum_{i \in ROI} \left(\frac{\text{v}}{\text{V}_{\text{ROI}}} \right) \Pi(D - D_i) = \frac{N_D}{N_{ROI}}$$

where the RHS is simply the ratio of the number of voxels at dose D (N_D) and the total number

of voxels in the ROI (N_{ROI}). The DMH value at dose D, for the same ROI, can be expressed

$$\text{DMH}(D) = \sum_{i \in ROI} \left(\frac{m_i}{\text{M}_{\text{ROI}}} \right) \Pi(D - D_i) = \frac{\sum_{(i|d_i > D)} \rho_i}{\sum_{i \in ROI} \rho_i}. \qquad 6.1$$

The cumulative DMH is the ratio of the sum of voxel densities at dose D and the sum of all voxel

densities in the ROI. The differences in DVH and DMH reveal physical characteristics (i.e. the

density) of the irradiated region of a structure.

Dose at volume (e.g. D95), volume at dose (e.g. V20), mean dose, and the generalized mean

(e.g. *gEUD*) are common quantities used to evaluate RT plans. These metrics assume all voxels

within an ROI have equal importance. If a structure has heterogeneous density and the number

of cells in each voxel is directly proportional to density, then according to the LQ model of

radiation damage, all voxels should not have equal importance in evaluation of RT. Figure 20 is

a graphical way to show the difference between volume- and mass- based evaluation. The

volume-based quantities treat all voxels within an ROI equally (top), whereas mass-based

quantities define voxel importance according to density (bottom).

In section 6.1.1, summarizing results of Appendix D, DVH and DMH values are compared for 8

of the locally advanced patients. Dose calculation is performed within the Pinnacle[3] TPS and

mass sampling is performed with dose and image voxels

of 0.3x0.3x0.3 cm^3 (the images are re-sampled at the

dose distribution). Two DVH plans are designed for

comparison, one on the inhale phase image (inhale-

plan) to simulate idealized breath-hold treatment and

one on the aCT image (to simulate free-breathing

treatment). The inhale-plan density results in well-

defined (visible) image contrast; the aCT blurs the

structure densities according to 10 phases of the

respiratory cycle and obscures structure boundaries in

many cases.

Figure 20. The DVH is analogous to the top image, with each voxel weighted by either a 1 or 0. The DMH uses density to weight voxel importance.

The DVH-optimized plans used for evaluation include

objectives for 70 Gy to 95% of the PTV-volume (D95>70 Gy) and PTV maximum dose less than

80 Gy (D_{max}<80 Gy) while minimizing lung V20, esophagus V25, heart V30, and spinal cord

D_{max}<40 Gy. In the inhale plan, the PTV is defined as the inhale-phase GTV surrounded by a

1 cm margin. In the aCT plan, the PTV is a 1 cm expansion about the ITV – the union of the GTV

in ten, 4DCT-phase images. DVH and DMH are compared at all dose levels in the following

section for eight locally advanced patients based on DVH-optimized dose distributions. If the differences are insignificant, dose-to-mass evaluation does not offer new information, as compared to dose-to-volume evaluation.

6.1.1 Results: DVH-DMH Differences

Observed differences in relative volume and relative mass depend on the ROI. For the spinal cord and heart, differences in DVH and DMH (DVH-DMH) are <3% at all dose levels for all patients (8) and DVH-plans (16) considered. For the esophagus, 1 of 8 patients show relative mass/volume differences exceeding 3% at doses above 2 Gy. In each lung, differences in relative mass and volume are patient and plan dependent, exceeding 3% in 3 of 8 inhale-based plans and in 6 of 8 aCT- plans at dose levels ranging from 10-20 Gy. The targets, including GTV and PTV on inhale-plans and ITV and PTV on aCT-plans, also show differences exceeding 3% for all patients near the prescription dose. The PTV dose at 95% volume ($D95_V$), when compared to PTV dose at 95% mass ($D95_M$), differ by up to 15.7 Gy (for P3), implying dose cold spots occur in massive regions of the PTV for this patient. For 5 of 8 patients considered, PTV differences in $D95_V$ and $D95_M$ are less than 1 Gy in both inhale and aCT plans. For the other three patients, these differences exceed 2 Gy in at least one of the two plans. For the GTV (in inhale plans) and ITV (in aCT plans), the results are similar to PTV, with differences occurring near the prescription dose. An example of a DVH and DMH plot is shown in Figure 21.
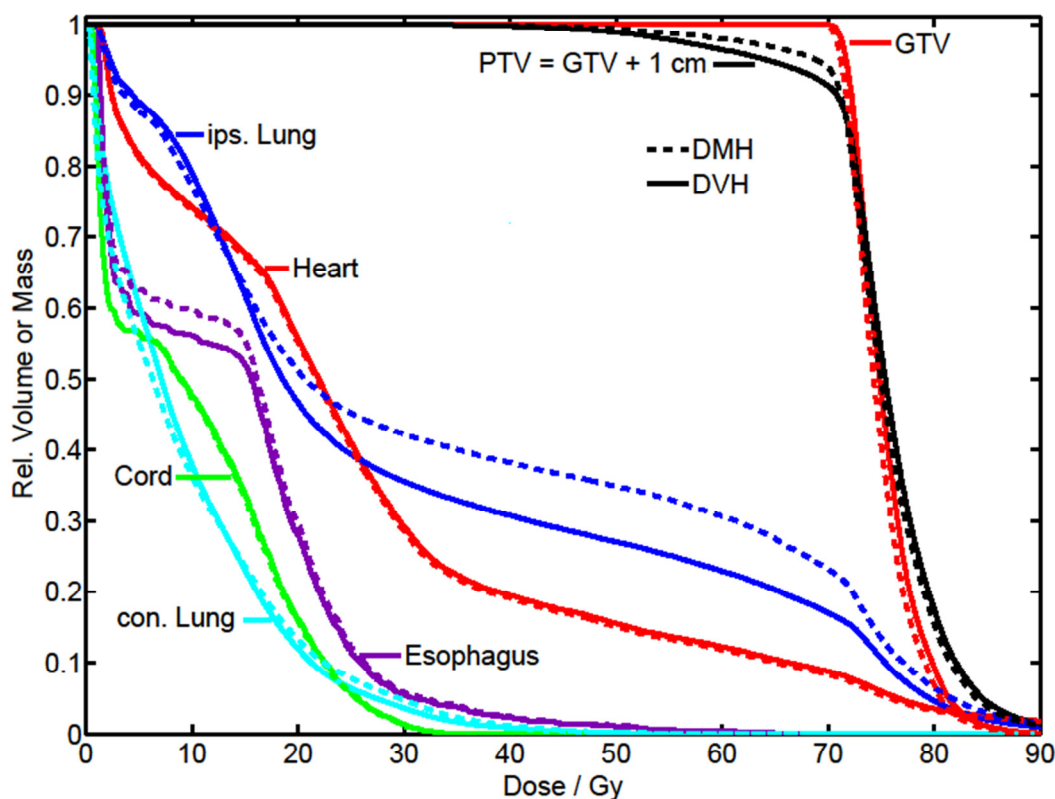
Figure 21. Dose-volume histogram (DVH, solid) and dose-mass histogram (DMH, dashed) for a plan designed on the inhale 4DCT phase (using single image, 3D-dose). Differences in the PTV and ipsilateral lung imply that a relatively dense region of each structure is receiving a large proportion of dose (i.e. DVH<DMH).

6.1.2 Summary: DVH and DMH differences

DVH and DMH differences in the each lung often exceed 3% at fixed dose and exceed 2 Gy at fixed volume or mass solely due to tissue heterogeneities. The study of Mavroidis et al.[134] show similar results for a breast cancer patient. Appendix D shows DVH and DMH in both lung and lung-cancer targets can vary by >10%, and the sign of this difference is patient and radiation-path dependent. However, dose-to-mass evaluation is approximately equivalent to dose-to-volume evaluation (to within 3%) for esophagus, heart, and spinal cord, likely because these

structures are approximately homogeneous. In lung and PTV, however, it is possible that the use of DVH indices result in uncertainty in estimating radiation damage due to corresponding uncertainty in the in initial cell population, based on the LQ-model of cell-kill. The population of cells in these structures may not be trivially related to volume.

6.2 MASS-CONSISTENCY IN 4DCT STRUCTURES

Mass is approximately conserved during respiration, assuming the mass of air exchanged and blood-flow variation as a function of 4DCT-breathing phase is negligible. Structures defined on different phases of a 4DCT dataset should also conserve mass if the images and delineated structures are an accurate representation of physical anatomy. In appendix D, mass and mass-conservation in delineated structures as defined in different breathing phases of 4DCT are reported. Defining structures in all phases of 4DCT is a time-consuming task in RT, but can be done relatively quickly using DIR and contour propagation between different phases of a 4DCT image-set.

In this section, multi-phase structure mass estimation is used to estimate intra-observer delineation consistency for two "observers" - an expert physician and the Demons DIR algorithm available in the research version of the Pinnacle[3] TPS.[99,100] However, delineation consistency is one of several factors which will contribute to mass variation in 4DCT. Motion artifacts due to intra-phase residual motion[7] can artificially change mass; sorting errors (i.e. projections sorted into the wrong respiratory phase)[10] generate mixed-phase images which will reproduce some regions and remove others. Li *et al.*[135] contend that mass deviations due to blood and air exchange create uncertainties in structures defined by DIR algorithms which

specifically penalize mass deviations, including the Demons algorithm (see, e.g.[136,137]). Yin *et al.*[138] introduced a DIR algorithm designed to conserve mass between individual voxels, claiming mass deviations are small enough to be ignored. The Demons registration algorithm, as proposed by Thirion[101], includes an optical-flow step which minimizes intensity differences between points in different images, implying that an ideal Demons-based registration will conserve integral intensity (or in the case of CT images, mass). However, the Demons algorithm used in this work includes regularization terms which allow for some differences in point-to-point intensity conservation without penalty, so the algorithm is not strictly mass-conserving.

The basic assumption of Appendix D, and the following summary, is that mass deviations due to phase-dependent variations in air and blood are negligible. These mass variations can be estimated. The minimum of eight lung masses considered in appendix D is 426 grams (g). The maximum inter-phase volume variation is 480 cm^3 and assuming this volume is composed of air, a mass deviation of approximately 5 g is plausible in a worse-case scenario (i.e. small lung with large volume changes). A recent study of pulmonary blood flow and pulmonary blood volume[139] shows the difference in stroke volume between the sum of pulmonary arteries and the sum of pulmonary veins was 8 ± 8 ml for a cohort of 10 healthy patients. This small blood variation implies blood mass is approximately independent of systole/diastole stages of the cardiac cycle. Estimated instantaneous volume of blood in pulmonary veins and pulmonary arteries showed maximum differences of approximately 50 ml; however, the temporal resolution of 4DCT phase-images is approximately 0.5 seconds - about ½ a heartbeat. The instantaneous differences will not be observed in 4DCT phase images due to the finite temporal resolution of each phase image, and are irrelevant to structure-mass variation reported in this

dissertation. The stroke volume difference (8 ± 8 ml) introduces a potential mass variation of 8 g on average, assuming the 4DCT phases exactly coincide with systole and diastole. Thus, the total mass-variation due to air and blood variations could result in approximately 3% mass discrepancy, i.e. (5g + 8g)/426g, in actual lung anatomy. Based on this information, this dissertation assumes observed inter-phase mass deviations >3% are due to intra-observer delineation inconsistences between structures on different phases of 4DCT.

For 8 locally advanced lung cancer patients, mass of GTV and ipsilateral lung are reported in each of 10, 4DCT phase images. Observed, inter-phase mass differences are assumed to be due to delineation inconsistencies and are cast into a 1-dimensional (1D) spatial difference to describe contouring, or delineation error. Using the volume of the physician-defined 00% phase structure ($V_{00\%}$) and defining a sphere of equivalent volume, the radius of the sphere is

$$r_0 = \left(\frac{3}{4\pi} V_{00\%} \right)^{1/3}.$$ Assuming volumes contoured in other phases (V_{ph}) are sampled from similar density arrays of mean density $\overline{\rho}$, the difference in total mass (ΔM) between $V_{00\%}$ and V_{ph} are used to estimate a corresponding volume discrepancy, $\Delta V = \Delta M / \overline{\rho}$. The phase volume is assumed to have deformed to a spheroid, so that the spatial discrepancy occurs over a fraction f of the original surface ($V_{ph} = f V_{ph} + (1-f) V_{00\%}$) and $\Delta V = f(V_{00\%}-V_{ph})$; the local spatial discrepancies grows with decreasing f. For example, a 10% volume change due to deformation over 1/4 of the original volume (f=1/4) results in a 1D-spatial difference, called Δr, of 16% (or 0.5 cm for r_0 = 3 cm). Δr based on an observed mass difference (ΔM) is

$$\Delta r = r_0 - \left(\frac{3}{4\pi} \frac{(1-f)V_{00\%} - \Delta M / \bar{\rho}}{(1-f)} \right)^{1/3}$$

Mass and volume of ipsilateral lung and GTV are summarized based on physician delineated contours (5 lungs, 8 GTVs) and deformed contours (8 lungs, 8 GTVs), based on the results of Appendix D. A corresponding spatial discrepancy is estimated for the structures with the fractional volume of deformation arbitrarily chosen as f=1/4 in all evaluations.

In section 6.2.3, mass and volume are compared over the course of radiation therapy for one locally advanced patient. Tumor regression is an often-observed consequence of radiation therapy[23,140,141] and increase in lung density (due to, e.g. fibrosis) is a known side-effect of RT in lung.[142] Analyzing the mass of a regressing GTV and changing lung may shed light on the inter-scan consistency of contours and/or mass dynamics between a regressing GTV and lung.

6.2.1   Results: Lung Mass in 4DCT Contours

Physician-defined contours of ipsilateral lung indicate a coefficient of variation for lung volume for each patient ranging between 3.0% and 7.5% of the mean volume, however maximum inter-phase mass variations are greater than 5.2% for all five patients considered based on these volumes (range 5.2%-12.4% of the inhale phase mass). For the same 5 patients, deformed contours of lung result in maximum inter-phase mass differences range from 2.2% - 7.0% of the inhale-phase mass. Figure 22 shows boxes representing the relative mass about the mean at 25th and 75th percentiles, together with the median relative mass, and data which lie beyond

the 99th percentile assuming normally distributed data. P3 and P6 show the largest differences

for physician contours, with maximum ΔM = 36.7 g resulting in Δr = 0.47 cm for P6.
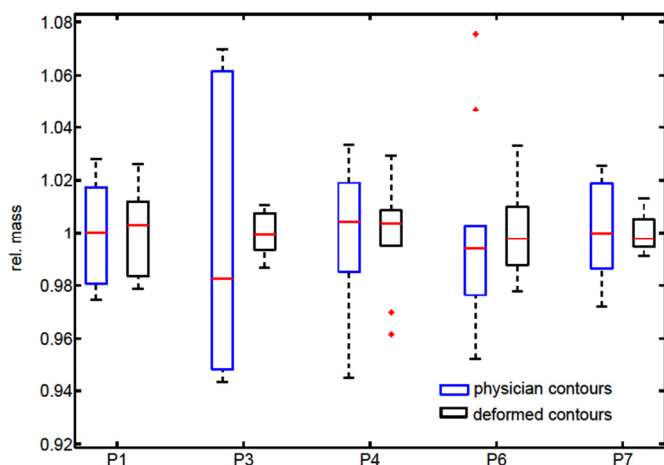
Figure 22. Boxes show the 25th and 75th percentile relative mass about the mean. The whiskers show the extent of data about the median within the 99th% confidence interval, assuming a normal distribution. Outliers (beyond the 99th%) are shown as red crosses.

Deformed contours result in maximum ΔM = 28.8 g with a corresponding Δr = 0.36 cm for P6.

The P6-4DCT dataset has recognizable 4DCT sorting artifacts (including a 'floating diaphragm')

visually evident in many of the phase images. Compromised lung function and alectasis are

evident in the images for P3; deformed contours indicate small volume changes (less than 18

cm^3 of air intake, a 1.5% volume change) and mass conservation to within 11.2 g (2.4% of the

mass at inhale). The physician contours, in this challenging case, indicate >6% volume variation

and mass changing by >10% (>50 g) between different phases in the lung. Using the calculated

average density of 0.38 g/cm^3, the 1D spatial discrepancy is Δr = 0.38 cm when ΔM = 55 g.

For patients P1, P5, and P8, average relative mass and volume of lung is shown in Figure 23.

This figure shows inter-patient variability in lung volume as a function of respiratory phase is

often >10%. Using DIR to define structures has the potential to conserve mass to within 3% in

these cases.
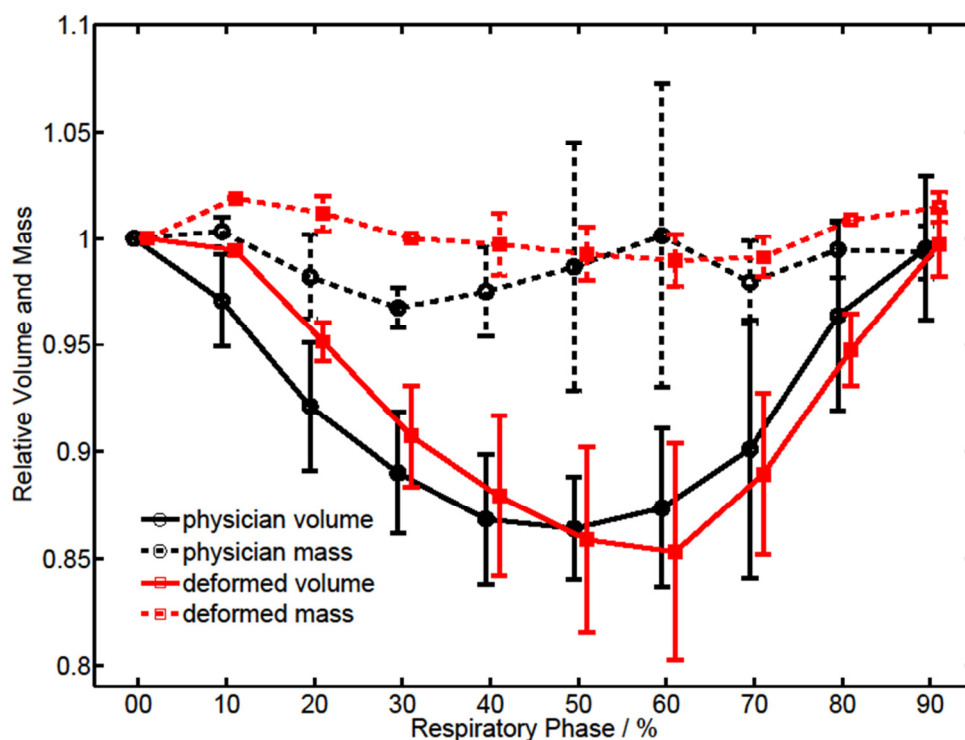
Figure 23. Relative lung mass and volume as a function of respiratory phase, normalized to the 00% (inhale) phase. Error bars show the standard deviation about the average relative mass and volume for three patients, P1, P5, and P8.

6.2.2 Results: GTV Mass in 4DCT Contours

Gross tumor volume and mass for physician-contoured and deformed structures are shown in

Figure 24 as a function of respiratory phase for the eight patients. In 4/8 cases, physician

defined mass varies by >4.5 g across respiratory phases and by >13 g in 2/8 cases. Deformed

contours vary by >4.6 g in 5/8 cases and >12g in 1/8 cases. Mass of the GTVs is approximately

constant, especially for tumors with smaller volume. However, larger GTVs resulted in larger

mass deviations in both sets of contours for the patients considered. The coefficient of

variation of physician contours varies from 1.6%-4.6% of the mean; similarly for 7/8 sets of deformed contours the coefficient of variation varies from 1.0%-3.5%. However, for P9 the coefficient of variation of GTV mass is 8.6%. This is the largest deviation in deformed contours, and can be considered a failure of the DIR algorithm (ΔM = 12.4 g, Δr = 0.33 cm). Inspection of the inhale-phase image, where the GTV contours are initially defined, reveals sorting artifacts near the superior and inferior border of the tumor. This implies that DIR is not reliable if image artifacts are present, which is not surprising. However, this also implies that evaluation of deformed structure mass may enable detection of 4DCT artifacts.

The physician contoured GTV mass and volume for P10 shows phase dependence similar to the lung, the GTV mass and volume are at maximum near inhale and minimum near exhale (maximum ΔM = 15.6 g, Δr = 0.16 cm). In general, in the GTVs considered, a large volume variation resulted in a large mass variation. The Spearman correlation coefficient between maximum volume and mass differences between the phase images is 0.93 for the physician contoured GTVs, and 0.98 for the deformed GTVs. Similar correlation is revealed when considering the standard deviation in GTV mass as a function of phase. Specifically, the correlation between the standard deviation in volume and the standard deviation in mass is >0.93 in all cases considered. This implies that GTV motion is approximately rigid in the cases considered.
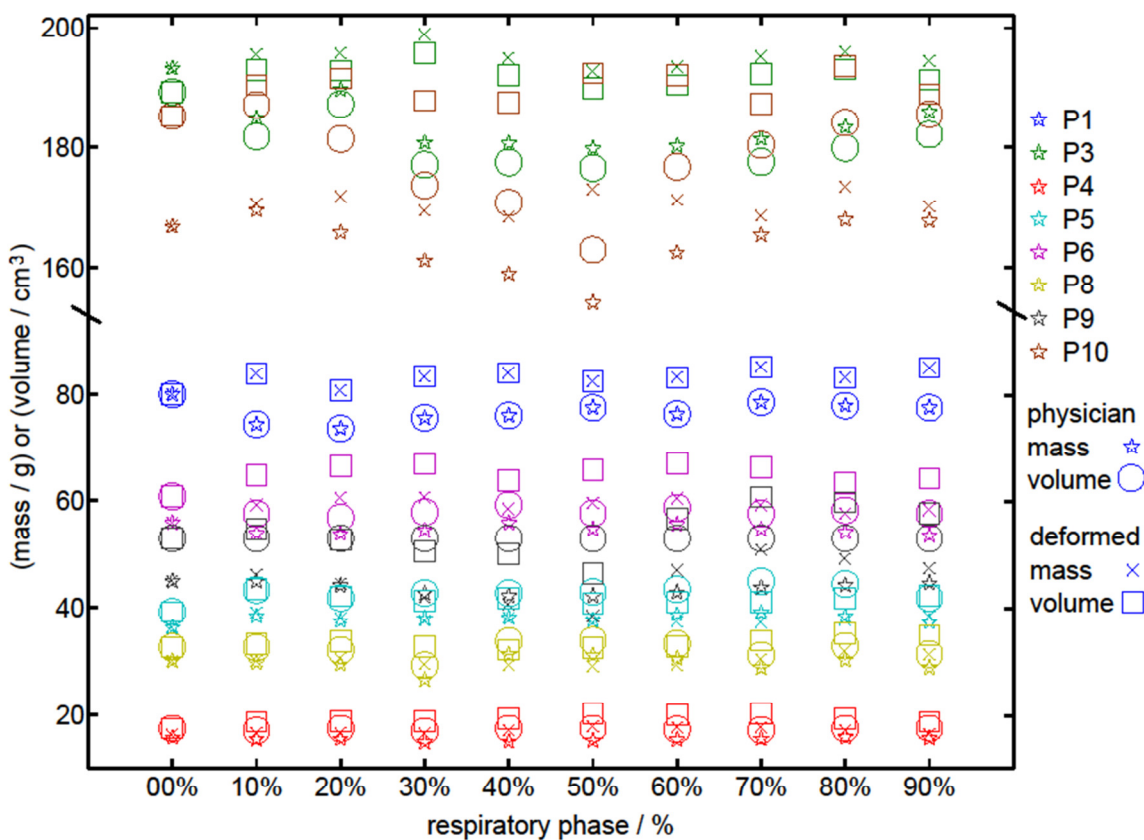
Figure 24. Gross tumor volumes (GTV) masses and volume as a function of respiratory phase for eight locally advanced lung cancer patients for physician defined contours and deformable registered contours based on the demons algorithm.

6.2.3 Mass Variation during Radiotherapy

For one patient who received serial 4DCT simulation scans, structure volume and mass is reported at different stages of RT in this section. Two 4DCT image sets for P10 were acquired approximately 6 weeks apart amid fractionated RT. The physician defined lung and tumor contours on the inhale phase indicate a 65.8 g reduction in tumor mass at 6 weeks, a 35% reduction of initial mass. The volume is similarly reduced by 66.8 cm^3. The ipsilateral lung, according to the physician drawn-contours shows an increase in mass and volume of 120.9 g and 652 cm^3, respectively. Inspection of physician contours in each scan, e.g. in Figure 25,

shows regions of the physician defined, regressed GTV contour exclude regions of anatomy which were included in the initial, planning contours. This delineation inconsistency dominates analysis related to lung and GTV mass dynamics for this case. Deformation of the planning contours to the 6-week scan results in a GTV with volume and mass 113.8 cm^3 and 84.0 g, 27 g less than the physician contour. Based on this case, more consistent structure definition is required in order to use mass of lung and GTV to estimate regression and lung fibrosis due to radiation damage.
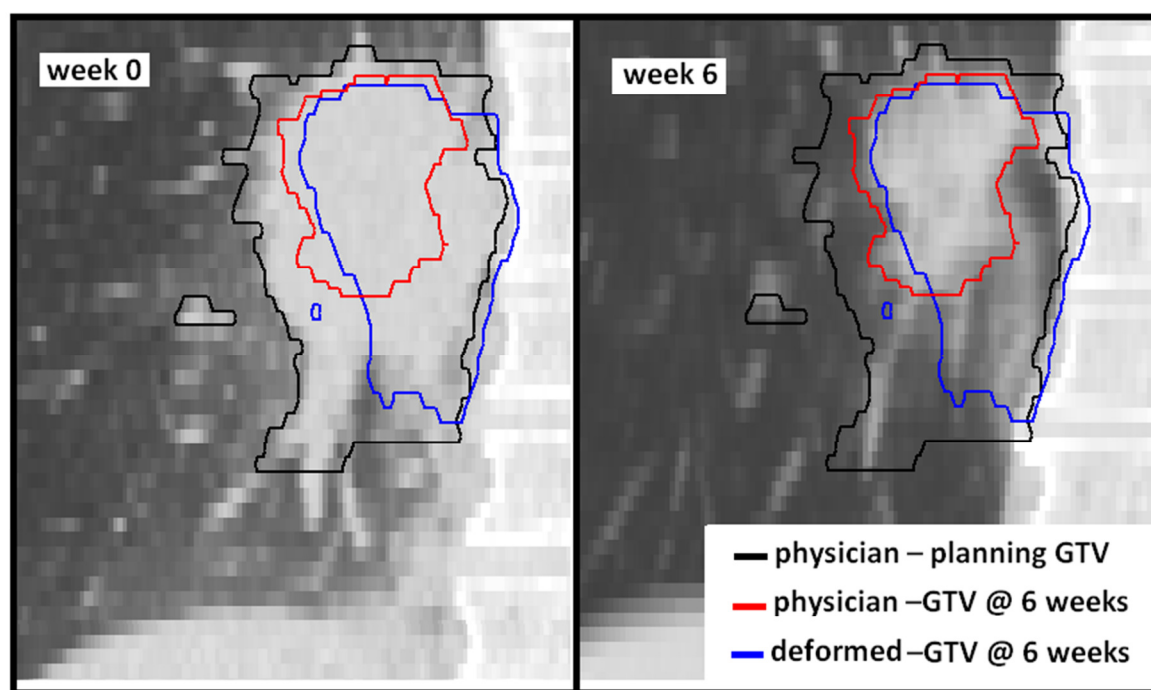
Figure 25. Coronal images of P10 at simulation and 6 weeks after simulation (during fractionated treatment). The gross tumor volume (GTV) varies significantly inter-scan and inter-observer.

6.2.4 Summary: Mass-Consistency in 4DCT Structures

The current standard for simulation of lung cancer patients is 4DCT; under the assumption that 4D information will improve the quality of plans and the associated risk/benefit analysis. A

prerequisite to improving the quality of plans, however, is accurate and consistent structure definition in 4D-images. Reduction of inter- and intra- observer contouring variability remains a significant challenge (see, e.g. Louie *et al.*[66]). There is no ground-truth value of a delineated internal structure, so that inter- and intra- observer delineation studies can only measure precision of contours.

In addition to inherent variability in delineated structures, the process of manually delineating structures on slices of CT images is also time-consuming. For a ten-phase 4DCT dataset, contouring ten-sets of structures is not clinically plausible. This is an unacceptable burden on expert physicians, and limits the utility of 4DCT data. Deformable image registration (DIR), on the other hand, can create contours on multiple 4D-images through contour propagation relatively quickly. However, DIR-based structure definition suffers from the same limitations as physician contours; there is no way to measure the accuracy of these contours. Using the fact that structure mass defined in different phases should be constant, delineation consistency can be estimated.

Monitoring structure mass in different phases of 4DCT has the potential to lead to more consistent structure definition. In this work, consistent GTV mass (to within 7 g) is observed using Demons-DIR contours for 7/8 patients. In 1 image set, however, DIR failed to preserve mass across respiratory phases. Further inspection of this image, and in particular the image used to define the initial contour, revealed image-artifacts. For this case, mass-based evaluation of structures identified registration problems that required attention. Structure mass is more consistent across respiratory phases in DIR-based contours than physician-delineated structures for lung and GTV.

Mass variation due to RT is an active area of interest. Using mass analysis, it may be possible to estimate mass-dynamics between the GTV and surrounding lung and relate these dynamics to RT outcomes. However, consistent structure delineation is a necessary condition in order to perform such an evaluation.

6.3 OPTIMIZING DOSE TO MASS

Integral dose is defined as the integral of dose (D) to mass, $I = \int_{mass} D\, dm$.[143] Integration of dose over volume reveals a fundamental difference in evaluation of dose-to-volume and dose-to-mass. Integration of dose over a volume composed of n elements, each with dose $D_n = E_n/m_n$ is

$$\int D\, dV = \sum_n D_n \frac{m_n}{\rho_n} = \sum_n \frac{E_n}{\rho_n} \, ,$$

or the sum of energy absorbed per unit density in each voxel. The Integral dose of n-elements is the energy absorbed within the mass,

$$\int D\, dm = \sum_n \frac{E_n}{m_n} m_n = \sum_n E_n = E^{abs} \, .$$

Consider, for example, a heterogeneous structure composed of 2 voxels with densities of ρ_1=1.0 g/cm^3 and ρ_2= ρ_1/10 =0.1 g/cm^3 and equal volumes, v = 1 cm^3. A beam is designed to deliver uniform dose of 50.0 Gy to each voxel (estimated using a dose calculation algorithm which corrects for heterogeneities). All of these quantities are reasonable estimates in, e.g. two (large) voxels of an SBRT lung cancer patient PTV – one which is GTV, one which is a mixture of GTV, lung tissues, and air. The energy absorbed in voxel 1 is E_1=0.05 J (Joules),

energy absorbed in voxel 2 is E_2=0.005 J. The integral dose is the total energy absorbed, 0.055 J. The dose integrated over volume of the structure is 0.10 J / (g/cm^3). In this case, the dose integrated over volume is not representative of a physical quantity. However, if the voxels had equal densities, integral dose to volume is directly proportional to integral dose to mass.

Limitations of external beam radiation therapy through rotational photon delivery have been described based on the concept of integral dose conservation within spherical shells of homogeneous tissues.[144,145] Specifically, all beam arrangements and fluence patterns which deliver equal dose to an isocenter point will also deliver equal integral dose to concentric spherical shells about the isocenter point. However, integral dose is not conserved between different beam/delivery conditions in heterogeneous structures, i.e. the limitations only apply to homogeneous structures. Specifically, delivering a larger proportion of fluence through lower density normal tissue will reduce the integral dose in such a spherical shell. This implies that inclusion of voxel mass in plan optimization has the potential to reduce radiation path lengths (and radiation dose) in normal tissues. Consistent with the overall goal of this thesis, optimizing dose to mass has the potential to increase the therapeutic ratio for lung cancer RT.

Optimizing dose-to mass through evaluating dose-mass histogram (DMH) levels is a simple method of voxel importance weighting for RT optimization which only relies on information acquired in 4DCT simulation. However, density may not be well-correlated to functionality in organs in such as lung. Several studies have investigated the relationship between density and lung functionality, but this area must be further explored in order to minimize dose to functional lung using only 4DCT.[146–149] Castillo *et al.*[146] have considered methods to produce ventilation images from 4DCT data sets but their results indicate that neither the Jacobian

determinant of the DVF nor the fractional air content of each voxel correlates well with perfusion imaging, with dice similarity coefficients less than 0.4 in six of seven cases.

In parallel organs such as lung, the number of surviving functional sub units (FSUs), as a proportion of the total number of FSUs, determines the complication probability.[150] Assuming FSU density is directly proportional to physical density; the biologic effect of treating less mass is directly proportional to complication or control probability, implying that the DMH is an appropriate choice for RT evaluation. However, as previously mentioned, the FSU and physical density are not trivially related in lung. Another surrogate will be required for functional optimization of lung tissue and an analogous evaluation metric can be constructed and optimized. Analogous to the CT-reconstruction of physical densities, the quantity which labels voxel importance will replace ρ in the definition of DMH (equation 6.1) if a functional image is available. Previous studies have incorporated lung perfusion imaging in lung-cancer RT plan optimization[151–156] in order to reduce dose to functional lung. Perfusion imaging can replace, or be combined with, mass weighting to optimize dose to functional tissue.

Section 6.3.1 summarizes results from appendix D, where plan-optimization based on DMH levels is carried out and compared to DVH-based optimization. A total of four plans per patient are compared, two DVH-optimized plans described in section 6.1 (an inhale-plan and an aCT-plan) and two DMH-optimized plans. In the inhale plan, the PTV is defined as the GTV surrounded by a 1 cm margin. In the aCT plan, the PTV is a 1 cm expansion about the internal target volume (ITV) – the union of the GTV in all phase images defined in the aCT image. All of these plans use single images for dose-estimation (i.e. 3D-dose) and plan optimization (single

planning image), combining mass-based optimization with 4D-dose optimization is a focus of future studies.

The DVH plan objectives include 70 Gy to 95% of PTV while minimizing lung V20, esophagus V25, heart V30, and spinal cord maximum dose limited to 40 Gy. The DMH-objective levels are translated trivially from these DVH values. Objectives are defined at relative mass levels; 70 Gy to 95% of the PTV mass (M70) and minimization of M20 for lung, M25 for esophagus, M30 for heart. Plans are compared at objective dose levels.

6.3.1   Results: Optimized Dose-to-Mass

A total of sixteen DMH-optimized lung cancer plans are created, two plans for 8 locally advanced patients. The target-prescription in each of the plans is to treat 95% of the PTV volume or mass to 70 Gy and this objective consistently trades-off with the ipsilateral lung, V20 objective. This tradeoff, combined with large differences between DVH and DMH levels for these structures, is the primary force producing differences between DVH- and DMH- optimized plans. In 13/16 DVH-optimized plans, cold-spot distributions in dense PTV sub-volumes result in V70 > M70. DMH-plans, for these cases, increase PTV-mass coverage towards prescription with a corresponding increase lung-mass at dose.

Optimization of DMH levels for P1 increases PTV-D95$_M$ from 49.7 Gy to 58.4 Gy compared to the DVH-plan. This 8.7 Gy increase in mass-coverage is achieved by increasing PTV-D95$_V$ by just 3.2 Gy (from 65.4 Gy in the DVH-plan to 68.6 Gy in the DMH-plan). A comparison of DVH- and DMH- optimized inhale-plans is shown in Figure 26 for P1.

Figure 26. DVH- and DMH-optimized dose distributions for P1. Ipsilateral lung DMH < DVH and optimized DMH levels resulting in target (the PTV) dose increased to meet prescription.
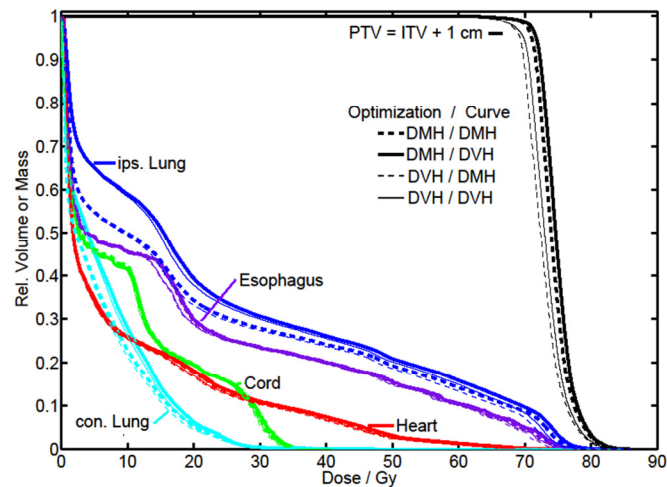
A different trend was observed for P3, PTV-D95$_V$ is reduced by 12.6 Gy in the DMH-based inhale plan and by 8.5 Gy in the DMH-based aCT plan, resulting in reduced lung mass and volume at dose (by 9-14% of DVH-optimized values). However, PTV-D95$_M$ is reduced by just 2.5 Gy in the inhale plan (69.4 Gy to 66.9 Gy) and by 1.8 Gy (68.8 Gy to 67 Gy) in the aCT-plan. In other words, the DMH plan for P3 reduces dose to low-density regions of the PTV in order to spare lung, while maintaining an approximately constant dose to the massive regions of the PTV. Consistent with 13/16 DVH-plans, PTV-V70 > PTV-M70 and the DMH-plan boosts PTV-M70 to prescription for P3. By increasing dose to massive regions of the PTV, the DMH plan for P3 reduces lung-mass at 20 Gy by >5%.

Figure 27 shows DVH and DMH curves resulting from optimizing dose-to-volume and dose-to-mass. In this case, the DMH-optimized plan boosts a dense region of the PTV up to prescription in order to spare lung. However, the PTV volume is not covered which is a concern when considering geometric uncertainty. The purpose of treating the PTV is to ensure all plausible

spatial location of the actual target are treated to a prescription does but the DMH-optimized dose distribution does not cover the PTV.

For P4, the DVH- and DMH- optimized plans are nearly identical. Comparing the two plans, lung V20 and M20 vary by 0.5% volume in the inhale plans, and by less than 1% in the aCT plans and PTV dose (both $D95_V$ and $D95_M$) varies by <1.3 Gy in all plans. The inhale DMH-plans are also approximately identical to DVH-plans for P5, while the aCT plan shows potential to reduce ipsilateral lung (ilung) V20 and M20 by >3% volume while maintaining constant target dose. The DMH plan also spares ilung in the aCT (4.6% volume decrease in V20, 5.1% mass decrease in lung M20) and boosts PTV-$D95_M$ compared to the DVH plan, but the inhale plan shows very small differences. Both the inhale- and aCT- DMH plans show potential to spare lung volume and mass at 20 Gy by >2.9% relative volume or mass at comparable target dose.

While lung volume and mass levels varied between plans optimized using either DVH or DMH, this was not the case for heart, esophagus, and spinal cord dose. For all eight patients and all 16 plans compared, esophagus V25 and M25 and heart V30 and M30 differ by <0.6% volume or mass between DVH and DMH plans. Spinal cord volume at 40 Gy varies by up to 0.6% volume between DMH and DVH plans for P10, but for the other 7 patients, this volume is equal among DVH and DMH plans.
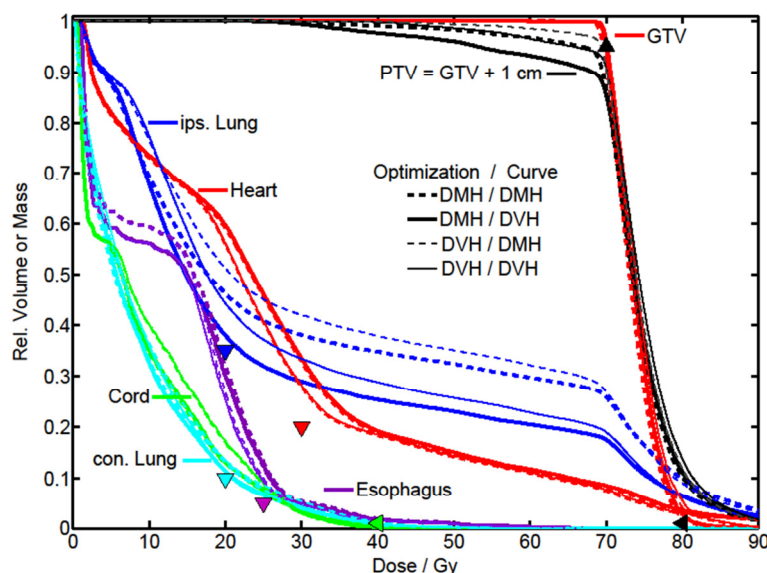
Figure 27. An optimized DMH-plan which maintains dose to the PTV-mass while reducing dose to the PTV-volume compared to a DVH-plan. The DMH-optimized plan spares lung volume and lung mass by >5% at 20 Gy.

6.3.2 Summary: Optimizing Dose-to-Mass

Mass as a surrogate for voxel importance in DMH-based optimization for RT of lung cancer shows potential to spare lung and increase the therapeutic ratio. The DMH weights voxels according to their density, implying the DMH-optimized solution will preferentially treat relatively dense target regions and avoid relatively dense regions of normal tissue. Using mas as a surrogate for cell-importance makes sense, intuitively, in the lung cancer target. The LQ-model of radiation damage relies on the initial number of cells. In lung, however, low density parenchyma may be important in oxygen exchange. Optimizing DMH uses density for voxel importance, but this quantity can be replaced by some other indicator of functionality (e.g. perfusion) if one is available.

Further investigation of DMH-based optimization must incorporate spatial uncertainty. In one case considered, DMH-optimization achieved the dose-to-target mass objective, PTV-

M70>95%. However, in order to simultaneously reduce dose to lung, the resulting plan reduced PTV-D95$_V$ by 12.6 Gy. This solution invalidates the PTV, i.e. the solution is no longer robust against setup uncertainty. Combining functional information and geometric uncertainty is a focus of future studies, including methods to over-write voxel importance based on spatial locations. By considering the probability distribution of target mass, an appropriate dose-to-mass optimization may be possible using MAO.

6.4 Conclusions

Evaluation of structure mass has utility in delineation, in dose evaluation, and in plan optimization. By incorporating mass in RT for lung cancer and for time-dependent anatomy in general, potential improvements in the therapeutic ratio may be possible. Relying on the premise that mass is constant during respiration, evaluation of structure mass defined on different respiratory-phases is an estimate of intra-observer delineation consistency and is able to detect 4DCT artifacts. In dose evaluation using the DMH, density of the irradiated tissue is explicitly included in evaluation, so that dose evaluation is more closely associated with prospective models of cell damage. Optimizing RT plans using mass (and the DMH) has the potential to reduce radiation path lengths through normal tissue in order to increase dose in massive regions of the target. Optimizing dose-to-mass must be further investigated in order to properly account for geometric uncertainty.

7 Multi-Criteria Optimization for Lung Cancer

DVO – dose volume objective

MCO – multi-criteria optimization

FO – fixed objective

aCT – average CT image

MODA – multi-objective decision analysis

NTCP – normal tissue complication probability

OAR – organ at risk

PCA – principal component analysis

ROCO – reduced order constrained optimization

sim-min – simultaneous minimization

ilung – ipsilateral lung

clung – contralateral lung

COPD – chronic obstructive pulmonary disease

As presented in Section 2.5, radiotherapy (RT) optimization is a multi-objective decision which

necessitates assigning importance weightings to competing objectives in order to numerically

achieve an optimal solution. Modification of objective weights can lead to different optimal

solutions from the numeric optimization. However, the plan which truly optimizes the

therapeutic ratio for each patient does not necessarily correspond with the numerically optimal

solution for a predetermined set of weights. Ideally, the numerically optimal plan for a given set of objectives and objective weights will be a member of a class of solutions which are relevant for clinical delivery for a given patient. Throughout the history of RT, it has been the role of the planning team to identify a clinically acceptable and ideally optimal treatment plan. To navigate the multi-parameter numerical solution space, a clear and efficient method to present the patient-specific decision space is introduced in this chapter.

A numerical optimization, as described in section 2.5, relies on a set of input objectives and objective weightings in order to determine an optimal solution. Use of dose-volume objectives (DVOs) based on outcome data in a numerical optimization implies a treatment dose just below the DVO-level is equivalent to a treatment of zero dose. For example, minimizing lung volume at 20 Gy (V20) implies 100% of lung treated to 19.99 Gy is equivalent to 100% of lung at 0.00 Gy within the numerical optimization. This is one weakness of population-based, fixed DVOs. On the other hand, achieving fixed DVOs in lung cancer RT is often impossible for a given clinical objective which is truly the intent of treatment; including treatment of the target (e.g. the prescription to the target must be met in order to realize any benefit). The set of achievable DVOs depend on patient-specific geometry and may conflict with treatment intent.

In this ill-defined scenario, where population-based objectives are applied to patient-specific treatment, iterative human interaction and re-optimization guide decision making and ultimately determine the treatment plan. During the planning loop, the presented decisions often involve two or more conflicting objectives and, despite a lack of information about trade-offs for the patient-specific geometry and dose distribution, decisions are made which may influence the efficacy of treatment. This decision process leads to inherent variability in plan

quality (in terms of the therapeutic ratio) due to inter-patient variability and inter-institution variability among decision-makers. One approach to aid in the decision-making process is multi-criteria optimization (MCO), which is investigated in this chapter. MCO computes a collection of basis-plans which can reveal relevant objective-tradeoffs for patient-specific anatomy. If two more objectives tradeoff, a decision must be made regarding preference, this is a decision opportunity.

An advantage of utilizing population-based DVOs is consistency in delivered plans despite inter-patient heterogeneity, i.e. for a given protocol, everyone receives (approximately) consistent treatment. This approach often leads to unnecessary irradiation of healthy tissue but may assist in retrospective outcome analysis due to consistency in the dose-volume data. While this is of interest in determining the effects of RT and associated complications, the aim of this study is to increase the therapeutic ratio through minimizing dose to normal tissues. One method to accomplish this aim is to achieve Pareto efficiency between objectives, for every objective for every patient, which is an ethical approach to RT. Pareto efficiency means that an objective cannot be improved without sacrificing another objective, i.e. all objectives are minimized with respect to one-another. Conventional, fixed-objective (FO) optimization does not guarantee DVOs are Pareto-efficient if the DVOs are zero-valued. This chapter, consistent with aim 3 of this dissertation, describes the design of an MCO plan constructor which generates a basis-set of plans which approximate Pareto-efficiency. Patient-specific tradeoffs are identified through analysis of the basis set in Section 7.2 and often reduce patient-specific planning to a few decision opportunities.

The purpose of the basis-set is twofold, (1) to reveal the relevant region of the Pareto-efficient front for each patient and (2) to identify the OARs which present decision opportunities through identifying conflicting objectives. However, the MCO basis set of plans as described in section 7.2 are not guaranteed to be Pareto-efficient and may not reveal all relevant decision opportunities. Section 7.3 compares tradeoffs revealed in different MCO-basis sets generated using different DVOs. In section 7.3, MCO-basis plans and the decision opportunities based on different DVOs are compared.

Real-time planning through interpolation of the MCO basis set is described in section 7.4. The MCO plans are optimized on a single planning image (average-CT, aCT) for density estimation with static structures defined on the 30% phase image. However, variations in OAR dosimetry due to delivery of the MCO plan to time-dependent anatomy may compromise potential dosimetric benefits. Dosimetric variability due to delivery of different MCO plans to 4D-anatomy is estimated on a per-plan basis in section 7.4. While the MAO approach (described in Chapter 5) considers 4D- information in plan design a-priori, MCO enables plan variation in real time and therefore can consider 4D-information a-posteriori without necessitating numerical re-optimization.

The MCO model developed in this work is implemented for four LA lung cancer patients under the premise that a simple model of the patient-specific decision space is superior to a complex one. MCO has the potential to transform modern radiation therapy treatment planning from a complex combination of conflicting decisions to a very efficient and conceptually clear decision space (or set of decision opportunities) which can be navigated in real time.

7.1 PARETO EFFICIENCY AND MULTI-CRITERIA OPTIMIZATION

Several authors have investigated Pareto-efficiency for RT objectives and MCO for RT planning. MCO has been introduced clinically through the RayStation™ (RaySearch Labratories, Stockholm, Sweden) treatment planning system, but methods of construction of an MCO basis-set are not yet clear. There is not a universally accepted method of generating an MCO-basis set.

7.1.1 Background

Multi-objective decision analysis (MODA) and Pareto-efficient optimization of radiotherapy plans has been discussed by several authors.[157–162] Considering the RT problem in the context of MODA, Yu[157] designed a ranking system for plans according to objective weightings defined by the decision-maker (designated as the physician in the rest of this document). The method computed a family of solutions with rankings determined by interpretation of the physician's intent and, essentially, automated the planning loop. Cotrutz *et al.*[158] solved for a family of RT solutions based on objective weight variation, allowing the physician to select a plan which meets the treatment objective.

The method of generating the MCO basis set presented herein, similar to Yu[157], uses concepts from MODA regarding utility and preference. However, the goal of this work is not to make decisions (or automate decision making), but to present a clear and efficient decision space to the physician. This is more consistent with the goal of Cotrutz *et al.*[158] but they considered tradeoffs between the target-dose and the sum of normal tissue complication probabilities

(NTCPs) for all organs at risk (OARs). In the method presented in section 7.2, target-dose and target-dose homogeneity is a constraint for all patients so the relevant decision space is only with respect to OAR dosimetry.

The decision opportunities revealed by an MCO-basis set may depend on the method of generating the basis set. Craft *et al.*[159] investigated the variation in basis plans optimized with maximum- and mean- dose objectives under the hypothesis that, if the solution space is similar for these different objectives, then "they should be similar for other cases as well." Their findings reveal an important characteristic of Pareto efficient solutions and independence with respect to the objectives used to estimate them; using their words, "any two functions which are positively correlated are the same in terms of the generation of the Pareto surface."[163] Romeijn *et al.*[83] presented a general method for MCO and rigorously prove the independence of the revealed Pareto-efficient front with respect to convex objective functions combined with linear operators. In section 7.3, several MCO bases are generated using different objectives in order to estimate proximity to the Pareto-efficient front and the consistency in revealed decisions.

Several other studies have investigated MCO for RT planning and included plan interpolation for real-time planning.[164–168] Craft and Bortfeld[165] estimated the number of basis plans required to perform real-time planning with interpolation without significantly departing from the Pareto frontier; they found that $N+1$ plans, where N is the number of objectives, is typically sufficient. Monz *et al.*[164] investigated interactive updates of basis plans in order to remain near the Pareto front and ensured interpolated plans do not deviate from Pareto efficiency. Ensuring Pareto efficiency of solutions is important; it ensures the solutions minimize objectives. However, the

hypothesis of this dissertation is that a clear and concise presentation of patient-specific decision-opportunities is more important, and will have more impact on conventional RT planning, than ensuring Pareto-efficiency for all objectives for all plans.

In order to create a more concise and clear decision space, Spalke *et al.*[169] reduced the MCO basis set of plans via principal component analysis (PCA) and via the isomap method for the set of optimized fluence vectors. Stabenau *et al.*[170] also reduced the number of basis plans generated via Reduced Order Constrained Optimization (ROCO) using PCA of the fluence vectors. Both of these studies considered variation in the beamlet space in order to determine an efficient representation of the patient-specific decision-space. Variability in vectors of beamlet fluence is of interest for computational efficiency, but the OAR-dosimetry in terms of the evaluation metrics used to determine plan quality, i.e. the DVH, is the quantity of interest in the relevant decision space. The basis plans described herein are designed in order to reveal tradeoffs in OAR-dosimetry, which is evaluated with the DVH, while approximately minimizing objectives.

7.2 MULTI-CRITERIA OPTIMIZATION FOR RADIATION THERAPY OF LUNG CANCER

Multi-criteria optimization (MCO) is used to form a model of the patient-specific decision-space for four locally advanced lung cancer patients. The method is implemented in the Pinnacle[3] TPS using the ORBIT optimization engine.[78] The MCO basis set of plans is constructed based on weight variation of a set of DVOs. The basis set forms a model of the relevant patient-specific decision space for each patient.

7.2.1   Estimating the Patient-Specific MCO Basis Set

The goal of radiation therapy is to maximize the therapeutic ratio, i.e. maximize the tumor control probability (TCP) and minimize the normal-tissue complication probability (NTCP) for all normal tissues. The utility of each radiotherapy plan (U), labeled by the vector of the beamlet weightings $\vec{b}$, can be expressed

$$U\left(\vec{b}\right) = w_1\, TCP\left(\vec{b}\right)\ +\ w_2\, NTCP\left(\vec{b}\right) \qquad\qquad 7.1$$

The first term in the sum, the TCP, is conceptually simple. The TCP is determined according to treating the target to a prescription dose; it is the intent of treatment and in this work is considered a constraint. In order to estimate the second term, the NTCP term, each OAR must be compared to other OARs in terms of importance and the impact of each of the possible OAR complications must be weighed against patient-specific quality of life, for each patient. The weights of the TCP and NTCP terms, w_1 and w_2, specify the importance of TCP with respect to NTCP, i.e. how important is tumor control as compared to complications on quality of life.

The estimated NTCP for each irradiated OAR can be used to estimate and assign a weight (or ranking) to each OAR ($w_{OAR\text{-}i}$) with respect to other OARs.

$$NTCP\left(\vec{b}\right) = \sum_{i \in N_{OARs}} w_{OAR\text{-}i} NTCP\left(OAR_i\right) \qquad\qquad 7.2$$

An individual plan, with beamlet vector $\vec{b}$ can be expressed through a value hierarchy, or utility assessment, of the TCP and the NTCP of each OAR, as illustrated in Figure 28.
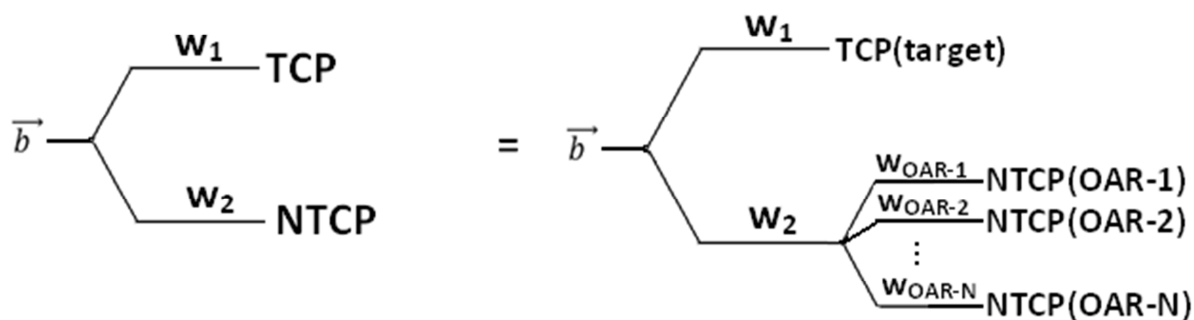
Figure 28. A value hierarchy to represent utility of a radiotherapy plan designated by a beamlet of vector weights $\vec{b}$ in terms of tumor control probability (TCP) and normal tissue complication probability (NTCP). The NTCP term can be difficult to estimate when multiple OARs are considered.

The beamlet vector, as indicated in Figure 28, has utility determined by importance weightings and values of TCP and NTCP. The objective function which is minimized during numerical optimization should be a numeric representation of the utility function for each $\vec{b}$. Expressed as a weighted sum of *N* objectives consistent with equation 2.1, the objective function is:

$$O\left(\vec{b}\right) = \sum_{n \in N} w_n f_n\left(\vec{b}\right) \qquad 7.3$$

According to equation 7.1 and 7.2, the weight factors in the objective function for the OARs are $w_n = w_2 \times w_{OAR-n}$ for each OAR, i.e. the importance weighting for each OAR must consider the benefit of TCP versus NTCP and the importance of each OAR to overall NTCP. The decision variable is the vector of beamlet weightings, $\vec{b}$, and the objectives are one-sided, least-squares penalty functions in dose ($\vec{d} = \hat{K}\vec{b} \geq 0$, where $\hat{K}$ is the matrix of dose deposition coefficients) with tolerance (or prescription) D_n^{Rx}.

$$f_n\left(\vec{b}\right) = \sum_{i \in n} c_{i,n} \left(\hat{K}\vec{b} - D_n^{Rx}\right)^2.$$

All *N* of the objectives contribute to the objective function and influence the "optimal" solution. According to the results of Craft and Bortfeld,[165] an *N* objective MODA problem can typically be described by *N+1* MCO-basis functions. The Pareto front for the objective function in equation 7.3 is *N*-dimensional with *N* degrees of freedom.

Consideration of an *N*-dimensional Pareto front (where *N* is the total number of objectives) is not a desirable approach for implementation of MCO for RT planning. The goal of this work is to create an efficient and conceptually clear decision environment, and the *N*-dimensional Pareto front fails in both efficiency (it is not efficient to consider every variable in the RT problem when designing an MCO database) and in conceptual clarity (very few people can envision an *N*-dimensional surface). Rather than consider the Pareto-front of the objective function described in equation 7.3, consider a decision space where a preference for the ith and j^{th} vector of beamlet weightings is written.
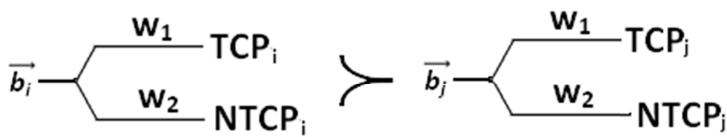
The utility of the ith beamlet vector, $\vec{b}_i$ (which labels the optimized plan), only needs to be considered in the context of other acceptable plans; this does not necessarily include the entire *N*-dimensional Pareto-front. This more compact representation of the decision space should be expressed in the numerical optimization of the objective function when generating the MCO basis set. The set of *N* objectives are divided into three subsets: (1) N_{hc} hard constraints each

with weight w_{n-hc}, which, if not met render a plan invalid, (2) N_{sc} soft-constraints (or goals, described in detail later) each with weight w_{n-sc}, and (3) N_o objectives with weights w_{n-o}. The objective function is now

$$O\left(\vec{b}\right) = \sum_{n \in N_0} w_{n-o} f_{n-o}\left(\vec{b}\right)$$

such that

$$min\left(\sum_{n-hc \in N_{Hc}} w_{n-hc} f_{n-hc}\left(\vec{b}\right) + \sum_{n_{sc} \in N_{sc}} w_{n-sc} f_{n-sc}\left(\vec{b}\right) \right)$$

For the locally advanced lung cancer patients considered in this study, the set of (three) hard constraints are (1) the prescription dose to the target, PTV-D_{95}>70 Gy, (2) maximum dose to the target, PTV-D_{max}<80 Gy, and (3) spinal cord D_{max}<45 Gy. It is interesting to note that the formulation is actually independent of the magnitude of the prescription dose constraint, an arbitrary prescription dose can be achieved through scaling plan monitor units (MUs) and dose to OARs can be expressed as a fraction of the prescription; this is shown in section 7.4. If any of the three hard constraints are violated for any given plan, the solution is invalid and is not considered in the MCO-basis set. These hard-constraints define the solution space (or the relevant region of the Pareto-efficient front) for each patient and can be considered on a patient-specific basis. The utility of the hard constraints is constant (**C**) across all plans and combine to form a constant prospect,[171] so that a preference relation between plans depends only on the remaining soft-constraints and objectives. The weight factors which balance TCP and NTCP no longer need to be considered. The constraint on the target dose, PTV-D_{95}>70 Gy determines the TCP, so that the preference relation between plans only depends on NTCP:
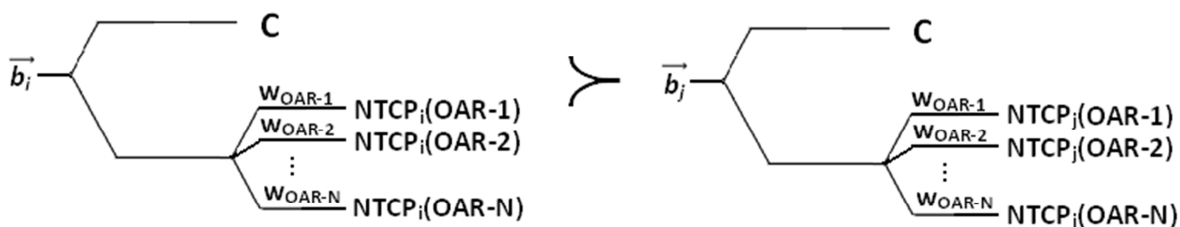
In order to further reduce the complexity of this decision, the set of soft constraints (or goals) are also defined as part of the constant prospect (**C**). The soft constraints avoid hotspots in normal tissues. In order to express this desirable feature of lung cancer RT plans in the objective function, for each OAR and for the entire body minus the PTV, objectives are included which minimize D_{max}>35 Gy. If an OAR overlaps the PTV, the objective is varied to minimize D_{max}>63 Gy (90% of prescription). Soft constraints on D_{max} are included for both the entire body minus PTV and each OAR, which overlap, in order to place additional emphasis on reducing hotspots in OARs. Another desirable feature of lung cancer RT plans is increasing the minimum PTV dose towards prescription, i.e. minimize PTV-D_{min}<70 Gy, and while many plans attempt to prescribe to D_{min} (or D_{99}), this prescription is often only achievable after altering the PTV regions which overlap OARs. In this work, all regions of the PTV are simultaneously considered PTV and OAR in terms of optimization. Assuming the set of soft constraints compose an approximately constant prospect across different plans, the decision space now depends on four objectives (N_0 = 4). Preference between plans now depends on NTCP of each lung, esophagus, and heart,
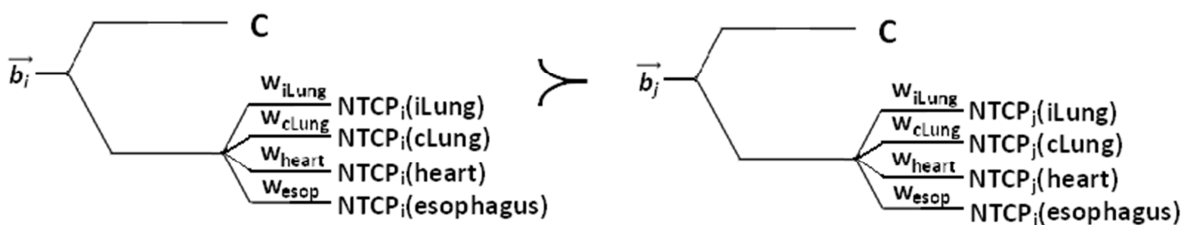
For these four OARs, potential trade-offs (or decisions) are identified based on analysis of basis plans resulting from weight variation on these objectives. Five basis plans are designed for each patient and approximate Pareto efficiency between DVOs for the ipsilateral lung (ilung), the contralateral lung (clung), the esophagus, and the heart.

Five plans are computed per patient and together form the MCO-basis set, they are computed by (1) simultaneously minimizing all four DVOs (called sim-min plan) and (2-5), for each DVO, one weight is varied by a factor of 10^{-3}. The resulting five plans are labeled by (1) sim-min and (2-5) the OAR plans (ilung-plan, clung-plan, esophagus-plan, and heart-plan). These five plans create the patient-specific basis set where, for each OAR plan one OAR is sacrificed in order to reveal a potential improvement in the DVH of some other OAR. If there is no improvement for a given OAR plan with respect to the sim-min plan, then the corresponding OAR does not trade-off and is not a decision variable in the problem.

Generating the five-plan basis set is accomplished with a 3-step sequential optimization. Step 1, the initialization step, is optimized for 20 iterations with $w_{n-hc}=100$, $w_{n-sc}=1$, and $w_{n-o}=0$. The purpose of the initialization step is to bias the solution to meet the set of (hard and soft) constraints. Step 2, the weight-variation step, the DVO weights are increased from zero to either 1.0 or 0.001, depending on the plan (e.g. in the sim-min plan, $w_{n-o}=1$ for all DVOs, in the ilung plan, $w_{ilung}=0.001$, etc.). The weight variation step is performed five times, once for each basis set, and is optimized using a large number of iterations (e.g. 100). This step establishes trade-offs between the DVOs. In step 3, the re-normalization step, the weights of both the DVOs and the soft constraints are reduced by 2-3 orders of magnitude and the plan is re-optimized (20 iterations) to ensure the hard constraints are met. Step 2 and 3 are repeated for

each DVO in order to form each basis plan, which is stored as a vector of beamlet weights. The

flow chart is shown in Figure 29.
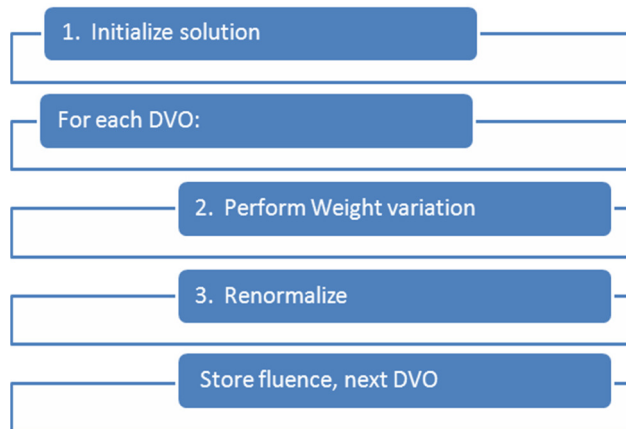
Figure 29. Flow-chart for generation of the MCO basis set. The initialized solution is input for each DVO basis plan, which are determined by weight variation (to reveal trade-offs) and renormalization (to ensure the plan meets the hard-constraints).

Steps 2 and 3, the weight variation and renormalization steps, are used to uncover tradeoffs

between OARs given the constraints of the problem. The sequential optimization, as

introduced, may not be necessary to unveil potential tradeoffs. Another plausible approach is

to use an interior point method (see e.g.Nocedal and Wright,[79] Chapter 14) which will render all

solutions which violate the hard constraints unfeasible. However, this approach limits the

search space and may conceal potential tradeoffs. By allowing the hard constraints to vary

during the weight variation step, the feasible search space is expanded to solutions which do

not meet the hard constraints of the problem. When the plan is renormalized, the solution will

either converge to an approximate equivalent solution to the sim-min plan (and a tradeoff is

not identified) or it will converge to a new solution which reveals a potential trade-off.

The sim-min plan is the reference point for identifying decision opportunities, if a basis plan

reduces an OAR DVH-levels compared to the sim-min plan, then a tradeoff is present.

Evaluation of the set of basis plans, for each patient, reveals which organs trade-off and clarifies

which decisions opportunities are available to the physician. Automated determination of trade-offs can be employed to further reduce the problem to as few as two plans (assuming at least one trade-off is identified), but may not be necessary (i.e. analysis of four plans is sufficiently clear to be useful clinically).

The four locally advanced patients included in this chapter, P6-P8 and P10, each present a unique tumor location. P6 presents a right, central upper lobe cancer with hilar involvement. P7 presents a left-lower lobe tumor with central and peripheral components; the tumor extends from the lower airway to the left diaphragm. P8 presents a right central tumor abutting the heart and esophagus, and P10 presents a right, central- lower lobe cancer. Each MCO data-base is optimized using the average- 4DCT density (aCT) and structures defined on the 30%-phase image. The PTV is a union of the phase-defined CTVs without consideration of setup error (i.e. PTV=ITV).

The basis plans and decision opportunities are presented for each patient. The basis plans are also compared to a fixed objective (FO) optimization which achieves identical target coverage, PTV-D_{95}>70Gy, but uses fixed DVOs including ilung and cLung V20<30%, esophagus V55<30%, and heart V40<50%.

7.2.2 Results: Identifying Patient-Specific Decision Variables

The five basis plans for both P6 and P7 show two decision opportunities based on trade-offs between iLung and esophagus and iLung and heart. The sim-min and iLung plan DVHs for P6 are compared in Figure 30. Compared to the sim-min plan, this is the only basis-plan which shows potential dosimetric improvement in any OAR. The decision opportunity for this patient

is a single variable, increase the ilung-DVH in order to decrease heart and esophagus dose or increase heart and esophagus dose to reduce dose to iLung. Esophagus V20 varies from 7% to 37% between MCO plans, however this increase in esophagus-volume corresponds with a negligible (<1% volume) decrease in iLung-V20. A plot of the tradeoffs in mean-dose (<D>) for iLung, compared to esophagus, heart, and

clung is shown in Figure 31, a small increase in iLung mean dose (0.5 Gy) results in a decrease of esophagus mean dose by nearly 5 Gy, whereas heart mean dose is reduced by approximately 2 Gy when increasing ilung mean dose by 3 Gy.
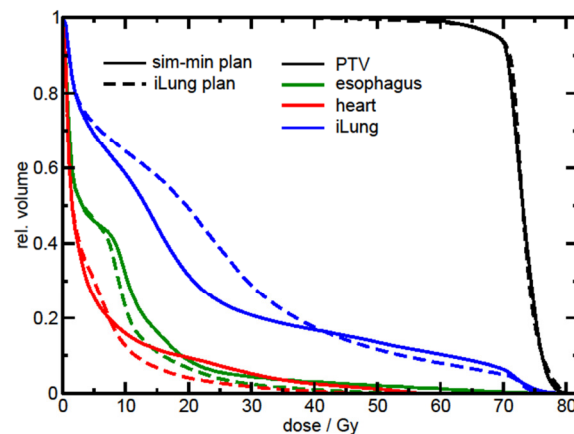
Figure 30. Comparison of the plan which simultaneously minimizes the four dose-volume objectives and the plan which relaxes ipsilateral lung (iLung) reveals tradeoffs between iLung and heart and esophagus.

The FO plan for P6 results in zero-valued objectives for cLung, esophagus, and heart. Delivering the FO plan would irradiate 20% of the esophagus to 40 Gy, compared to 4% in the sim-min plan and 1% in the ilung plan. By presenting the basis set to the physician, it is evident that iLung-V20 cannot be reduced to less than 31% volume without degrading target coverage, however esophagus and heart sparing is possible by increasing iLung V20 to above 31% volume. or P7, a similar decision is evident from the MCO basis set. The iLung trades-off with heart and esophagus as shown in Figure 32. This patient presents an invasive tumor plaguing a large volume of the lung, so that treating a larger region of ilung in order to spare both heart and esophagus may be desirable. The remaining basis plans, together with the sim-

min plan are plotted in Figure 33. Compared to the sim-min plan, the clung-, esophagus-, and,

and heart- plans do not show potential to spare OARs.
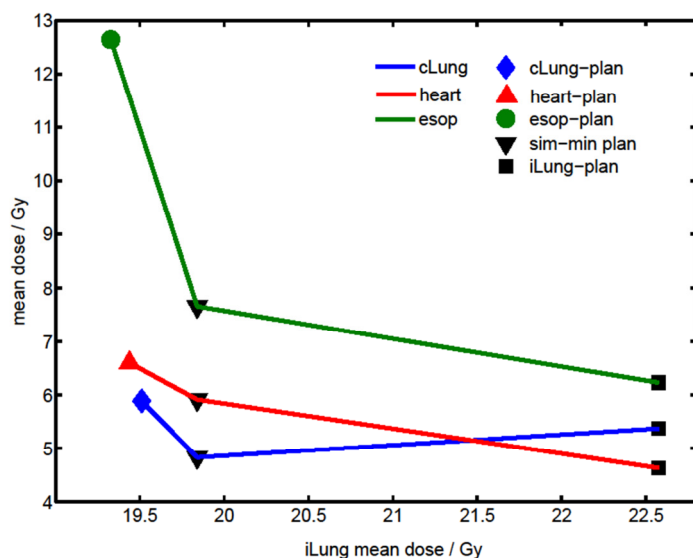
Figure 31. A tradeoff in mean-dose between ipsilateral lung (iLung) and esophagus (esop) and ilung and heart is clear, whereas contralateral lung does not trade off with ilung.
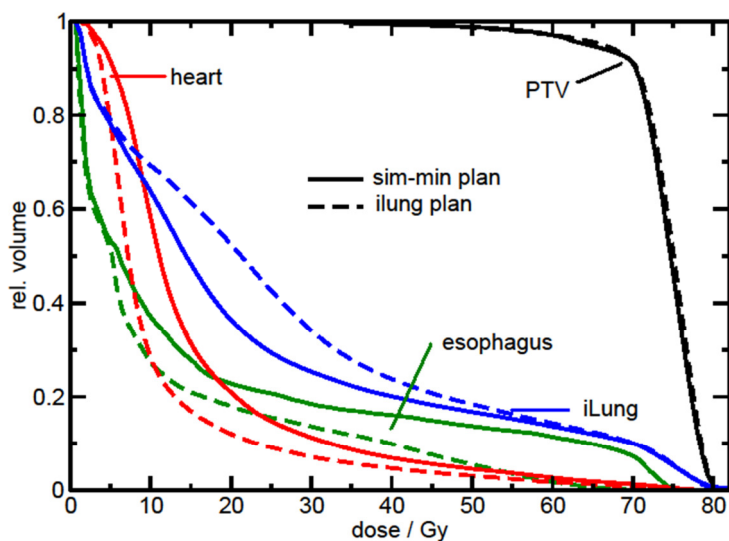
Figure 32. The sim-min and iLung basis plans are reveal tradeoffs between ilung and esophagus and heart.

Patient 8 (P8) presents a right-central tumor and the PTV overlaps both heart and esophagus.

Similar to P6 and P7, one trade-off is evident for this patient. Increasing iLung-V20 from 24% up to 30% corresponds to a reduction in cLung from 23% to 17%. Variations in esophagus and heart volumes at all dose levels in basis plans for P8 are <3%. By using the MCO plans, cLung V20 can be adjusted, in real time, from 29% (where a

Figure 33. Multi-criteria optimized (MCO) basis plan DVHs are shown for patient 7. The OAR plans do not show improvement in any OAR dose compared to the sim-min plan, and no tradeoff is evident for these OARs.

V20<30% objective results in zero DVO penalty) down to 17% volume. The MCO plans based on ilung and clung are shown in Figure 34 (dashed DVHs) and are compared to the FO-optimized plan (solid DVH).

For the fourth patient considered, P10, decision opportunities are evident between iLung and cLung and iLung and heart. An increase in iLung-V20 from 29% to 49% reduces V20 in cLung from 15% to 9%. Heart V20 is reduced by 6% volume, from 19% to 13% for the same shift iLung V20 (29% to 49%). Conversely, an increase of heart-V20 of 35% (from 19% to 54%) results in a reduction of iLung-V20 of 3% (from 29% to 26%). The tradeoffs for Patient P10 are described in more detail in the section 7.3.

Figure 34. Patient 8 MCO basis plans for ipsilateral lung (iLung) and contralateral lung (cLung), compared to a fixed-objective plan. The MCO plans allow >5% in iLung and cLung V20.

7.2.3   Summary: Identifying Patient-Specific Decision Variables

Basis sets reveal at least one decision to be made by the physician regarding OAR sparing for

each patient. This decision in 2/4 cases involved trade-offs between two OARs, so that the

decision between plans depends on the physician's weighting of 2 OARs. Rather than attempt

to automate the decision making, the physician is permitted to interactively view the tradeoffs

while balancing other variables, such as patient-specific quality of life, in order to determine the

delivered plan. For example, a decision to increase dose to ilung in order to spare esophagus was revealed for 3/4 patients. If the patient presents complications in breathing, e.g. due to chronic obstructive pulmonary disease (COPD), perhaps lung dose should be minimized at the cost of increased dose to the esophagus. In other cases the decision may be very obvious, e.g. the 5 Gy decrease in esophagus mean dose at the cost of a 0.5 Gy increase in ilung mean dose evident in P6. Compared to fixed-objective optimization, MCO methods have the potential to spare regions of OARs at all dose levels.

7.3   OBJECTIVE DEPENDENCE IN MCO BASIS SOLUTIONS

The basis sets described in the previous section are not guaranteed to exist on the Pareto-front, in fact is it is unlikely that they do. However, the plans may get "close-enough" to produce a solutions which capture plan variation due to conflicting objectives relevant to possible decision opportunities. Assuming all objectives with positive correlations will converge to the same Pareto surface, this section compares MCO basis plans optimized using different DVOs for one patient (P10). The goal of this section is to show the approach of MCO-basis estimation presented in section 7.2 captures relevant plan variability, independent of the chosen objectives. There will always be some level of objective dependence by setting a dose or dose-volume tolerance (or prescription) level >0 Gy or >0% volume; this is because all voxels which meet this tolerance are ignored. This creates non-linear response in the objective function about the prescription tolerance dose.

Consider a dose-volume objective for an ROI labeled by the index n, defined according to equation 2.2,

$$f_n = \sum_{i \in n} c_{i,n} \left(d(i) - D_n^{Rx} \right)^2 \text{ with } c_{i,n} = \frac{\Pi \left(\mp d_i^{acc} \pm D_n^{Rx} \right)}{\left(D_n^{Rx} \right)^2}$$

(assuming the volume prescription level, $V_n^{Rx} = 0$). The objective function response due to variation of the prescription dose (D_n^{Rx}) depends on the number of voxels in the ROI at or below the prescription dose. Consider $D_n^{Rx} \to D_n^{Rx}/2$, then

$$f_n \to f_n + \frac{1}{\left(D_n^{Rx} \right)^2} \sum_{\left(i \, | \, D_n^{Rx} > d(i) > D_n^{Rx}/2 \right)} \left(d(i) - \frac{D_n^{Rx}}{2} \right)^2 + \frac{1}{\left(D_n^{Rx} \right)} \sum_{\left(i \, | \, d(i) > D_n^{Rx}/2 \right)} \left(d(i) - \frac{3}{4} D_n^{Rx} \right)$$

This non-linear response of the dose-volume objectives, due to the Heaviside operator, implies that numerically optimized solutions using different dose-volume objectives may not converge to an equivalent Pareto surface.

In order to estimate MCO-basis variation with respect to varying planning objectives, the five MCO basis sets described previously are generated for four different sets of DVOs: (1) minimize V10>20%, (2) minimize V5>10%, (3) minimize *gEUD*(*a*=2)>0 Gy, and (4) minimize D_{max}>0 Gy (i.e. minimize all dose in all voxels). The *gEUD*(*a*=2) approach is consistent with the recommendation of Craft[172] for MCO as implemented in the RayStation™ treatment planning system. Both the *gEUD*(*a*=2)>0 Gy and D_{max}>0 Gy objectives penalize all voxels in each OAR with dose >0, but *gEUD*(*a*=2) penalizes higher dose levels quadratically. DVHs are compared for the different sets of bases, and the approximate Pareto surface is displayed graphically for objectives which trade-off.

7.3.1   Results: MCO Basis Variation Based on Different Objectives

The collection of DVHs for all MCO basis sets, based on optimization with different dose-volume objectives for each OAR, is shown in Figure 35. Also included with each basis set are the FO-optimized DVH curves. The basis sets optimized with different objectives are similar but not identical for the patient considered. Using the $gEUD(a=2)$ and D_{max} objectives (which penalize every voxel with non-zero dose) led to reduced DVHs compared to MCO-bases generated using V5 and V10 objectives for heart and clung, but not for ilung. Minimum DVHs for ilung (by trading off with heart in the heart-plan) were uncovered in the $gEUD$- and V10- MCO-bases but minimum DVHs are not evident from the V5 and D_{max} MCO-bases. The decision space, based on OAR trade-offs, also varies based on the chosen DVOs.

Figure 36 compares the sim-min and ilung plans using V10 and $gEUD$ objectives. The $gEUD$-bases show the potential to increase ilung dose beyond what is evident in the V10 plans in order to reduce (or approximately minimize) dose to esophagus and heart. On the other hand, D_{max}-bases failed to reveal decreases in ilung dose through increasing heart dose. One tradeoff was clear in all MCO basis sets independent of chosen DVO, increasing dose in ilung decreases dose to other OARs.

Mean dose (<D>) to ilung is plotted as a function of heart <D> for all MCO-plans in Figure 37. The approximate Pareto-efficient front using just three MCO-bases are also plotted in Figure 37 using the heart, sim-min, and ilung plans. The four curves differ depending on the objectives used. Plans optimized with Dmax did not achieve minimum ilung <D> compared to other MCO-basis sets (minimum ilung <D> = 18.93 Gy compared to 17.86 Gy in the gEUD plans) but did

achieve minimum heart <D> (reduced to 5.6 Gy in the Dmax plans compared to 11.47 Gy in the

V10 plans).
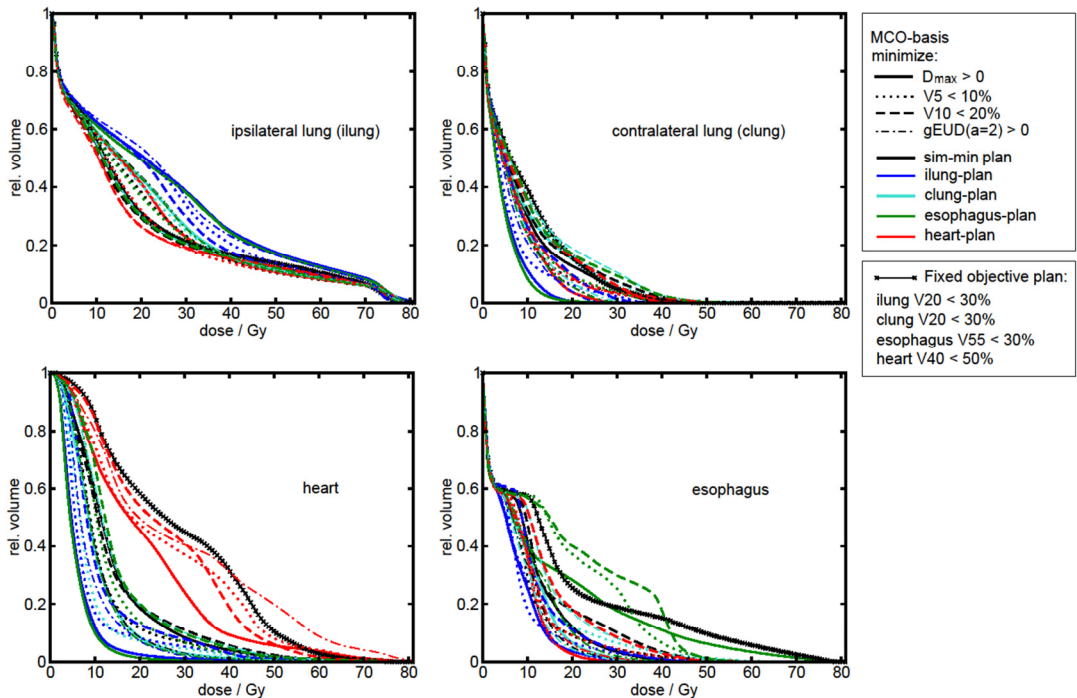
Figure 35. Dose-volume histogram (DVH) variation for each OAR based on different MCO-basis sets (computed by minimizing different objectives) and a fixed-objective optimized solution. MCO-bases were similar, but not identical for different objectives.
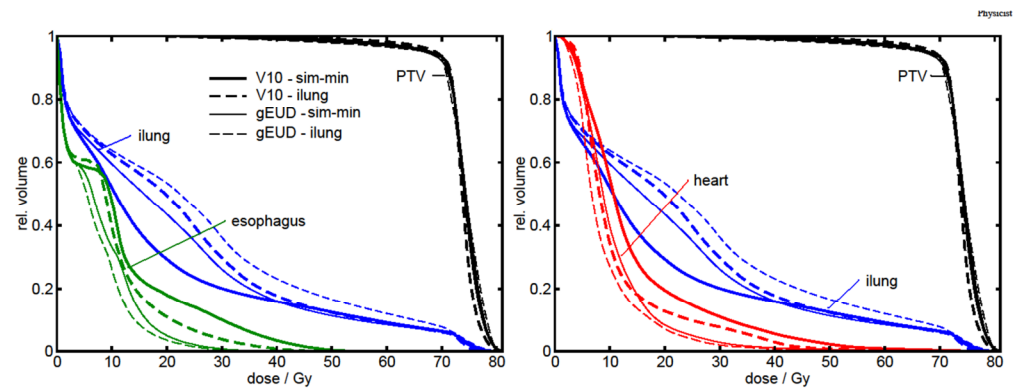
Figure 36. Multi-criteria basis sets using V10>20% and *gEUD*(*a*=2)>0 objectives. The *gEUD* basis sets reveal potential to reduce esophagus and heart dose compared to the V10 basis set at the cost of higher ipsilateral lung dose.

The approximate Pareto-efficient front varies depending on which objectives are chosen, but may also depend on the evaluated dose-volume metric. Mean structure dose was not optimized in any of the plans but clearly shows tradeoffs in ilung and heart. Using dose-volume based evaluation metrics, Figure 38 plots relative structure volume as a function of volume of ilung at 20 Gy (top left), 10 Gy (top right), and 5 Gy (bottom right). Among the plans considered, gEUD-based optimization (labeled with circles) reveals minimized ilung volume at all three dose levels, with V10-objectives finding similar values for V20 (≈0.26) and V10 (≈0.52). Conversely, only D_{max}-based MCO plans reveal minima in heart and clung at all three dose levels.
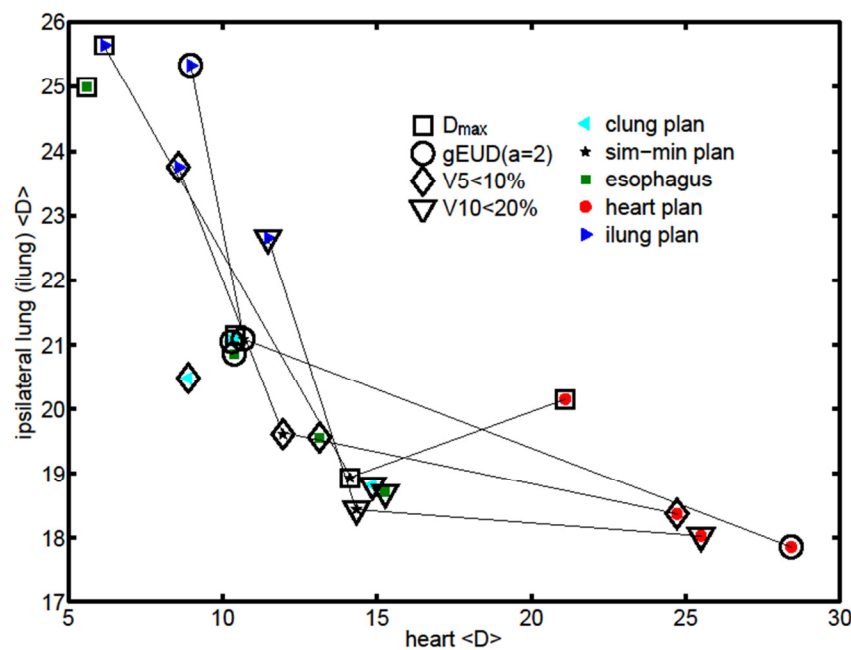
Figure 37. Mean dose <D> to ipsilateral lung (ilung) as a function of heart <D> for 20 plans, five multi-criteria optimization (MCO) basis plans for four objectives. The approximate Pareto-efficient front using three basis plans, each optimized using different objectives, are shown with lines.
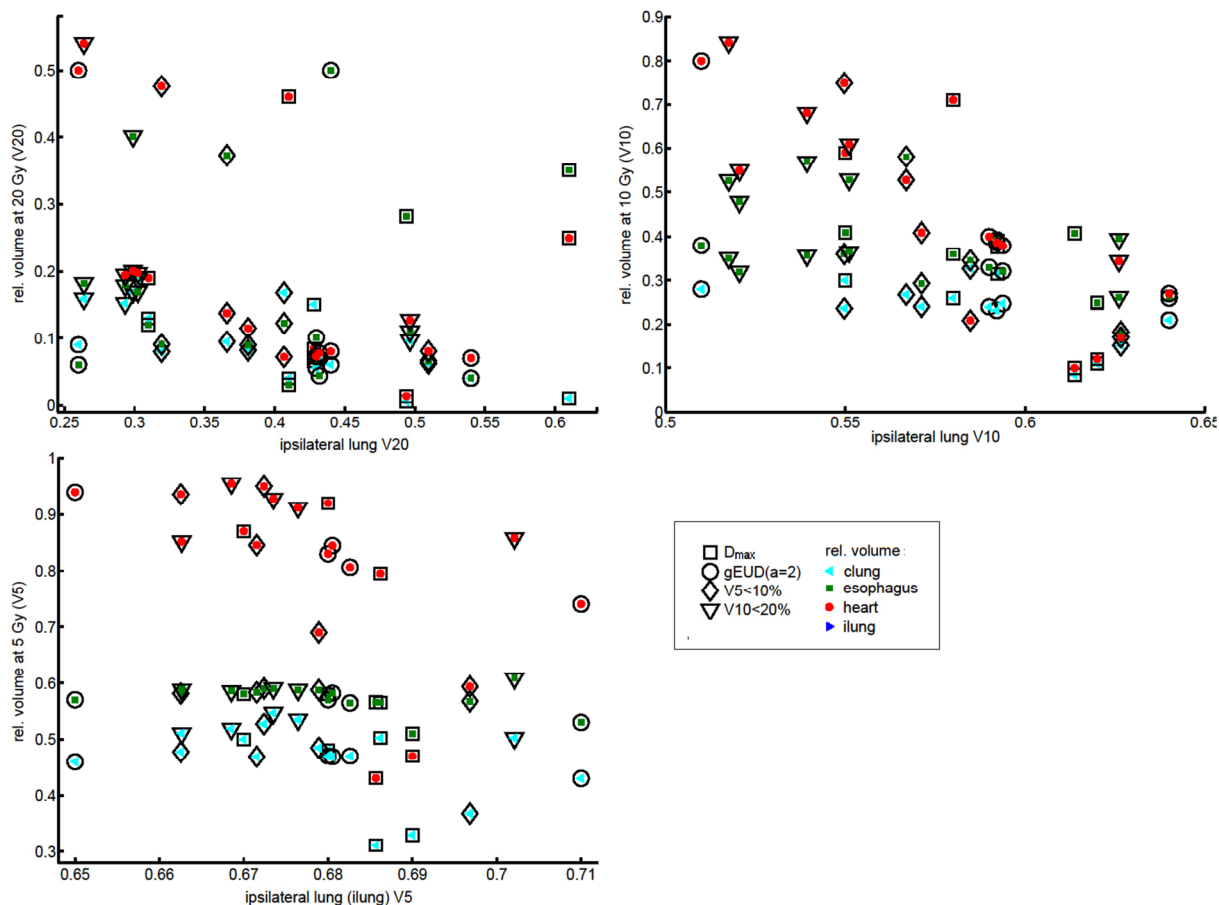
Figure 38. Relative volume at three different dose levels for heart (red circle), esophagus (green square), and contralateral lung (blue) as a function of ipsilateral lung volume at fixed dose. The plans are each optimized with different objectives as part of an MCO basis set.

Utilizing a fixed prescription dose or volume level, e.g. minimizing V5 or V10 at a given OAR volume, does not imply the resulting plan will minimize this dose metric. In fact, for every structure, the MCO plans optimized based on V5<10% did not reveal minimum V5 levels. This was also the case in all V10<20% plans at V10 levels. For example, optimizing V10<20% in clung results in five MCO-basis plans with V10>26%, however every other set of basis plans (which use lower-valued prescription) result in clung-V10<15% in at least one plan.

7.3.2   Summary: Objective Dependence in MCO Basis Sets

The MCO basis set is designed to reveal relevant dosimetric variation for each patient while maximizing the therapeutic ratio. This section shows that the dose-volume information conveyed by an MCO-basis set depends on the dose-volume metrics used to optimize the plans. Part of this variation is due to bias introduced by objectives with non-zero tolerance (or prescription) dose. Dose volume objectives with non-zero tolerance levels should not be expected to reach global minima for metrics such as mean dose. Through minimization of dose to every voxel of every OAR, using e.g. a D_{max} objective, minimum dose volumes in heart and clung were revealed, but these objectives failed to achieve minima in ilung. Using $gEUD(a=2)$ objectives increases the importance of high voxel doses and did achieve minimum dose to ilung, but did not reveal potential sparing in clung and heart.

The results of this section suggest an objective function comprised of different objectives (much like what is used in conventional, FO-optimization) may be appropriate in construction of an MCO basis set. Using an objective which penalizes all dose (e.g. minimization of D_{max}>0 Gy) may be appropriate in structures expected to receive low dose. For structures in close proximity to, or overlapping the target, a non-zero dose-volume prescription tolerance or $gEUD(a=2)$ may be more appropriate. Further studies are needed which model objective response as a function of dose-variation.

7.4   PLAN ROBUSTNESS ON 4D-ANATOMY

Interpolation of MCO basis sets allows real-time planning and decision making through estimating dose as a linear interpolation of basis-plan doses. However, the basis set doses are computed on single planning-images and assume static structures as defined on the 30% phase image. Variations in OAR dosimetry due to delivery of the MCO plan to time-dependent anatomy may compromise potential dosimetric benefits or invalidate potential tradeoffs. This section details dosimetric variations due to delivery of the MCO plan on 4DCT phase images and moving, deforming structures for one patient.

The MCO basis-set of plans enables prospective analysis of the effects of delivering varying plans to time-dependent anatomy. Dose variation as a function of respiratory phase can be accomplished through dose calculation on each phase image, or using the static dose-cloud approximation.   The advantage of the latter approach is that it enables real-time evaluation of plan robustness to 4D-anatomy, whereas dose computation on several phase images is more difficult (or impossible) to achieve in real-time. The static dose-cloud approximation enables a fast evaluation of plan (or dose) sensitivity with respect to variability in OAR-definition as a function of respiratory phase. Dose computed on each 4DCT image and evaluated on structures defined in each 4DCT phase reveals variations due to the combined effects of OAR- and density- variations with respect to respiratory phase.

The basis set of MCO plans for P6 are evaluated on 4DCT respiratory phases in order to estimate plan robustness with respect to time-dependent anatomy. Because MCO allows plan variation in real time, the effects of delivery to time-dependent anatomy can be considered in

the plan selection stage (i.e. after the basis set is computed). Plans which result in minimal variations in evaluation metrics such as mean-dose or volume-at-dose, as a function of respiratory phase, are robust to uncertainty due to respiratory motion. By considering time-dependent anatomic variations in the planning stage of radiotherapy, a confidence interval on acceptable anatomy and/or plausible dosimetry, for a given treatment plan, can be established before treatment begins.

7.4.1 Results: MCO plans on 4D-Anatomy

The MCO basis sets for P6 reveal potential tradeoffs between esophagus and ilung. Figure 39 shows the ilung plan evaluated on the structures defined in each 4DCT assuming dose is independent of density variations (left) and computed on each phase image (right). The ilung V20 varies from 47% in the inhale (00%) phase image up to 57% in the 60% phase. Computing dose on each phase indicates ilung V20 varies from 44% in the 00% phase to 53% in the exhale phase (50%). The MCO ilung plan, computed on aCT predicts ilung V20 is 54%, consistent with the value computed on the exhale phase image.
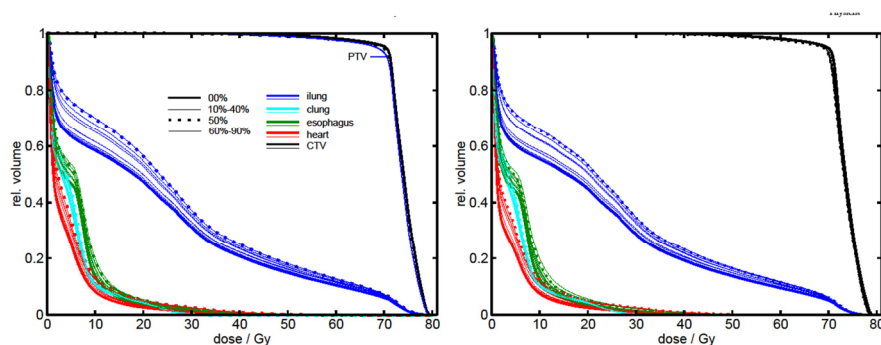
Figure 39. The MCO ilung plan evaluated (left) and computed (right) on ten 4DCT phase images. The inhale phase (thick, solid lines) and the exhale phase (thick, dashed lines) approximately bound the DVH's in all other 4DCT phases.

Volume at 20 Gy (V20), whether evaluated using the static dose-cloud approximation or computing dose on each phase image, is approximately constant for esophagus (<1.5% volume variation), heart (<2.5% volume variation), and clung (<1.0% volume variation) in this basis set. The CTV dose, irrespective of evaluation, is also approximately constant. This implies that theses parameters are robust to 4D-anatomic motion.

The esophagus-plan decreases ilung V20 at the cost of increasing dose to the esophagus. Evaluation of the MCO-plan on the ten phase 4DCT contours (assuming the static dose-cloud approximation) shows ilung, heart, and esophagus volumes vary by 3-5% at all doses from 10-30 Gy. This implies that the esophagus MCO plan is less robust to inter-phase variations than the ilung plan. Figure 40 shows this plan evaluated on all of the phase-contours.
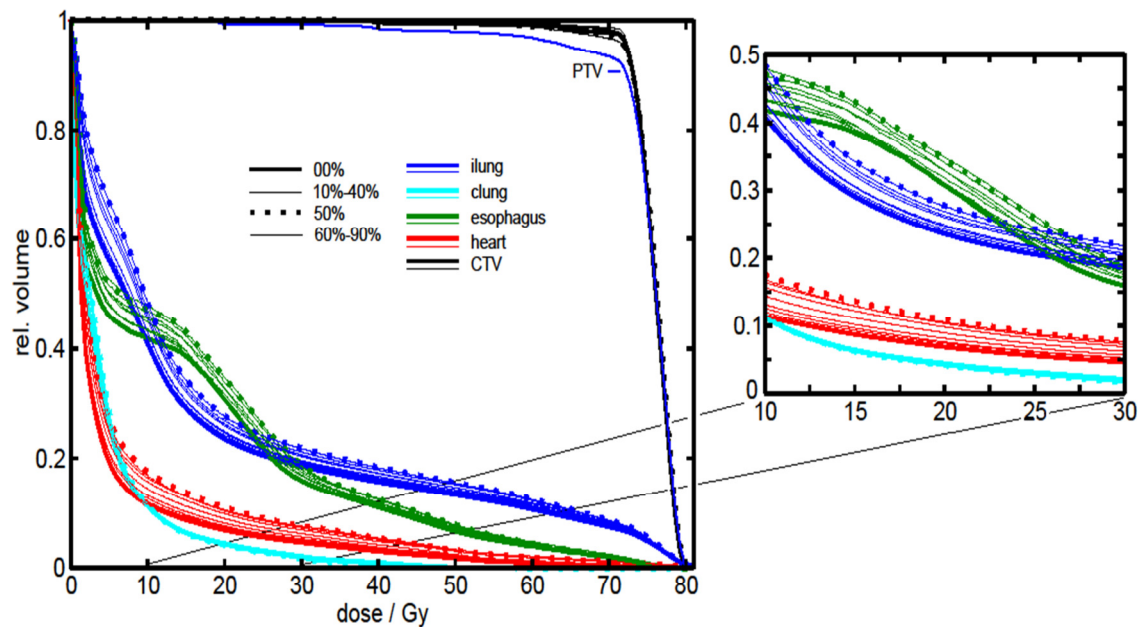
Figure 40. The esophagus MCO plan reduces ipsilateral lung (ilung) dose at the cost of increased dose to esophagus. Evaluation of the plan on 4DCT contours shows dose to the moving target is higher than the PTV dose.

This 4D evaluation of each plan can be accomplished in real time for any basis plan or linear combination of basis plans using the plan interpolator, with the user interface shown in Figure 41. While the 4D-analysis presented in this section can be applied to any plan, MCO has the advantage of enabling plan browsing in real-time without necessitating numerical re-optimization. By adjusting plan weights and interpolating, real-time plan browsing is possible and using the static dose-cloud approximation, the effects of delivering the plan to 4D-anatomy can be assessed.
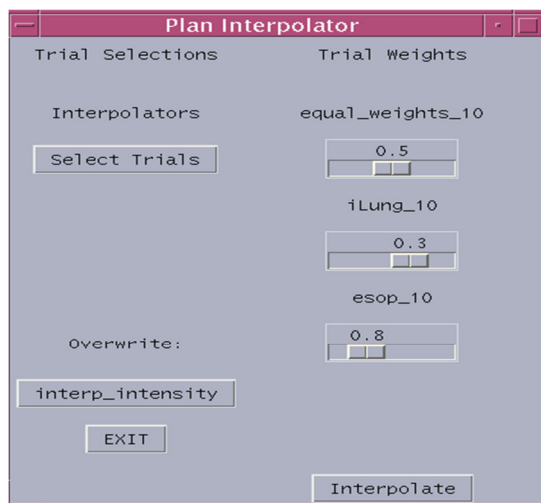
Figure 41. The plan interpolator user interface allows selection of basis plans and allows weight variation on each.

7.4.2 Summary: Plan Robustness on 4D-Anatomy

By estimating dose on time-dependent structures as depicted in 4DCT, an estimate of plan-robustness on 4D-anatomy for a given plan is possible. Based on the case presented, the static-dose cloud approximation is a reasonable assumption for this 4D-evaluation. MCO presents decision opportunities based on OAR dosimetry. Combining MCO real-time planning with 4D-

evaluation allows the physician to make decisions with knowledge of patient-specific decision variables and the effects of delivering each plan to time-dependent anatomy.

7.5 CONCLUSIONS

By decomposing the lung cancer RT problem into hard constraints, soft constraints, and dose-volume objectives, decision opportunities can be clarified for each patient. The method introduced herein constrains the dose to the target and to the spinal cord; however, in other tumor sites other constraints are needed. By grouping together the maximum-dose objectives as soft-constraints in the MCO method presented, the possible trade-offs which exist among them are ignored. Without considering possible tradeoffs in maximum dose the entire relevant region of the Pareto-efficient front may not be exposed to the physician.

By varying the set of objectives, varying dose-volume levels were exposed. The results of section 7.3 imply that the use of different objectives for different OARs may be appropriate based on factors including volumes and anticipated dose-volumes. For organs with low-dose, an objective with a zero-valued dose-prescription uncovers minimal dose-volume levels compared to other plans. This was not the case for ilung, which overlaps the target. For this higher-dose structure, *gEUD* and V10 objectives were superior to other objectives considered in terms of uncovering minima in OAR dose. Selection of the relevant portion of the Pareto frontier, and only the relevant portion, will generate a simplified decision environment in which MCO holds great potential. Further studies are needed to ensure the DVOs used to optimize basis sets truly reveal the extent of decision space.

The basis set, if it is truly on the Pareto-efficient front, should be independent of the dose-volume objectives chosen. This is a desirable feature of the MCO method but also represents an acute deviation from current methods, where outcome studies consider reasonable safe levels of radiation and prescriptions are set at non-zero dose and/or volume levels. This study shows optimizing an objective with a non-zero dose or volume prescription does not imply that the dose-volume level is minimized, using MCO reduced dose at prescription levels compared to plans optimized at those levels.

Rather than consider accumulated dose (or 4DD) and uncertainties which influence 4DD (e.g. phase-weight variations) in plan optimization, this study also shows variability in evaluation metrics can be used to determine plan robustness. MCO offers advantages in this a-posteriori analysis because the collection of MCO plans enables real-time plan design, so that if unacceptable variations are observed in the planning stage, the plan can be redesigned without necessitating numerical re-optimization.

Clinical implementation of MCO, and in particular MCO methods which minimize dose to OARs, shows potential to increase the therapeutic ratio compared to conventional, fixed-objective optimization. Unlike other methods which enable real-time planning, however, MCO also uncovers decision variables for individual patients and enables an assessment of plausible plans for each patient. The current clinical RT planning paradigm, i.e. the planning loop, explores patient-specific tradeoffs in a trial and error process. MCO can clarify these tradeoffs while simultaneously improving the therapeutic ratio.

8   Conclusions

The objective of this work was to implement and develop techniques which, when implemented, will improve the therapeutic ratio of radiation therapy in time-dependent (4D) anatomy. Four-dimensional RT is an active area of research in radiation oncology because it applies to nearly all treatments which utilize fractionated delivery. The methods herein focus on lung cancer for several reasons including the availability of 4D-data. However, many of the methods introduced and investigated also apply to all tumor sites which display time-dependent features.

8.1   IMPROVING DOSE ESTIMATION AND PLAN OPTIMIZATION

Among the most fundamental preconditions of modern radiation therapy is a dose estimator. In this work, a dose estimator utilizing Demons-based DIR and interpolation is compared to single-image, 3D-dose estimation. The results suggest accumulated dose is comparable to 3D-dose in lung cancer organs at risk (OARs) including lungs, heart, and esophagus; however, high dose regions within the PTV can cause large deviations in dose to the moving tumor. Hotspots in the PTV may result in significant dose deviations (>3% of prescription) in the moving target. Specific to respiratory motion, this study also developed a respiratory sampling system to simulate fractionated delivery to 4D-anatomy. The effects of finite delivery time showed

minimal effect on the accumulated dose. In the future, the effects of per-aperture interplay with respiration-induced lung tumor motion can be modeled prospectively using the RPM interface developed as part of this dissertation.

The results of this dissertation suggest large motion is not a pre-requisite to create large deviations between planned dose to the target surrogate (i.e. the 3D-PTV) and delivered dose to a 4D-target; however, these deviations rarely compromise the intent of treatment (i.e. under-dosing moving targets in the PTV is possible, but not probable). Estimated differences between 3DD and 4DD for OARs are generally less than ±3% independent of planning image used to compute dose. This implies that 4D- imaging and planning may only be relevant in the high-dose region, i.e. surrounding the PTV. Reducing the volume for which 4DD is necessary presents advantages in terms of computational efficiency, and more importantly, in terms of sparing healthy tissue from unnecessary radiation during image acquisition. The comparisons of 3DD and 4DD suggest 4DCT for large regions of the thorax is not necessary. With an estimate of the tumor location, e.g. on a 3DCT image or through automated detection through e.g. positron emission tomography, only the tumor region needs to be imaged and considered in a 4D-model for lung cancer RT.

If the motion pattern of the tumor can be estimated, this dissertation shows MAO can directly account for motion in plan design. By relaxing the uniformity (or minimum dose) objective on the ITV and incorporating the tumor-PDF in plan design, the therapeutic ratio can be enhanced. More importantly, MAO can be clinically implemented immediately without introducing new hardware or relying on methods which may cause patient discomfort. Two scenarios which show potential advantages in utilizing MAO, rather than ITV-planning, are (1) a time-dependent

relationship between target and OAR can be exploited through preferentially treating in phases which avoid the OAR, and (2) if a tumor PDF deviates from a uniform distribution, MAO identifies regions of the PTV where the target dose can be adjusted to match the tumor-PDF.

Further studies of per-aperture interplay effects are needed in order to ensure treatment intent is not compromised when delivering an MAO plan clinically. While the effects of finite delivery time and interplay between patient-specific breathing and non-uniform delivery are not alarming (<1.5 Gy variation in target D_{95} in all estimates), the effects of per-aperture interplay must also be considered in a clinically realizable plan. This is a focus of future work in order to ensure MAO can be safely implemented clinically.

8.2 STRUCTURE MASS IN RADIATION THERAPY

Another pre-requisite of RT is meaningful and precise evaluation metrics. Dose-volume metrics may not be consistent with current prospective models of radiation damage (i.e. the LQ model) in heterogeneous tissues. This is relevant in lung cancer, where volume-based metrics in heterogeneous tissues in lung and PTV treat all voxels equally in plan optimization and outcome analysis. In fact, a voxel of air within the lung or PTV surely does not include as many functional cells as voxels of solid tumors or lung-tissues. An analogous comparison can be made in OARs in the pelvis including rectum and bladder. By including non-functional matter in these organs, rather than the organs walls, an inconsistency is created between the evaluation of dose and radiation damage due to dose. Dose-to-mass is an intuitive measure, it is the total energy absorbed in tissue.

Using dose-to-mass to guide optimization is a method which assigns per-voxel weightings according to voxel density measured in 4DCT simulation. The basic premise of DMH-based optimization is functional density is proportional to physical density. This implies that the DMH, which plots relative density at dose, is equal to a dose-to-functional-tissue histogram. This assumption may be valid in the PTV, where tumor clonogen density is likely proportional to physical density. In lung, however, low density parenchyma may be significant to oxygen-exchange, whereas high density blood and blood vessels are not directly related to functionality, i.e. dose to mass is not related to dose to functional tissue in lung. If a functional signal can be acquired, for any ROI, it can be incorporated in a voxel-weighted optimization. Because dose-to-mass penalizes treatment of massive regions of normal tissues, DMH optimization has the potential to reduce integral dose to normal tissues.

Using dose-to-mass to evaluate dose distributions in tissue is a more precise evaluation than dose-to-volume metrics on 4DCT image sets. While volume of lung and tumors physically varies during respiration, mass is constant. Evaluation of delineated structure mass as defined on 4DCT image sets allows for an estimate of delineation consistency. In many of the cases considered, structures defined using DIR result in less inter-phase mass variation compared to physician contours; however, DIR failed to conserve mass in GTV and lung to within 5% in the presence of image artifacts.

8.3 RADIATION THERAPY DECISION MAKING

In general, a set of achievable objectives are defined by the constraints of the problem at hand. In RT of lung cancer, this is the patient-specific anatomy and a constrained, prescription dose to

the target. These two factors determine the relevant portion of the Pareto-efficient front, where RT decision making can take place in order to design an optimal treatment plan. By further reducing the set of objectives into a set of soft constraints, which are not intended to be traded-off or compromised, this work shows that a tractable decision space can be revealed based on as few as two plans, trading off as few as two OARs. Risk of complication and impact on quality of life do not have a one-to-one correspondence for many individual patients. This implies that risk of complication should be considered on a per-patient basis, including relevant factors like age and prior health issues. Patient-specific OAR-weightings can be considered in the context of a realizable decision space and MCO can uncover this decision space.

8.4 SUMMARY

The goal of this dissertation was to implement and develop techniques which, when implemented, have the potential to improve RT for time-dependent anatomy and specifically to improve the therapeutic ratio for time-dependent anatomy. This study shows implementation of MCO for lung cancer planning will expose opportunities to increase the therapeutic ratio. Estimating dose to time dependent anatomy, either through dose-accumulation or through evaluation on multiple images, will allow for a more precise evaluation of dose during planning and treatment. By explicitly considering anatomic motion in plan design, MAO can enhance the therapeutic ratio for lung cancer patients by optimizing accumulated dose. Finally, using dose-to-mass to evaluate radiation therapy will allow for more precise metrics which may be related to outcomes and RT efficacy. Dose-to-mass is closely related to the currently used prospective

model of radiation damage, the LQ model, evaluation of dose-to-mass in lung cancer outcome

studies may allow for precise modeling of cell-kill in tumors.

References

LIST OF REFERENCES

1   SEER Stat Fact Sheets: Lung and Bronchus,
    http://seer.cancer.gov/statfacts/html/lungb.html (03/11/2013).

2   D. A. Low, M. Nystrom, E. Kalinin, P. Parikh, J. F. Dempsey, J. D. Bradley, et al., "A method
    for the reconstruction of four-dimensional synchronized CT scans acquired during free
    breathing," Medical Physics **30**, 1254 (2003).

3   P. J. Keall, G. Starkschall, H. Shukla, K. M. Forster, V. Ortiz, C. W. Stevens, et al., "Acquiring
    4D thoracic CT scans using a multislice helical method," Physics in Medicine and Biology **49**,
    2053–2067 (2004).

4   R. George, S. S. Vedam, T. D. Chung, V. Ramakrishnan, and P. J. Keall, "The application of the
    sinusoidal model to lung cancer patient respiratory motion," Medical Physics **32**, 2850–
    2861 (2005).

5   Y. Suh, S. Dieterich, B. Cho, and P. J. Keall, "An analysis of thoracic and abdominal tumour
    motion for stereotactic body radiotherapy patients," Physics in Medicine and Biology **53**,
    3623–3640 (2008).

6   T. Yamamoto, U. Langner, B. W. Loo Jr., J. Shen, and P. J. Keall, "Retrospective Analysis of
    Artifacts in Four-Dimensional CT Images of 50 Abdominal and Thoracic Radiotherapy
    Patients," International Journal of Radiation Oncology Biology Physics **72**, 1250–1258
    (2008).

7   W. T. Watkins, R. Li, J. Lewis, J. C. Park, A. Sandhu, S. B. Jiang, et al., "Patient-specific motion
    artifacts in 4DCT," Medical Physics **37**, 2855–2861 (2010).

8   W. Lu, P. J. Parikh, I. M. El Naqa, M. M. Nystrom, J. P. Hubenschmidt, S. H. Wahab, et al.,
    "Quantitation of the reconstruction quality of a four-dimensional computed tomography
    process for lung cancer patients," Medical Physics **32**, 890–901 (2005).

9   R. Werner, B. White, H. Handels, W. Lu, and D. A. Low, "Technical Note: Development of a tidal volume surrogate that replaces spirometry for physiological breathing monitoring in 4D CT," Medical Physics **37**, 615–619 (2010).

10   R. Li, J. H. Lewis, L. I. Cerviño, and S. B. Jiang, "4D CT sorting based on patient internal anatomy," Physics in Medicine and Biology **54**, 4821–4833 (2009).

11   C. K. Glide-Hurst, G. D. Hugo, J. Liang, and D. Yan, "A simplified method of four-dimensional dose accumulation using the mean patient density representation," Medical Physics **35**, 5269–5277 (2008).

12   R. W. M. Underberg, F. J. Lagerwaard, B. J. Slotman, J. P. Cuijpers, and S. Senan, "Use of maximum intensity projections (MIP) for target volume generation in 4DCT scans for lung cancer," International Journal of Radiation Oncology Biology Physics **63**, 253–260 (2005).

13   K. Park, L. Huang, H. Gagne, and L. Papiez, "Do maximum intensity projection images truly capture tumor motion?," International Journal of Radiation Oncology Biology Physics **73**, 618–625 (2009).

14   P. J. Keall, G. S. Mageras, J. M. Balter, R. S. Emery, K. M. Forster, S. B. Jiang, et al., "The management of respiratory motion in radiation oncology report of AAPM Task Group 76," Medical Physics **33**, 3874 (2006).

15   International Commission on Radiation Units and Measurements (ICRU) Report 62: Prescribing, recording, and reporting photon beam therapy. (International Commission on Radiation Units and Measurements, Bethesda, MD, 1999).

16   A. M. Allen, K. M. Siracuse, J. A. Hayman, and J. M. Balter, "Evaluation of the influence of breathing on the movement and modeling of lung tumors," International Journal of Radiation Oncology Biology Physics **58**, 1251–1257 (2004).

17   E. Rietzel, A. K. Liu, K. P. Doppke, J. A. Wolfgang, A. B. Chen, G. T. Y. Chen, et al., "Design of 4D treatment planning target volumes," International Journal of Radiation Oncology Biology Physics **66**, 287–295 (2006).

18   K. Ohara, T. Okumura, M. Akisada, T. Inada, T. Mori, H. Yokota, M.J.B. Calaguas, "Irradiation synchronized with respiration gate," International Journal of Radiation Oncology Biology Physics **17**, 853–857 (1989).

19   P. J. Keall, V. R. Kini, S. S. Vedam, and R. Mohan, "Potential radiotherapy improvements with respiratory gating," Australasian Physical & Engineering Sciences in Medicine **25**, 1–6 (2002).

20   S. B. Jiang, "Technical aspects of image-guided respiration-gated radiation therapy," Medical Dosimetry **31**, 141–151 (2006).

21   J. Hanley, M. M. Debois, D. Mah, G. S. Mageras, A. Raben, K. Rosenzweig, et al., "Deep inspiration breath-hold technique for lung tumors: the potential value of target immobilization and reduced lung density in dose escalation," International Journal of Radiation Oncology Biology Physics **45**, 603–611 (1999).

22   J. W. Wong, M. B. Sharpe, D. A. Jaffray, V. R. Kini, J. M. Robertson, J. S. Stromberg, et al., "The use of active breathing control (ABC) to reduce margin for breathing motion," International Journal of Radiation Oncology Biology Physics **44**, 911–919 (1999).

23   C. K. Glide-Hurst, E. Gopan, and G. D. Hugo, "Anatomic and Pathologic Variability During Radiotherapy for a Hybrid Active Breath-Hold Gating Technique," International Journal of Radiation Oncology Biology Physics **77**, 910–917 (2010).

24   S. P. Robertson, E. Weiss, and G. D. Hugo, "Localization accuracy from automatic and semi-automatic rigid registration of locally-advanced lung cancer targets during image-guided radiation therapy," Medical Physics **39**, 330–341 (2012).

25   L. Papież, "The leaf sweep algorithm for an immobile and moving target as an optimal control problem in radiotherapy delivery," Mathematical and Computer Modelling **37**, 735–745 (2003).

26   L. Papież, "DMLC leaf-pair optimal control of IMRT delivery for a moving rigid target," Medical Physics **31**, 2742–2754 (2004).

27   S. Webb, "The effect on IMRT conformality of elastic tissue movement and a practical suggestion for movement compensation via the modified dynamic multileaf collimator (dMLC) technique," Physics in Medicine and Biology **50**, 1163–1190 (2005).

28   M. Isaksson, J. Jalden, and M. J. Murphy, "On using an adaptive neural network to predict lung tumor motion during respiration for radiotherapy applications," Medical Physics **32**, 3801 (2005).

29   D. Ruan, "Kernel density estimation-based real-time prediction for respiratory motion," Physics in Medicine and Biology **55**, 1311–1326 (2010).

30   T. Neicu, R. Berbeco, J. Wolfgang, and S. B. Jiang, "Synchronized moving aperture radiation therapy (SMART): improvement of breathing pattern reproducibility using respiratory coaching," Physics Medicine Biology **51**, 617–636 (2006).

31   A. Trofimov, E. Rietzel, H.-M. Lu, B. Martin, S. Jiang, G. T. Y. Chen, et al., "Temporo-spatial IMRT optimization: concepts, implementation and initial results," Physics in Medicine and Biology **50**, 2779–2798 (2005).

32   A. Sawant, R. Venkat, V. Srivastava, D. Carlson, S. Povzner, H. Cattell, et al., "Management of three-dimensional intrafraction motion through real-time DMLC tracking," Medical Physics **35**, 2050 (2008).

33   Y. Suh, A. Sawant, R. Venkat, and P. J. Keall, "Four-dimensional IMRT treatment planning using a DMLC motion-tracking algorithm," Physics in Medicine and Biology **54**, 3821–3835 (2009).

34   E. J. Hall and A. Giaccia, *Radiobiology for the Radiologist,* 7th Edition. (Lippincott Williams and Wikins, 2012)

35   J. F. Fowler, "The linear-quadratic formula and progress in fractionated radiotherapy," British Journal of Radiology **62**, 679–694 (1989).

36 G. W. Barendsen, "Dose fractionation, dose rate and iso-effect relationships for normal tissue responses," International Journal of Radiation Oncology Biology Physics **8**, 1981–1997 (1982).

37 Radiation Therapy Oncology Group (RTOG) 0915 Protocol Information, http://www.rtog.org/ClinicalTrials/ProtocolTable/StudyDetails.aspx?study=0915 (2012).

38 J. Bradley, M. V. Graham, K. Winter, J. A. Purdy, R. Komaki, W. H. Roa, J.K. Ryu, W. Bosch, B. Emami, "Toxicity and outcome results of RTOG 9311: a phase I-II dose-escalation study using three-dimensional conformal radiotherapy in patients with inoperable non-small-cell lung carcinoma," International Journal of Radiation Oncology Biology Physics **61**, 318–328 (2005).

39 J. Bradley, "A review of radiation dose escalation trials for non-small cell lung cancer within the Radiation Therapy Oncology Group," Seminars in Oncology **32**, S111–113 (2005).

40 R. Hara, J. Itami, T. Kondo, T. Aruga, Y. Abe, M. Ito, M. Fuse, D. Shinohara, T. Nagaoka, T. Kobiki, "Stereotactic single high dose irradiation of lung tumors under respiratory gating," Radiotherapy Oncology **63**, 159–163 (2002).

41 J. P. Kirkpatrick, J. J. Meyer, and L. B. Marks, "The linear-quadratic model is inappropriate to model high dose per fraction effects in radiosurgery," Seminars in Radiation Oncology **18**, 240–243 (2008).

42 W. U. Shipley, J. E. Tepper, G. R. Prout Jr, L. J. Verhey, O. A. Mendiondo, M. Goitein, A.M. Koehler, H.D. Suit, "Proton radiation as boost therapy for localized prostatic carcinoma," JAMA: The Journal of the American Medical Association **241**, 1912–1915 (1979).

43 P. Källman, A. Agren, and A. Brahme, "Tumour and normal tissue responses to fractionated non-uniform dose delivery," International Journal of Radiation Oncology Biology Physics **62**, 249–262 (1992).

44 J. T. Lyman, "Complication Probability as Assessed from Dose-Volume Histograms," Radiation Research **104**, S13–S19 (1985).

45   A. Niemierko, "A generalized concept of equivalent uniform dose (EUD)," Medical Physics **26**, (1999).

46   L. B. Marks, R. K. Ten Haken, and M. K. Martel, "Guest Editor's Introduction to QUANTEC: A Users Guide," International Journal of Radiation Oncology Biology Physics **76**, S1–S2 (2010).

47   B. Emami, J. Lyman, A. Brown, L. Coia, M. Goitein, J. E. Munzenrider, B. Shank, L.J. Solin, M. Wesson, "Tolerance of normal tissue to therapeutic irradiation," International Journal of Radiation Oncology Biology Physics **21**, 109–122 (1991).

48   J. P. Kirkpatrick, A. J. van der Kogel, and T. E. Schultheiss, "Radiation Dose–Volume Effects in the Spinal Cord," International Journal of Radiation Oncology Biology Physics **76**, S42–S49 (2010).

49   M. Werner-Wasik, E. Yorke, J. Deasy, J. Nam, and L. B. Marks, "Radiation Dose-Volume Effects in the Esophagus," International Journal of Radiation Oncology Biology Physics **76**, S86–S93 (2010).

50   G. Gagliardi, L. S. Constine, V. Moiseenko, C. Correa, L. J. Pierce, A. M. Allen, L.B. Marks, "Radiation Dose–Volume Effects in the Heart," International Journal of Radiation Oncology Biology Physics **76**, S77–S85 (2010).

51   L. B. Marks, S. M. Bentzen, J. O. Deasy, F.-M. (Spring) Kong, J. D. Bradley, I. S. Vogelius, et al., "Radiation Dose–Volume Effects in the Lung," International Journal of Radiation Oncology Biology Physics **76**, S70–S76 (2010).

52   K. S. C. Chao, S. A. M.D, and G. O. M.D, *Practical Essentials of Intensity Modulated Radiation Therapy,* 2ⁿᵈ Edition. (Lippincott Williams & Wilkins, 2005).

53   T. A. Hazra, M. S. Chandrasekaran, M. Colman, T. Prempree, and A. Inalsingh, "Survival in carcinoma of the lung after a split course of radiotherapy," British Journal of Radiology **47**, 464–466 (1974).

54   N. C. Choi, H. C. Grillo, M. Gardiello, J. G. Scannell, and E. W. Wilkins Jr, "Basis for new strategies in postoperative radiotherapy of bronchogenic carcinoma," International Journal of Radiation Oncology Biology Physics **6**, 31–35 (1980).

55   H. Scruggs, A. El-Mahdi, R. D. Marks, and W. C. Constable, "The results of split-course radiation therapy in cancer of the lung," American Journal of Roentgenology, Radium Therapy, and Nuclear Medicine **121**, 754–760 (1974).

56   A. Ozgen, M. Hayran, and F. Kahraman, "Mean esophageal radiation dose is predictive of the grade of acute esophagitis in lung cancer patients treated with concurrent radiotherapy and chemotherapy," Journal of Radiation Research **53**, 916–922 (2012).

57   S. Krafft, S. Tucker, Z. Liao, L. Court, D. Gomez, and M. Martel, "Mean Regional Dose to the Esophagus Predicts Acute Toxicity Rate for Lung Cancer Patients," Medical Physics **39**, 3856–3856 (2012).

58   A. K. Singh, M. A. Lockett, and J. D. Bradley, "Predictors of radiation-induced esophageal toxicity in patients with non-small-cell lung cancer treated with three-dimensional conformal radiotherapy," International Journal of Radiation Oncology Biology Physics **55**, 337–341 (2003).

59   W.-B. Qiao, Y.-H. Zhao, Y.-B. Zhao, and R.-Z. Wang, "Clinical and dosimetric factors of radiation-induced esophageal injury: radiation-induced esophageal toxicity," World Journal of Gastroenterology **11**, 2626–2629 (2005).

60   J. Belderbos, W. Heemsbergen, M. Hoogeman, K. Pengel, M. Rossi, and J. Lebesque, "Acute esophageal toxicity in non-small cell lung cancer patients after high dose conformal radiotherapy," Radiotherapy Oncology **75**, 157–164 (2005).

61   X. Wei, H. H. Liu, S. L. Tucker, S. Wang, R. Mohan, J. D. Cox, R. Komaki, Z. Liao, "Risk Factors for Pericardial Effusion in Inoperable Esophageal Cancer Patients Treated With Definitive Chemoradiation Therapy," International Journal of Radiation Oncology Biology Physics **70**, 707-714 (2008).

62 E. M. T. Dieleman, S. Senan, A. Vincent, F. J. Lagerwaard, B. J. Slotman, and J. R. van Sörnsen de Koste, "Four-dimensional computed tomographic analysis of esophageal mobility during normal respiration," International Journal of Radiation Oncology Biology Physics **67**, 775–780 (2007).

63 E. Nioutsikou, S. Webb, N. Panakis, T. Bortfeld, and U. Oelfke, "Reconsidering the definition of a dose--volume histogram," Physics in Medicine and Biology **50**, L17–L19 (2005).

64 M. van Herk, "Errors and margins in radiotherapy," Seminars in Radiation Oncology **14**, 52–64 (2004).

65 J. C. Stroom, H. C. de Boer, H. Huizenga, and A. G. Visser, "Inclusion of geometrical uncertainties in radiotherapy treatment planning by means of coverage probability," International Journal of Radiation Oncology Biology Physics **43**, 905–919 (1999).

66 A. V. Louie, G. Rodrigues, J. Olsthoorn, D. Palma, E. Yu, B. Yaremko, B. Ahmad, I. Aivas, "Inter-observer and intra-observer reliability for lung cancer target volume delineation in the 4D-CT era," Radiotherapy and Oncology **95**, 166–171 (2010).

67 J. A. Moore, J. J. Gordon, M. S. Anscher, and J. V. Siebers, "Comparisons of treatment optimization directly incorporating random patient setup uncertainty with a margin-based approach," Medical Physics **36**, 3880–3890 (2009).

68 I. S. Grills, G. Hugo, L. L. Kestin, A. P. Galerani, K. K. Chao, J. Wloch, D. Yan, "Image-guided radiotherapy via daily online cone-beam CT substantially reduces margin requirements for stereotactic lung radiotherapy," International Journal of Radiation Oncology Biology Physics **70**, 1045–1056 (2008).

69 A. R. Yeung, J. G. Li, W. Shi, H. E. Newlin, A. Chvetsov, C. Liu, J. R. Palta, K. Olivier, "Tumor localization using cone-beam CT reduces setup margins in conventionally fractionated radiotherapy for lung tumors," International Journal of Radiation Oncology Biology Physics **74**, 1100–1107 (2009).

[70] T. G. Purdie, J.-P. Bissonnette, K. Franks, A. Bezjak, D. Payne, F. Sie, M. B. Sharpe, D. A. Jaffray, "Cone-Beam Computed Tomography for On-Line Image Guidance of Lung Stereotactic Radiotherapy: Localization, Verification, and Intrafraction Tumor Position," International Journal of Radiation Oncology Biology Physics **68**, 243–252 (2007).

[71] J.-P. Bissonnette, T. G. Purdie, J. A. Higgins, W. Li, and A. Bezjak, "Cone-Beam Computed Tomographic Image Guidance for Lung Cancer Radiation Therapy," International Journal of Radiation Oncology Biology Physics **73**, 927–934 (2009).

[72] Alpha Cradle, http://www.alphacradle.com/ (03/14/13).

[73] D. Yan, D. Lockman, A. Martinez, J. Wong, D. Brabbins, F. Vicini, et al., "Computed tomography guided management of interfractional patient variation," Seminars in Radiation Oncology **15**, 168–179 (2005).

[74] J. C. Stroom and B. J. M. Heijmen, "Geometrical uncertainties, radiotherapy planning margins, and the ICRU-62 report," Radiotherapy and Oncology **64**, 75–83 (2002).

[75] J. J. Gordon and J. V. Siebers, "Coverage-based treatment planning: Optimizing the IMRT PTV to meet a CTV coverage criterion," Medical Physics **36**, 961–973 (2009).

[76] J. J. Gordon, N. Sayah, E. Weiss, and J. V. Siebers, "Coverage optimized planning: Probabilistic treatment planning based on dose coverage histogram criteria," Medical Physics **37**, 550–563 (2010).

[77] Q. Wu and R. Mohan, "Multiple local minima in IMRT optimization based on dose–volume criteria," Medical Physics **29**, 1514 (2002).

[78] J. Löf, Development of a general framework for optimization of radiation therapy, Ph.D. Thesis, Stockholm University (2000).

[79] J. Nocedal and S. J. Wright, *Numerical Optimization,* (Springer, 1999).

80   J. Lof, B. K. Lind, and A. Brahme, "Optimal radiation beam profiles considering the stochastic process of patient positioning in fractionated radiation therapy," Inverse Problems **11**, 1189–1209 (1995).

81   V. Pareto, *Cours d'economie politique,* (F. Rouge, 1896).

82   V. Pareto, Manual of Political Economy, (Macmillan Co., 1927).

83   H. E. Romeijn, J. F. Dempsey, and J. G. Li, "A unifying framework for multi-criteria fluence map optimization models," Physics in Medicine and Biology **49**, 1991 (2004).

84   G. D. Hugo, D. Yan, and J. Liang, "Population and patient-specific target margins for 4D adaptive radiotherapy to account for intra- and inter-fraction variation in lung tumour position," Physics in Medicine and Biology **52**, 257 (2007).

85   M. A. Admiraal, D. Schuring, and C. W. Hurkmans, "Dose calculations accounting for breathing motion in stereotactic lung radiotherapy based on 4D-CT and the internal target volume," Radiotherapy Oncology **86**, 55–60 (2008).

86   K. K. Brock, D. L. McShan, R. K. Ten Haken, S. J. Hollister, L. A. Dawson, and J. M. Balter, "Inclusion of organ deformation in dose calculations," Medical Physics **30**, 290 (2003).

87   M. Rosu, I. J. Chetty, J. M. Balter, M. L. Kessler, D. L. McShan, and R. K. Ten Haken, "Dose reconstruction in deforming lung anatomy: Dose grid size effects and clinical implications," Medical Physics **32**, 2487 (2005).

88   T. Guerrero, G. Zhang, W. Segars, T.-C. Huang, S. Bilton, G. Ibbott, et al., "Elastic Image Mapping for 4-D Dose Estimation in Thoracic Radiotherapy," Radiation Protection Dosimetry **115**, 497–502 (2005).

89   S. Flampouri, S. B. Jiang, G. C. Sharp, J. Wolfgang, A. A. Patel, and N. C. Choi, "Estimation of the delivered patient dose in lung IMRT treatment based on deformable registration of 4D-

CT data and Monte Carlo simulations," Physics in Medicine and Biology **51**, 2763–2779 (2006).

90   M. Guckenberger, J. Wilbert, T. Krieger, A. Richter, K. Baier, J. Meyer, et al., "Four-dimensional treatment planning for stereotactic body radiotherapy," International Journal of Radiation Oncology Biology Physics **69**, 276–285 (2007).

91   M. Rosu, J. M. Balter, I. J. Chetty, M. L. Kessler, D. L. McShan, P. Balter, et al., "How extensive of a 4D dataset is needed to estimate cumulative dose distribution plan evaluation metrics in conformal lung therapy?," Medical Physics **34**, 233 (2007).

92   E. Heath, J. Seco, Z. Wu, G. C. Sharp, H. Paganetti, and J. Seuntjens, "A comparison of dose warping methods for 4D Monte Carlo dose calculations in lung," Journal of Physics: Conference Series **102**, 012013 (2008).

93   G. Starkschall, K. Britton, M. F. McAleer, M. D. Jeter, M. R. Kaus, K. Bzdusek, et al., "Potential Dosimetric Benefits of Four-Dimensional Radiation Treatment Planning," International Journal of Radiation Oncology Biology Physics **73**, 1560–1565 (2009).

94   Y. Y. Vinogradskiy, P. Balter, D. S. Followill, P. E. Alvarez, R. A. White, and G. Starkschall, "Verification of four-dimensional photon dose calculations," Medical Physics **36**, 3438–3447 (2009).

95   R. I. Berbeco, C. J. Pope, and S. B. Jiang, "Measurement of the interplay effect in lung IMRT treatment using EDR2 films," Journal of Applied Clinical Medical Physics **7**, (2006).

96   S. R. Chaudhari, S. M. Goddu, D. Rangaraj, O. L. Pechenaya, W. Lu, E. Kintzel, et al., "Dosimetric variances anticipated from breathing- induced tumor motion during tomotherapy treatment delivery.," Physics in Medicine and Biology **54**, 2541–2555 (2009).

97   J.-P. Thirion, "Image matching as a diffusion process: an analogy with Maxwell's demons," Medical Image Analysis **2**, 243–260 (1998).

98   The Insight Segmentation and Registration Toolkit (ITK), www.itk.org.

99   T. Vercauteren, X. Pennec, A. Perchant, and N. Ayache, "Diffeomorphic demons: efficient non-parametric image registration," Neuroimage **45**, S61–72 (2009).

100   Florence Dru and Tom Vercauteren, "An ITK Implementation of the Symmetric Log-Domain Diffeomorphic Demons Algorithm," Insight Journal (in press), 1–10 (2009).

101   J. V. Siebers and H. Zhong, "An energy transfer method for 4D Monte Carlo dose calculation," Medical Physics **35**, 4096–4105 (2008).

102   E. Heath, F. Tessier, and I. Kawrakow, "Investigation of voxel warping and energy mapping approaches for fast 4D Monte Carlo dose calculations in deformed geometries using VMC++," Physics in Medicine and Biology **56**, 5187–5202 (2011).

103   C. Yan, G. Hugo, F. J. Salguero, N. Saleh-Sayah, E. Weiss, W. C. Sleeman, et al., "A method to evaluate dose errors introduced by dose mapping processes for mass conserving deformations," Medical Physics **39**, 2119–2128 (2012).

104   S. B. Jiang, C. Pope, K. M. A. Jarrah, J. H. Kung, T. Bortfeld, and G. T. Y. Chen, "An experimental investigation on intra-fractional organ motion effects in lung IMRT treatments," Physics in Medicine and Biology **48**, 1773–1784 (2003).

105   L. Lee, Q.-T. Le, and L. Xing, "Retrospective IMRT Dose Reconstruction Based on Cone-Beam CT and MLC Log-File," International Journal of Radiation Oncology Biology Physics **70**, 634–644 (2008).

106   M.-H. Lin, J. Li, L. Wang, S. Koren, J. Fan, E. Forkal, et al., "4D patient dose reconstruction using online measured EPID cine images for lung SBRT treatment validation," Medical Physics **39**, 5949–5958 (2012).

107   M. D. Jensen, A. Abdellatif, J. Chen, and E. Wong, "Study of the IMRT interplay effect using a 4DCT Monte Carlo dose calculation," Physics in Medicine and Biology **57**, N89 (2012).

108 H. Li, H. Zhong, J. Kim, T. Nurushev, and I. Chetty, "SU-E-T-874: Investigation of the Interplay Effect Between MLC and Lung Tumor Motions Using 4DCT and RPM Profile Data," Medical Physics **38**, 3692–3693 (2011).

109 T. Bortfeld, K. Jokivarsi, M. Goitein, J. Kung, and S. B. Jiang, "Effects of intra-fraction motion on IMRT dose delivery: statistical analysis and simulation," Physics in Medicine and Biology **47**, 2203–2220 (2002).

110 L. Court, M. Wagar, R. Berbeco, A. Reisner, B. Winey, D. Schofield, et al., "Evaluation of the interplay effect when using RapidArc to treat targets moving in the craniocaudal or right-left direction," Medical Physics **37**, 4–11 (2010).

111 L. E. Court, M. Wagar, D. Ionascu, R. Berbeco, and L. Chin, "Management of the interplay effect when using dynamic MLC sequences to treat moving targets," Medical Physics **35**, 1926–1931 (2008).

112 Varian Medical Systems, http://www.varian.com/us/oncology/radiosurgery/truebeam-stx.html (2013).

113 J. G. Li and L. Xing, "Inverse planning incorporating organ motion," Medical Physics **27**, 1573–1578 (2000).

114 M. Birkner, D. Yan, M. Alber, J. Liang, and F. Nüsslin, "Adapting inverse planning to patient and organ geometrical variation: algorithm and implementation," Medical Physics **30**, 2822–2831 (2003).

115 D. L. McShan, M. L. Kessler, K. Vineberg, and B. A. Fraass, "Inverse plan optimization accounting for random geometric uncertainties with a multiple instance geometry approximation (MIGA)," Medical Physics **33**, 1510–1521 (2006).

116 A. E. Lujan, J. M. Balter, and R. K. Ten Haken, "A method for incorporating organ motion due to breathing into 3D dose calculations in the liver: Sensitivity to variations in motion," Medical Physics **30**, 2643 (2003).

117 P. Zhang, G. D. Hugo, and D. Yan, "Planning Study Comparison of Real-Time Target Tracking and Four-Dimensional Inverse Planning for Managing Patient Respiratory Motion," International Journal of Radiation Oncology Biology Physics **72**, 1221–1227 (2008).

118 M. Söhn, M. Weinmann, and M. Alber, "Intensity-modulated radiotherapy optimization in a quasi-periodically deforming patient model," International Journal of Radiation Oncology Biology Physics **75**, 906–914 (2009).

119 J. Unkelbach and U. Oelfke, "Inclusion of organ movements in IMRT treatment planning via inverse planning based on probability distributions," Physics in Medicine and Biology **49**, 4005–4029 (2004).

120 J. Unkelbach and U. Oelfke, "Incorporating organ movements in inverse planning: assessing dose uncertainties by Bayesian inference," Physics in Medicine and Biology **50**, 121–139 (2005).

121 E. Heath, J. Unkelbach, and U. Oelfke, "Incorporating uncertainties in respiratory motion into 4D treatment plan optimization," Medical Physics **36**, 3059–3071 (2009).

122 A. Fredriksson, A. Forsgren, and B. Hardemark, "Minimax optimization for handling range and setup uncertainties in proton therapy," Medical Physics **38**, 1672–1684 (2011).

123 K. Sheng, J. Cai, J. Brookeman, J. Molloy, J. Christopher, and P. Read, "A computer simulated phantom study of tomotherapy dose optimization based on probability density functions (PDF) and potential errors caused by low reproducibility of PDF," Medical Physics **33**, 3321 (2006).

124 T. C. Y. Chan, T. Bortfeld, and J. N. Tsitsiklis, "A robust approach to IMRT optimization," Physics in Medicine and Biology **51**, 2567–2583 (2006).

125 T. Bortfeld, T. C. Y. Chan, A. Trofimov, and J. N. Tsitsiklis, "Robust Management of Motion Uncertainty in Intensity-Modulated Radiation Therapy," Operations Research **56**, 1461–1473 (2008).

[126] A. Ben-Tal and A. Nemirovski, "Robust Convex Optimization," Mathematics of Operations Research **23**, 769–805 (1998).

[127] O. Nohadani, J. Seco, and T. Bortfeld, "Motion management with phase-adapted 4D-optimization," Physics in Medicine and Biology **55**, 5189–5202 (2010).

[128] J. M. Mulvey, R. J. Vanderbei, and S. A. Zenios, "Robust Optimization of Large-Scale Systems," Operations Research **43**, 264–281 (1995).

[129] O. Nohadani, J. Seco, and T. Bortfeld, "Motion management with phase-adapted 4D-optimization," Physics in Medicine and Biology **55**, 5189–5202 (2010).

[130] H. H. Liu, P. Balter, T. Tutt, B. Choi, J. Zhang, C. Wang, et al., "Assessing respiration-induced tumor motion and internal target volume using four-dimensional computed tomography for radiotherapy of lung cancer," International Journal of Radiation Oncology Biology Physics **68**, 531–540 (2007).

[131] R. P. Brent, *Algorithms for Minimization without Derivatives,* (Prentice-Hal, 1973).

[132] O. Nohadani, J. Seco, B. C. Martin, and T. Bortfeld, "Dosimetry robustness with stochastic optimization," Physics in Medicine and Biology **54**, 3421–3432 (2009).

[133] L. E. Butler, K. M. Forster, C. W. Stevens, C. Bloch, H. H. Liu, S. L. Tucker, et al., "Dosimetric benefits of respiratory gating: a preliminary study," Journal of Applied Clinical Medical Physics **5**, 16–24 (2004).

[134] P. Mavroidis, G. A. Plataniotis, M. A. Górka, and B. K. Lind, "Comments on 'Reconsidering the definition of a dose–volume histogram'—dose–mass histogram (DMH) versus dose–volume histogram (DVH) for predicting radiation-induced pneumonitis," Physics in Medicine and Biology **51**, L43–L50 (2006).

[135] B. Li, G. E. Christensen, E. A. Hoffman, G. McLennan, and J. M. Reinhardt, "Pulmonary CT image registration and warping for tracking tissue deformation during the respiratory cycle through 3D consistent image registration," Medical Physics **35**, 5575–5583 (2008).

[136] L. Fan, C. W. Chen, C. -T. Chen, A. V. Clough "3D warping and registration from lung images," SPIE Proceedings **3660,** 459–470 (1999).

[137] V. Boldea, D. Sarrut, and et al, "Lung Deformation Estimation with Non-rigid Registration for Radiotherapy Treatment," *Medical Image Computing and Computer Assisted Intervention Lecture Notes in Computer Science*, (Springer-Verlag GmbH, 2003), 770–777.

[138] Y. Yin, E. A. Hoffman, and C.-L. Lin, "Mass preserving nonrigid registration of CT lung images using cubic B-spline," Medical Physics **36**, 4213–4222 (2009).

[139] M. Ugander, E. Jense, and H. Arheden, "Pulmonary intravascular blood volume changes through the cardiac cycle in healthy volunteers studied by cardiovascular magnetic resonance measurements of arterial and venous flow," Journal of Cardiovascular Magnetic Resonance **11**, 42 (2009).

[140] C. A. Perez, K. Stanley, P. Rubin, S. Kramer, L. Brady, R. Perez-Tamayo, et al., "A prospective randomized study of various irradiation doses and fractionation schedules in the treatment of inoperable non-oat-cell carcinoma of the lung. Preliminary report by the radiation therapy oncology group," Cancer **45**, 2744–2753 (1980).

[141] P. A. Kupelian, C. Ramsey, S. L. Meeks, T. R. Willoughby, A. Forbes, T. H. Wagner, et al., "Serial megavoltage CT imaging during external beam radiotherapy for non–small-cell lung cancer: Observations on tumor regression during treatment," International Journal of Radiation Oncology Biology Physics **63**, 1024–1028 (2005).

[142] I. I. Rosen, T. A. Fischer, J. A. Antolak, G. Starkschall, E. L. Travis, S. L. Tucker, et al., "Correlation between lung fibrosis and radiation therapy dose after concurrent radiation therapy and chemotherapy for limited small cell lung cancer," Radiology **221**, 614–622 (2001).

[143] F. H. Attix, *Introduction to Radiological Physics and Radiation Dosimetry,* (Wiley-VCH, 1991).

[144] W. D. D'Souza and I. I. Rosen, "Nontumor integral dose variation in conventional radiotherapy treatment planning," Medical Physics **30**, 2065–2071 (2003).

[145] A. S. Reese, S. K. Das, C. Curle, and L. B. Marks, "Integral dose conservation in radiotherapy," Medical Physics **36**, 734–740 (2009).

[146] R. Castillo, E. Castillo, J. Martinez, and T. Guerrero, "Ventilation from four-dimensional computed tomography: density versus Jacobian methods," Physics in Medicine and Biology **55**, 4661–4685 (2010).

[147] T. Yamamoto, S. Kabus, T. Klinder, J. von Berg, C. Lorenz, J. Billy W. Loo, et al., "Four-dimensional computed tomography pulmonary ventilation images vary with deformable image registration algorithms and metrics," Medical Physics **38**, 1348–1358 (2011).

[148] T. Yamamoto, S. Kabus, T. Klinder, C. Lorenz, J. von Berg, T. Blaffert, et al., "Investigation of four-dimensional computed tomography-based pulmonary ventilation imaging in patients with emphysematous lung regions," Physics in Medicine and Biology **56**, 2279 (2011).

[149] Y. Y. Vinogradskiy, R. Castillo, E. Castillo, A. Chandler, M. K. Martel, and T. Guerrero, "Use of weekly 4DCT-based ventilation maps to quantify changes in lung function for patients undergoing radiation therapy," Medical Physics **39**, 289–298 (2012).

[150] A. Niemierko and M. Goitein, "Modeling of normal tissue response to radiation: The critical volume model," International Journal of Radiation Oncology Biology Physics **25**, 135–145 (1993).

[151] Y. Seppenwoolde, M. Engelsman, K. De Jaeger, S. H. Muller, P. Baas, D. L. McShan, et al., "Optimizing radiation treatment plans for lung cancer using lung perfusion information," Radiotherapy and Oncology **63**, 165–177 (2002).

152 J. A. Christian, M. Partridge, E. Nioutsikou, G. Cook, H. A. McNair, B. Cronin, et al., "The incorporation of SPECT functional lung imaging into inverse radiotherapy planning for non-small cell lung cancer," Radiotherapy and Oncology **77**, 271–277 (2005).

153 S. M. McGuire, S. Zhou, L. B. Marks, M. Dewhirst, F.-F. Yin, and S. K. Das, "A methodology for using SPECT to reduce intensity-modulated radiation therapy (IMRT) dose to functioning lung," International Journal of Radiation Oncology Biology Physics **66**, 1543–1552 (2006).

154 Y. Shioyama, S. Y. Jang, H. H. Liu, T. Guerrero, X. Wang, I. W. Gayed, et al., "Preserving Functional Lung Using Perfusion Imaging and Intensity-Modulated Radiation Therapy for Advanced-Stage Non–Small Cell Lung Cancer," International Journal of Radiation Oncology Biology Physics **68**, 1349–1358 (2007).

155 K. Lavrenkov, J. A. Christian, M. Partridge, E. Niotsikou, G. Cook, M. Parker, et al., "A potential to reduce pulmonary toxicity: the use of perfusion SPECT with IMRT for functional lung avoidance in radiotherapy of non-small cell lung cancer," Radiotherapy and Oncology **83**, 156–162 (2007).

156 I. Munawar, B. P. Yaremko, J. Craig, M. Oliver, S. Gaede, G. Rodrigues, et al., "Intensity modulated radiotherapy of non-small-cell lung cancer incorporating SPECT ventilation imaging," Medical Physics **37**, 1863–1872 (2010).

157 Y. Yu, "Multiobjective decision theory for computational optimization in radiation therapy," Medical Physics **24**, 1445–1454 (1997).

158 C. Cotrutz, M. Lahanas, C. Kappas, and D. Baltas, "A multiobjective gradient-based dose optimization algorithm for external beam conformal radiotherapy," Physics in Medicine and Biology **46**, 2161–2175 (2001).

159 D. Craft, T. Halabi, and T. Bortfeld, "Exploration of tradeoffs in intensity-modulated radiotherapy," Physics in Medicine and Biology **50**, 5857–5868 (2005).

160 A. L. Hoffmann, A. Y. D. Siem, D. den Hertog, J. H. A. M. Kaanders, and H. Huizenga, "Derivative-free generation and interpolation of convex Pareto optimal IMRT plans," Physics in Medicine and Biology **51**, 6349–6369 (2006).

161 R. O. Ottosson, A. Karlsson, and C. F. Behrens, "Pareto front analysis of 6 and 15 MV dynamic IMRT for lung cancer using pencil beam, AAA and Monte Carlo," Physics in Medicine and Biology **55**, 4521–4533 (2010).

162 C. Holdsworth, M. Kim, J. Liao, and M. H. Phillips, "A hierarchical evolutionary algorithm for multiobjective optimization in IMRT," Medical Physics **37**, 4986–4997 (2010).

163 D. Bertsimas, J. N. Tsitsiklis, J. Tsitsiklis, D. Bertsimas, and J. Tsitsiklis, *Introduction to Linear Optimization,* (Athena Scientific, 1997).

164 M. Monz, K. H. Küfer, T. R. Bortfeld, and C. Thieke, "Pareto navigation—algorithmic foundation of interactive multi-criteria IMRT planning," Physics in Medicine and Biology **53**, 985–998 (2008).

165 D. Craft and T. Bortfeld, "How many plans are needed in an IMRT multi-objective plan database?," Physics in Medicine and Biology **53**, 2785–2796 (2008).

166 S. Breedveld, P. R. M. Storchi, and B. J. M. Heijmen, "The equivalence of multi-criteria methods for radiotherapy plan optimization," Physics in Medicine and Biology **54**, 7199–7209 (2009).

167 K. Teichert, P. Süss, J. I. Serna, M. Monz, K. H. Küfer, and C. Thieke, "Comparative analysis of Pareto surfaces in multi-criteria IMRT planning," Physics in Medicine and Biology **56**, 3669–3684 (2011).

168 J. Fiege, B. McCurdy, P. Potrebko, H. Champion, and A. Cull, "PARETO: A novel evolutionary optimization approach to multiobjective IMRT planning," Medical Physics **38**, 5217–5229 (2011).

169   T. Spalke, D. Craft, and T. Bortfeld, "Analyzing the main trade-offs in multiobjective radiation therapy treatment planning databases," Physics in Medicine and Biology **54**, 3741–3754 (2009).

170   H. Stabenau, L. Rivera, E. Yorke, J. Yang, R. Lu, R. J. Radke, et al., "Reduced order constrained optimization (ROCO): Clinical application to lung IMRT," Medical Physics **38**, 2731–2741 (2011).

171   M. McCord and R. de Neufville, "'Lottery Equivalents': Reduction of the Certainty Effect Problem in Utility Assessment," Management Science **32**, 56–60 (1986).

172 A guide to using multi-criteria optimization (MCO) for IMRT planning in RayStation, http://gray.mgh.harvard.edu/attachments/039_MCO_how_to_august_2011_Revision.pdf (03/14/2013)

Appendices

Appendix A

Multiple Anatomy Optimization of Accumulated Dose

W.T. Watkins[1], J. A. Moore[2], M. Sharma[1], C. Dial[1], H. Xu[1], G. D. Hugo[1], J.J. Gordon[1,3], J. V. Siebers[1]

[1]Virginia Commonwealth University, Richmond, VA

[2]Johns Hopkins University, Baltimore, MD

[3]Henry Ford Health System, Detroit, MI

Purpose: To demonstrate the potential benefits of multiple anatomy optimization (MAO) compared to internal target volume (ITV)-based IMRT optimization for lung cancer radiotherapy.

Methods: Four different IMRT plans are developed for ten lung cancer patients using two methods of radiotherapy optimization, the ITV method and MAO. For the ITV method, three different plans are created, corresponding with planning images at the end of inhale, mid-ventilation, and the average CT. Differences between ITV-planned single image 3D-dose and the 10-phase accumulated 4D-dose are examined. The MAO aims to optimize a single fluence to be delivered to all respiratory phases such that the accumulated dose meets the plan objectives. MAO dose distributions are compared to ITV-based cumulative dose distributions in the clinical target volume (CTV), lungs, esophagus, heart and spinal

cord. Dosimetric comparisons and sensitivity to breathing interplay during fractionation for both ITV- and MAO- solutions are examined.

Compared to accumulated 4D-dose, single image 3D-dose systematically overestimates both the dose to 95% of the CTV (ΔD_{95} = 1.29 Gy ± 1.8 Gy, p=10^{-4}) and the target volume at the prescription dose (ΔV_{Rx}=3.4% ± 4.9%, $p = 10^{-4}$) in the ITV-plans considered. CTV-D_{95} is underestimated by greater than 1.75 Gy in 13 of 30 ITV-plans. For OARs, 3D-to-4D differences are less than 3.2% volume (at fixed dose) and less than 1.5 Gy (at fixed volume) for all structures considered. The target dose underestimation can be overcome by optimizing the 4D-dose in MAO, which simultaneously shows potential to spare OARs compared with ITV plans. MAO reduces ipsilateral mean lung dose by 0.70 Gy ± 0.62 Gy (p=10^{-2}, maximum reduction of 2.12 Gy) compared to ITV plans at equal target coverage. All plans considered are robust to breathing variations.

Conclusions: Dose-volume optimization on a stationary image does not ensure accumulated dose coverage to the moving CTV. MAO can remove this dose discrepancy and improve plan quality.

1. Introduction

Approximations utilized in treatment planning of time-dependent anatomy limit the accuracy of radiotherapy (RT) to the thorax and upper abdomen. The current standard for simulation of lung cancer RT is four-dimensional computed tomography (4DCT),[1,2] resulting in several patient images representing the phases of respiration. Many current planning methods combine these 4D-images into a single image (e.g. a stationary average[3] or a maximum intensity projection (MIP)[4–6]) enabling three-dimensional (3D) treatment planning while partially considering inherent motion. However, 3D-planning on 4D-anatomy requires structures that may not physically exist (e.g. internal target volume or ITV) and dose may be calculated on a synthetic image which is not representative of the true anatomy (e.g. MIP). The multiple anatomy optimization (MAO) we utilize in this work includes the phase dependent information available in 4DCT in the plan optimization process. In MAO, dose calculated on each anatomic phase is mapped to a reference phase via deformable image registration (DIR) and summed to estimate the accumulated dose (4D-dose) during plan optimization and delivery. In addition to comparing MAO- and ITV-based

IMRT optimization for a 10 patient cohort, we also quantify differences between 3D- and 4D-dose for several different methods of ITV planning, thereby demonstrating the need for MAO optimization.

Several other authors have investigated differences between 4D-dose and single image dose (3D-dose) for ITV-based plans of lung targets and have shown that delivery of the ITV-based plans would result in under-dosing of the target[7–10] or clinical target volume (CTV). For example, Starkschall et al.[7] found that 3D-dose overestimated target coverage (CTV-D99) in 10 of 15 patient cases considered. While these differences motivate MAO, the need to demonstrate this fact for our patient cohort is necessary to ensure that MAO can indeed compensate for deficiencies in ITV-planning.

ITV-plans assume that CTV-voxels can occupy any position throughout the ITV with equal probability, whereas imaging and DIR may show that target and risk voxels are distributed non-uniformly. This implies the ability to reduce healthy tissue dose through design of a non-uniform dose distribution in the ITV. In fact, motion-inclusive RT planning, including gating[11] and direct tumor tracking,[12,13] do exactly this, they create non-uniform dose distributions in the ITV in order to create a more conformal CTV dose. Unfortunately, these methods rely on continuous and accurate target positioning and tracking, require complicated deliveries, and may only offer advantages for tumors with large motion (> 1cm). Like these methods, MAO produces a non-uniform ITV dose distribution which improves 4D-dose conformality, but unlike them, MAO is delivered under free-breathing conditions, without requiring target location prediction or tracking.

The concept of utilizing MAO to account for intra-fraction motion in IMRT of lung cancer under free breathing is not new. [14–18] While Trofimov et al.[14] introduced the theory of MAO for intra-fraction motion, all prior investigators demonstrated MAO with small patient cohorts (less than 6 patients) in proof of concept studies. Similarly, several authors have considered MAO methods for accommodating rigid set-up uncertainties[19–22], again with small numbers of patients. Both Trofimov et al.[14] and Zhang et al.[16] compared ITV, tracking, gating, and 4D-planning, and found that MAO-methods are comparable to idealized tracking and improve the ITV solution in proof of principle studies. One should note that the accuracy of Zhang et al.'s[16] study is limited since the 4D-dose estimate was accomplished via convolution with a single image 3D-dose instead of DIR-based dose mapping and accumulation. Söhn et al.[20] optimized 4D accumulated dose and also show similar objective achievement between gating and MAO

(or 4D-planning). Together, these studies imply MAO can achieve plans superior to the ITV-method, without reliance on prediction or tracking of tumor positions.

In further studies, Heath et al.[21] compared an MAO approach with optimized margins and included variations in respiratory motion by estimating tumor isocenter displacement based on tidal volume for 5 lung cancer patients. Heath et al.[21] reported that MAO plans were degraded by respiratory motion variation. Similarly, Nohadani et al.[22] include uncertainty in the objective function to ensure that plan objectives were not compromised by intra-treatment breathing variations for 2 patients[23]. Breathing variation has the potential to create large geometric variations within the ITV and may lead to unacceptable dose distributions[24]. Concerns about target motion probability density function (PDF) stability during treatment have slowed clinical implementation of MAO. This study examines the effects of PDF variation based on predictable and controllable factors during fractionated MAO delivery.

Since MAO incorporates both target and risk-structure motion PDFs in plan design, plans can be delivered while a patient breathes freely and comfortably. In the optimization process, MAO designs a non-conformal ITV-dose distribution which takes advantage of predictable intra-fraction motion observed in individual breathing phases. This study compares MAO, which explicitly includes all 4DCT phases in plan definition, and the ITV-method, under the hypothesis that inclusion of this information will lead to superior treatment plans for lung cancer.

2. Methods

To quantify the potential dosimetric benefits of MAO compared to ITV-optimization for lung cancer IMRT, plans were generated using both optimizations on a group of lung cancer patients. Following optimization, target coverage and normal tissue sparing were evaluated and compared for each plan based upon the 4D-dose. Inherent to ITV plans, dose differences estimated by single image 3D-dose and 4D-dose are reported. We also analyzed of the susceptibility of MAO and ITV plans to PDF variations.

2.1 Implementation of MAO

A research plugin interface to the Pinnacle treatment planning system (PINNACLE[3] version 9.100, Philips Medical Systems, Milpitas, CA) is used to implement MAO, including Pinnacles super-position/convolution dose calculation algorithm, the demons fast-symmetric DIR algorithm, and the

built-in deformable dose accumulation algorithm. These processes were implemented from within ORBIT objective functions and optimized using the quasi-Newton (QN) optimizer[25]. For each optimization iteration, fluence was projected onto each anatomy (or respiratory phase image), dose was calculated, then deformed along demons DVFs, and accumulated to the reference image (chosen as the inhale phase). The 4D-dose was evaluated in the ORBIT objective function.

For a collection of N anatomies (N_{ana}) or images, 4D-dose in voxel j in an arbitrary reference anatomy (D_j^{ref}) is expressed as

$$D_j^{ref} = \sum_{a \in N_{ana}} w_a u_j^{ref \to a} D_j^a = \sum_{a \in N_{ana}} \sum_{i \in Ap} w_a u_j^{ref \to a} \left(b_i K_{ij}^a \right) \tag{1}$$

where w_a is the probability of the beam encountering the ath anatomy and $u_j^{ref \to a}$ is the DVF which acts on voxel j in the reference anatomy, pointing to a location in the ath anatomy . The dose is expanded in the latter half of equation 1 to include the ith beamlet weight (b_i) summed over all beamlets in the aperture (Ap). The dose deposition coefficients (or influence matrices) for anatomy a, beamlet i, and voxel j are denoted K_{ij}^a. The composite objective value (f) of n quadratic objectives (N_{obj}) for a region of interest (ROI) with N voxels (N_{vox}) is expressed as

$$f = \sum_{n \in N_{objs}} \sum_{j \in N_{vox}} \omega_n c_n \left(D_j^{ref} - Rx_{n,j} \right)^2 \tag{2}$$

Where ω_n is the weight of the nth objective and c_n includes Heaviside functions and proportionality constants based on the prescription ($Rx_{n,j}$). The beamlet update is calculated using the gradient of the objective function at each dose voxel, and the Hessian is estimated through gradient differences, consistent with the Broyden-Fletcher-Goldfarb-Shanno BFGS -method. These calculations are necessary to determine the search direction. At each step size, 4D-dose is recalculated and is accepted if the resulting objective function satisfies the Wolfe conditions.[26]

The initial approximation of the Hessian in MAO must include importance weighting for voxels throughout the ITV (in order to include the CTV in all phases), but the target objective is the CTV (not the ITV) and only need to be defined in the reference phase. Because the voxels of the reference anatomy determine which voxels are included in the objective function, many are included in the gradient as either OAR or target, when in fact this definition changes depending on the individual phase. Several steps are taken to ensure the entire ITV is considered in each MAO iteration. The Hessian approximation defined in the 3D, ITV-optimization problem is chosen as the
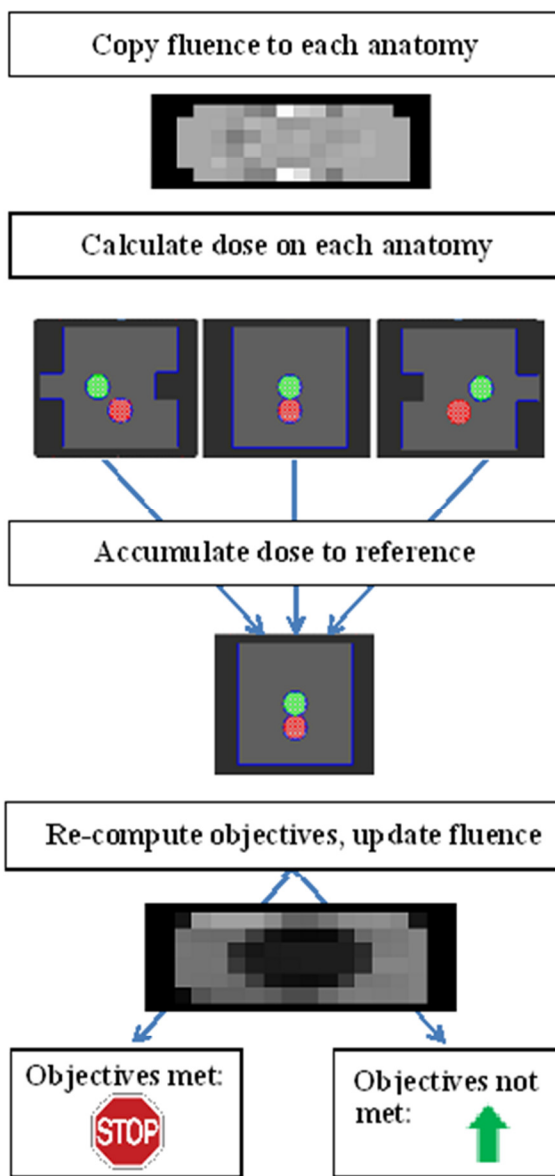
Figure 1. The flow diagram of multiple anatomy optimization (MAO) is shown for a simple, three phase phantom in which one structure moves relative to another.
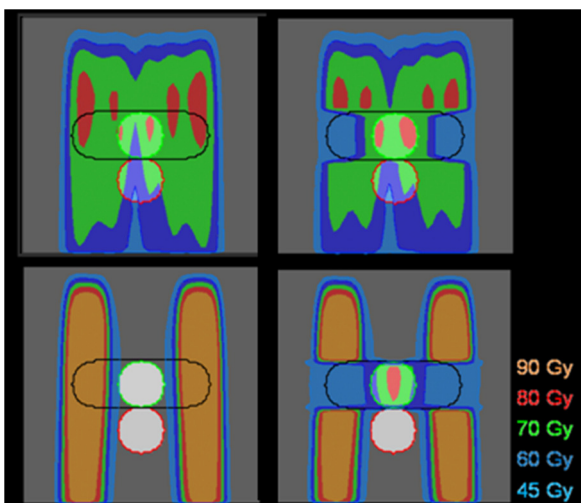
Figure 2. An ITV-optimized dose distribution (top left) compared to an MAO solution (bottom left).

initial MAO estimate. Improvement in the initial Hessian approximation by explicitly including the influence matrices in all phases has the potential to improve MAO convergence. All voxels in the relative complement between the reference-CTV and the ITV are always included in the

optimization problem by minimizing ipsilateral lung dose and the maintaining target coverage throughout the optimization.

Intensity modulated fluence-based optimization is considered in this study, direct aperture optimization (DAO) is a focus of future studies.

The fluence update is determined according to the flow diagram shown in Figure 1 for MAO with a simple phantom example. The phantom includes three phases, and is designed so that in one of the phases, the (moving) target and the (stationary) organ at risk (OAR) are aligned along beam paths. The phantom ITV is the union of the moving CTV in all phase images, and the ITV-plan is optimized so that 95% of the ITV is irradiated to 70 Gy; the risk objective is a maximum dose of 45 Gy. The desired solution is obvious, to reduce the fluence in the beamlets (3D beam elements) which intercept the OAR. The ITV plan cannot reduce the OAR dose and also achieve ITV–D_{95} = 70 Gy because the objectives are conflicting, however, they conflict in only one of the three phase images. In the MAO case, dose is calculated on the moving target and knowledge of the motion drives the solution away from the risk structure. The ITV- and MAO- optimized dose distributions are shown in Figure 2. This simple example demonstrates the method of MAO and the potential for improvement in cases where objective tradeoffs occur.

2.2 Patient Planning

Ten locally advanced non-small cell lung cancer patients (named P1-P10), each with a single 4DCT image set collected on an internal review board-approved study of image-guided adaptive radiation therapy at Virginia Commonwealth University, were used in this study. All subjects are lung cancer patients receiving radiation therapy who gave informed consent. The patient images are imported into the Pinnacle treatment planning system with physician drawn contours on each phase image. Registration is performed using the Insight Toolkit (ITK) implementation of the demons fast-symmetric algorithm[27] as part of the Pinnacle treatment planning system. Displacement vector fields (DVFs) resulting from the registration were produced at an isotropic resolution of 3 mm^3. Propagated physician drawn contours (from the reference maximum inhale phase to all other phases) are visually verified with the physician drawn per-phase contours to ensure consistency of deformations. Dose voxels are designed at the same resolution as the DVF and the dose-voxel grid encompasses the lungs in all phase images (~10^6 dose-

voxels per image). Each plan consists of 7-9 co-planar beams, placed non-uniformly around the patient to avoid both OARs and hot-spots in normal tissues not explicitly considered in the optimization. Four different plan optimizations are performed for each patient with identical beam arrangements, three ITV plans and an MAO plan.

The ITV is a union of the clinical target volumes (CTVs) on all phase images, with each CTV defined as a 5 mm isotropic expansion of the propagated GTV. Inter-fractional set-up error is not considered in this study, so the planning target volume (PTV) is set equal to the ITV. The ITV-optimizations are performed using three different input images, the 30% mid-ventilation phase, the average CT (with structures defined from the 30% phase), and the maximum inhale phase (0% phase, with 0% structures). For the ITV plans, the target objective is 70 Gy to 95% of the PTV (PTV-D_{95} = 70 Gy) with an objective weight at least 100 times that of OAR objectives. The initial objectives include a maximum PTV dose of 80 Gy, cord maximum dose of 40 Gy, for each lung V20 < 10%, esophagus V25 < 5%, and heart V30 < 5%, where the OARs are defined on either the 0% or 30% phase, consistent with the input image phase.

The MAO plans consider the 4D-dose on the reference anatomy, therefore the PTV constraint becomes a (moving) CTV constraint (CTV-D_{95} = 70 Gy, CTV maximum dose < 80 Gy) and OARs are considered in each phase image. In some cases, the lung, esophagus, and heart objectives are impossible to achieve simultaneously in ITV plans. For these cases, to achieve the target criteria in the ITV plans, volume tolerances are adjusted at the listed dose levels by 5% increments until the objective does not dominate the overall objective function, in other cases the OAR-objectives are reduced by 5% relative volume until a non-zero objective score is encountered. The OAR objectives are designed to be difficult to achieve in the ITV plans order to reduce normal tissue complication probability and show potential advantages in MAO.

The maximum contour difference is defined between the ITV and 50% (maximum exhale)-CTV contour and was measured along anterior-posterior (AP), lateral (LAT), and superior-inferior (SI) directions, as shown in **Table** . The centroid CTV motion is also measured in the 3 principle directions, and this data combined with the CTV volume, and the ratio of the two target volumes used in MAO- and ITV- planning (CTV/ITV) is detailed in **Table** for each of the patients considered. The patients are ordered according to the value of the Euclidean norm of the 3D-motion vector, ranging from 0.28 cm for P1 to 0.95 cm for P10. Pearson correlation coefficients are used to examine the relationship between these patient-

specific parameters and differences in 3D-dose and 4D-dose. Unlike the aforementioned studies[14–18], this work focuses on locally advanced NSCLC cases with modest 3D-motion (< 1cm in all cases)

Table 1. Patient Details

Patient	Contour deviation (cm,maximum)			Tumor Centroid Motion (cm)			ITV (cm^3)	Ratio (ITV/CTV)
	AP	LAT	SI	AP	LAT	SI		
1	0.9	0.7	0.3	0.15	0.07	0.24	221.5	0.83
2	0.5	0.7	0.5	0.21	0.13	0.22	294.8	0.89
3	1.5	0.8	1	0.21	0.28	0.17	401.8	0.84
4	0.3	0.3	0.3	0.08	0.24	0.31	60.2	0.78
5	1.5	2.3	1.3	0.16	0.19	0.43	174.6	0.70
6	1.6	1.6	0.7	0.08	0.07	0.57	174.4	0.81
7	1	1.1	0.7	0.30	0.41	0.41	232.6	0.70
8	0.6	1.2	0.6	0.32	0.25	0.56	105.1	0.80
9	1.4	0.7	0.9	0.44	0.15	0.61	173.1	0.79
10	1.9	2.9	1.7	0.36	0.16	0.86	442.4	0.82

2.3 Dosimetric Comparisons

For each of the patient cases, differences in single image approximations of dose (3D-dose) and the 4D-dose, calculated by dividing the ITV-plan monitor units on each of ten phases and accumulating dose to the inhale phase, are reported. This includes mean structure dose and dose-volumes at dose levels described previously. Differences between 3D- and 4D- dose are labeled as dose prediction errors (DPEs). For a general dose or dose-volume measurement m, DPE is defined $DPE_m = D_m^{3D} - D_m^{4D}$. Metrics include mean dose ($<D>$ and $DPE_{<D>}$) and dose at fixed volume (i.e. D_{95} and DPE_{D95}). Similarly, for a structure volume at a fixed dose level x (Vx), the volume prediction error (VPE) is defined as $VPE_{Vx} = Vx^{3D} - Vx^{4D}$. Significance testing of DPE distributions are carried out using one-sided t-tests.

All analysis is performed on the 0% phase image (chosen as the reference image) on the physician-drawn contours of this image. The inhale phase is chosen arbitrarily, but will have some effects on the results. For example, the lung volume in inhale is up to 26% larger than the exhale lung-volume for

these patient image sets, which has the potential to shift the DVH values. The ITV-based 3D- and 4D-dose are compared through DPE and VPE at the objective levels.

The ITV-based 4D-dose is also compared to the MAO-dose (which is inherently 4D). The differences in target and OAR dose-metrics are used to estimate the potential advantages of our MAO approach. The first comparison is between the final ITV and MAO plans at optimized MUs based on identical objectives and objective weights and in general this will result in varying target coverage. In a second comparison, the ITV and MAO plan monitor units are adjusted to a fixed target (4D-dose) D_{95} = 70 Gy, and the potential for OAR sparing is examined.

2.4 Probability density variations in MAO

A source of variability in the 4D-dose estimated by equation 1 is due to variations in the anatomical weight (w_a) for each treatment phase in the time it takes to deliver each beam. Based on the daily starting phase, the w_a will vary during every beam of every fraction unless the treatment time of each beam is coupled with a constant patient breathing period. This variation can be determined by the monitor units per beam (MU_b), dose rate (DR), and a breathing period (T). This predictable interplay effect has been shown to average out over the course of fractionated radiotherapy[8,9] but this may not be the case for MAO dose distributions, where the total dose to the ITV is not necessarily conformal.

To estimate the effects of predictable interplay on MAO and ITV dose distributions, we evaluate N_{ana} images per breathing period (fixed at 10 for this study), a constant, reproducible breathing period ranging from 3-6 seconds, and dose rates ranging from 400-1000 MU/min. This delivery is considered over 30 fractions (N_{fx}), and the monitor units per beam (MU_b) ranges from 4,000 to 10,000. With these values, the expected number of anatomies, $<n_{ana}>$, seen by each beam is calculated according to

$$\left\langle n_{ana} \right\rangle = \frac{MU_b \times N_{ana}}{N_{fx} \times DR \times T} .$$

The calculation of the expected number of anatomies assumes a steady patient breathing pattern and an accurate set of 4D simulation images with small temporal resolution with respect the dose

significance level. For each optimized beam MU, the daily anatomical weightings (w_a) during each fraction can vary from a minimum value (w_a^{min}) to a maximum value (w_a^{max}) estimated by

$$w_a^{min} = \text{floor}\left(\frac{\langle n_{ana}\rangle}{N_{ana}}\right)\Big/\langle n_{ana}\rangle \; ; \quad w_a^{max} = w_a^{min} + 1\big/\langle n_{ana}\rangle \; .$$

where the floor function is the integer component of the expectation value of the number of periods sampled per beam ($\langle n_{ana}\rangle/N_{ana}$).

Dose and dose-response metrics are used to evaluate the effect of anatomic-weight variations on ITV and MAO plans due to breathing interplay. The evaluation is based on the expectation value of CTV-(D95, $\langle D_{95}\rangle$), and the variance in this value, σ. Following the formulation of Bortfeld et al.[8], the expected total physical dose after N_{fx} fractions is $\langle \tilde{D}\rangle = N_{fx}\langle D\rangle$ with total dose variance $\tilde{\sigma} = N_{fx}\sigma$. The expected total physical dose and the dose variance are used to estimate the equivalent biological dose,

$$\langle \tilde{D}_E\rangle = \langle \tilde{D}\rangle + \frac{\tilde{\sigma}^2}{\alpha/\beta + 2\langle \tilde{D}\rangle/N_{fx}}$$

assuming linear-quadratic cell kill with $\tilde{\sigma}$ small. An α/β = 10 Gy is chosen for the NSCLC-CTV dose-response model. The increase in equivalent biological dose with increasing dose variance is balanced by the (possible) reduction in the expected physical dose if under-dosing occurs during individual fractions.

3. Results

3.1. Dose prediction error in ITV plans

Figure 3 shows differences in 3D- and 4D-dose for ITV plans for each patient assuming equal probability weightings for each of the ten phase images (w_a=0.1). The distribution of DPE for mean dose (DPE$_{<D>}$) for all ITV plans ranges from -0.1 Gy to 1.8 Gy for the CTV (p=10^{-7}) but values are relatively small (CTV-DPE$_{<D>}$ > 1.7 Gy in 2 of 30 estimates). There is consistency in CTV-DPE$_{<D>}$ between the three different ITV plans for nine of ten patients to within 0.5 Gy, but P4 shows a dissimilarity. The CTV-DPE$_{<D>}$ = 0.95 Gy in

the 0% plan, and DPE$_{<D>}$ = 1.80 Gy in both the aCT and 30% phase plan. Figure 3 shows the aCT-DVH of the 3D- and 4D-dose. The 3D-dose shows 92% of the ITV exceeds the 70 Gy (prescription) isodose, and 97% of the static CTV is covered by the 70 Gy isodose, however, the ITV volume is 25% larger than the CTV volume, and in the aCT and 30% plan, 10% of the CTV volume falls below 70 Gy. The plan on the inhale-phase is very similar in the ITV shoulder (92% volume at 70 Gy); however, the cold spots are distributed so that DPE$_{<D>}$ is less than 1 Gy. The sign of DPE$_{<D>}$ indicates either over- or under-estimation of accumulated dose by 3D estimates. Positive DPE$_{<D>}$ is observed for the CTV in 28 of 30 cases, overestimating mean dose to moving and deforming CTV by up to 1.8 Gy (2.5% of the prescription dose). DPE$_{<D>}$ is independent of the ITV-
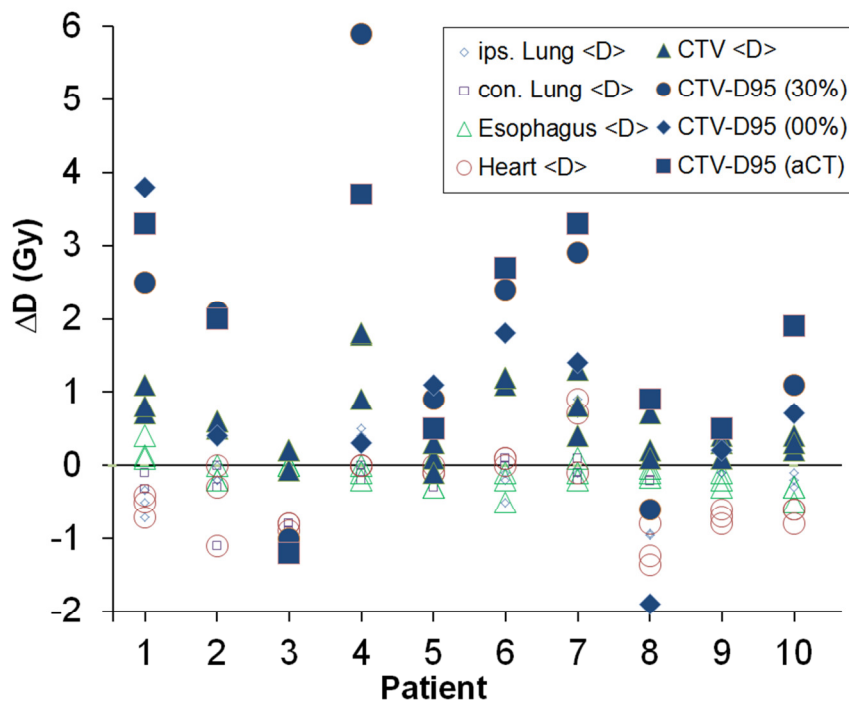
Figure 3. Dose-differences between 3D- and 4D- estimates are shown for CTV and OARs. Three different ITV-plans on mid-ventilation phase (30%), the inhale phase (00%), or average-CT (aCT) create three values of 3D-dose for each structure in each plan.   Compared to accumulated dose over all phases, the CTV- mean dose is overestimated and OAR- mean dose is underestimated in a majority of cases considered. Differences in D95 are noticeably larger than differences in mean dose.

planning image, with mean DPE$_{<D>}$ of 0.5 Gy for plans on both 0% phase (± 0.4 Gy, *p*=0.002) and 30% phase (± 0.4 Gy, *p*=0.007). For plans on aCT, mean DPE$_{<D>}$ = 0.7 Gy ± 0.4 Gy (*p*=0.001). Using two-sample t-tests between the three distributions, only the relationship between the 0%-phase and aCT plans show *p* < 0.1.
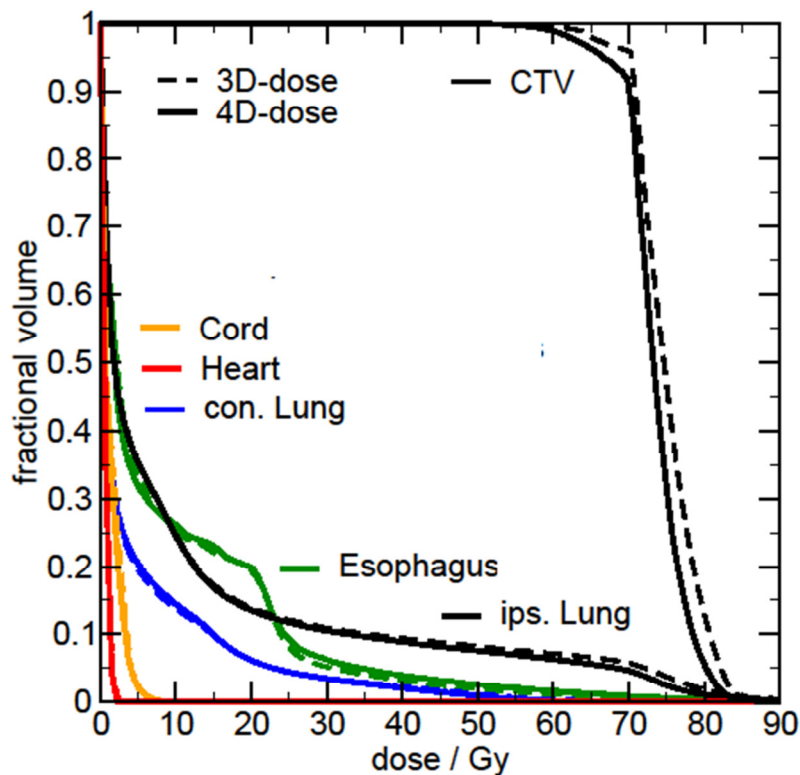
Figure 4. DVH for an ITV plan for Patient 4 showing single image dose on average CT (3D-dose) and accumulated dose (4D-dose). The 3D-dose, using the static CTV contour, gave CTV-D95 = 70.4 Gy, however 4D-dose gave 66.7 Gy. In most of the patient cases considered the OAR doses are similar in 3D- and 4D- estimates.

Negative DPE$_{<D>}$ is observed in 80 of 120 OAR measurements with magnitude of OAR-DPE$_{<D>}$ less than 1 Gy in 116 of 120 estimates. Ipsilateral lung VPE$_{V20}$ ranges from -3.2% to 3.5%; contralateral lung VPE$_{V20}$ similarly ranges from -2.1% to 3.5%. Esophagus VPE$_{V25}$ ranged from -0.2% to 1.3% in the patients considered, and heart VPE$_{V30}$ ranges from -3.2% to 1.2%. DPE for maximum cord dose are negligible in all cases. VPE at objective dose levels exceeds 3% in 3 of 150 cases, with only ipsilateral lung VPE$_{V20}$ showing statistically significant differences (*p*=0.03) from a normal distribution about zero.

A similar trend is observed in CTV-DPE$_{D95}$ as with DPE$_{<D>}$ (shown in Figure 3). In 8 of 10 patients considered, CTV-D$_{95}$ is overestimated in all three ITV-plans compared to the 4D-dose CTV-D$_{95}$. In 4 of 10 cases, DPE$_{D95}$ is greater than 3% of the prescription dose in all three ITV plans including P1, indicating even small tumor motion may be susceptible to DPE. The 4D-dose CTV-V70 also shows consistent underestimation by 3D-ITV plans, with

VPE_{V70}=3.4% ± 4.9% (p=10^{-4}), 7 of 30 plans fail to achieve 4D-dose CTV-V70 > 90%.   Different ITV-planning images result in similar VPE $_{V70}$ (p > 0.2 in all comparisons) showing DPE in ITV planning is independent of planning image. DPE in ITV plans is not correlated to 3D-motion of the CTV (r^2 = 0.002) or CTV to ITV ratio (r^2 = 0.124).

3.2.   MAO compared to ITV plans

The volume of CTV at prescription isodose (V70) is shown in Figure 5 for all plans and all patients. MAO improves CTV-V70 compared to at least one ITV plan for each patient considered. In other cases, the ITV plan results in a 4D-dose exceeding prescription (e.g P3) and MAO reduces the CTV isodose in order to spare OARs. Both P6 and P9 show improvements through MAO planning, ipsliateral lung V20 and heart V30 is less than or equal to all other plans, while also maintaining increased target V70 (in all plans) and D95 (in 4 of 6 plans). In most comparisons of MAO and ITV plans, the reduction in OAR dose-volume levels is small (average ipsilateral V20 decrease is 1.5%±1.1%).   In other cases, there was a more
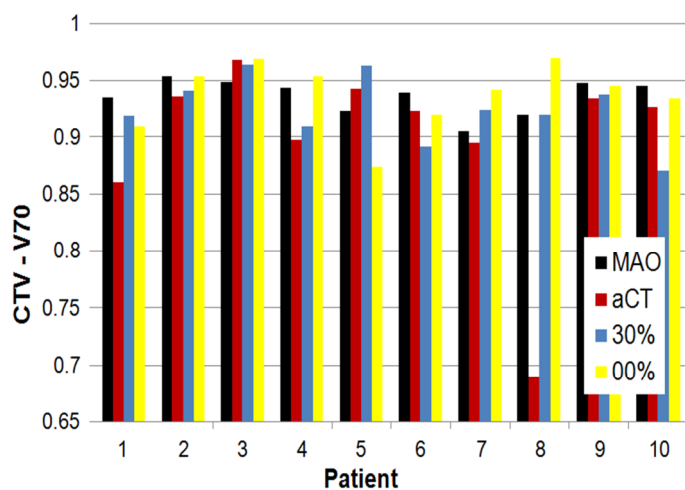
Figure 5. The CTV volume at prescription dose (70 Gy) based on the 4D-dose, assuming equal phase-weightings for each of the plans considered. In seven of ten patients considered, at least one plan fails to deliver 70 Gy to 90% of the CTV, however the MAO solution can ensure accumulated dose meets prescription.

pronounced difference, for example in P3, the MAO plan results in V70 = 94.9% of the CTV, compared to the 30%-ITV plan with V70 = 96.4%. In this case, by reducing the target V70 to prescription MAO reduces ipsilateral mean lung dose is reduced by 2.2 Gy (a reduction in V20 of 7%) even though 3D motion for this case is just 0.39 cm.

Overall, MAO improves V70 by an average of 3.5% (±4.3%, p=0.01) compared to ITV plans at optimized MUs. Increased D95 with MAO compared to ITV planning is not significant, on average 0.35 Gy ± 1.27 Gy (p=0.8), but is greater than 1 Gy in 8 of 30 cases. Two of the DVH's are shown in Figures 6 and 7 for patients 6 and 10, respectively. The MAO- and ITV- DVH comparison for these two patients display

common features observed with many of the ten patients, notably, increased CTV coverage in the MAO plan with similar dose-volumes for OARs.
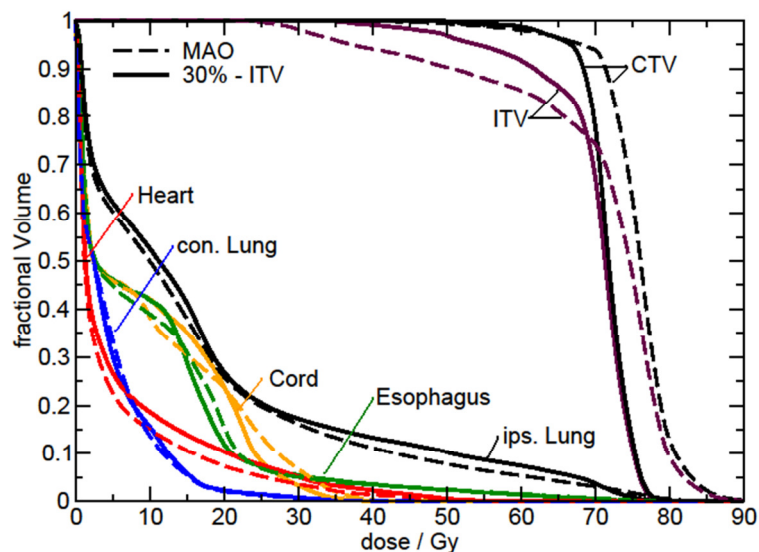
Figure 6. Accumulated dose DVH for Patient 6 based on delivering the 30%-ITV plan and the MAO plan. The ITV is not covered in the MAO plan (as it is not an objective), but the CTV coverage is improved while reducing ipsilateral lung and heart doses.
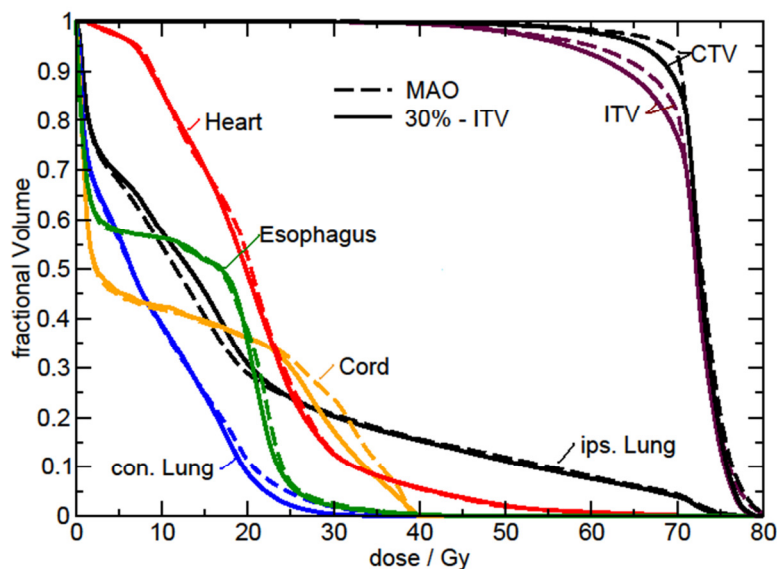
Figure 7. Accumulated dose DVH for Patient 10 based on delivering the 30%-ITV plan and the MAO plan. MAO increases CTV-D95 to prescription, while simultaneously reducing ipsilateral lung dose.

In order to show the potential to spare organs at risk in MAO, the 30%-ITV plan and the MAO plan monitor units are normalized so that 4D-dose CTV-D_{95} = 70 Gy. In this set of normalized plans, OAR

volume sparing at objective dose levels is evident in five of the ten cases, P3, P4, P6, P7, and P10, as shown in Figure 8. In the other five cases the combined OAR-volume sparing at objective dose levels is less than 2%. The potential for OAR sparing in MAO is not trivially correlated to 3D-motion (r^2 = 0.08, p = 0.8). The lateral motion showed a weak correlation (r^2 = 0.42, p = 0.2), the largest CTV motion is measured in the lateral direction for P3 (0.28 cm) and P7 (0.41 cm) and MAO reduces total of all OAR volumes at prescription by 16.3% and 5.9% for these cases. In all other cases, the largest CTV motion direction is superior inferior and the 3D-motion for the CTV for P4, P6, and P10 is dominated by SI motion.
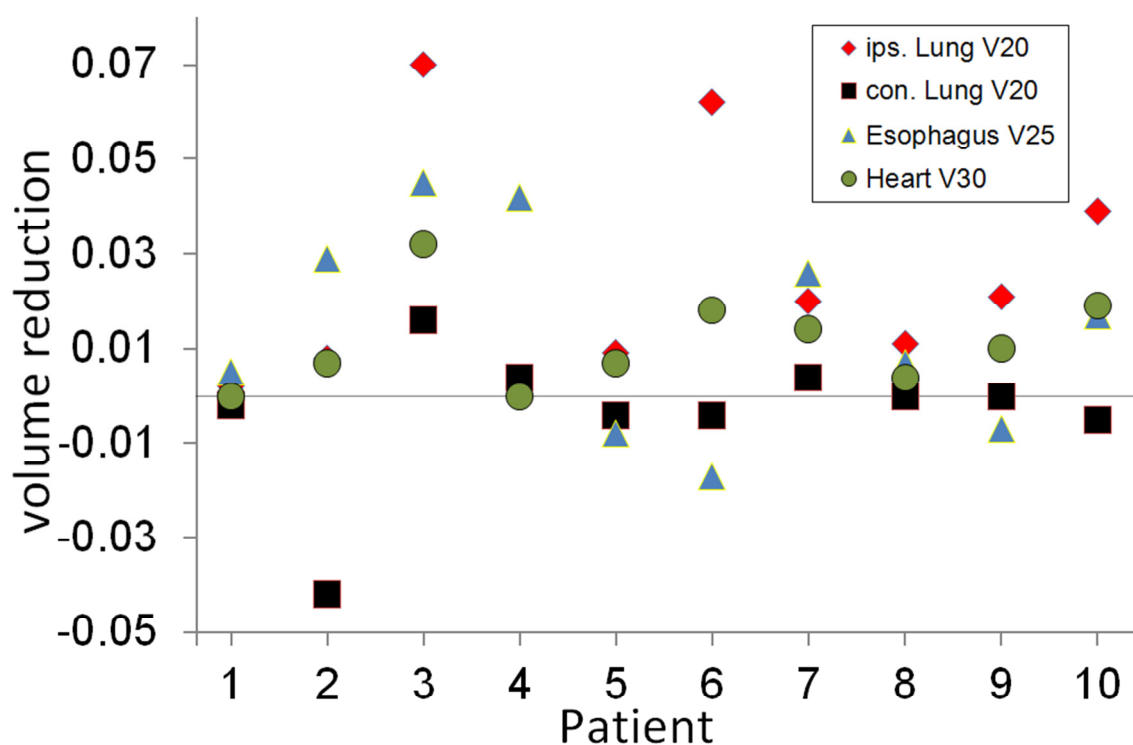
Figure 8. At fixed CTV-D$_{95}$, the decrease in relative volume of OARs at objective dose levels is shown using the MAO approach, compared to the 30%-ITV plan. There is potential to spare organs at risk using MAO for patient 3, 4, 6, 7, 8, and 9.

3.3. Probability density variations in MAO

For 10-phase images per breathing period, on any given treatment day, the individual anatomical weightings (w_a) range from approximately 0.09 to 0.11 per phase image if the patient breathes consistently with the pattern observed during simulation. This variation (10% of the nominal value) is estimated based on simulations of the anatomical weights and their standard deviation for 30 fractions. These values bound all scenarios considering the breathing period (T=3-6 sec), dose rate (400 – 1000 MU/min), and beam monitor unit variations (4,000-10,000 per beam). Even in an extreme scenario (i.e. 4,000 MU beam delivered at 1,000 MU/min to a patient with a 5 second breathing period) sampling a random starting phase over 30 fractions results in an average anatomical weight ranging from 0.094 to 0.106.

Based on these findings, the sensitivity analysis of MAO and ITV dose distributions to PDF variation is carried out considering three scenarios: nominal weighting (w_a=0.1) on all phases, distribution of the maximum weights (w_a^{max} = 0.11) on the five phases surrounding inhale (80% - 20%), and distribution of the minimum weight (w_a^{min} = 0.09) on the five phases surrounding inhale. The three dose values are used to calculate the expected dose and dose variance for the CTV.

Both P1 and P3 show negligible differences in dose resulting from equal delivery to all phases (w_a=0.10) and the other two scenarios considered, the variance in CTV-D95 is 0.01 Gy for both ITV and MAO plans so that the effective dose approximately equals the physical dose. For P3, the range of dose differences in the considered scenarios are -4.02 Gy to 2.12 Gy for the MAO plan and -4.2 Gy to 1.93 Gy for the ITV plan when considering the entire dose-volume, but these differences occur outside the ITV.

Increased sensitivity to PDF variation is observed for the MAO dose-distribution for P6, with a CTV-D_{95} standard deviation of 1.4 Gy in the MAO plan and 0.6 Gy in the 30%-ITV plan. A coronal slice of the optimized MAO and ITV dose distributions are shown in Figure 9. The dose shows the SI motion is incorporated in the MAO solution for this patient with hotspots (or horns) on the superior and inferior borders of the target. In the case of P7 or P10, where the standard deviation in D95 is 0.2 Gy and 0.01 Gy, respectively, both MAO and ITV plans are robust to PDF variations considered. The average D_{95} for P1, P3, P7, and P10 is equal to the D_{95} based on nominal weightings (to within 0.10 Gy) and the biological dose does not differ from the physical dose by more than 0.10 Gy in any of the cases

considered, implying the MAO solutions are robust to PDF variations occurring due to dose-rate and breathing interplay. However, the effects of motion along a principle axis (i.e. P6) were more pronounced than a distribution along multiple axes. The dose variation over the entire dose-grid is greater in the MAO distributions, but dose variance due to breathing interplay does not affect the biologic equivalent dose in the cases considered.
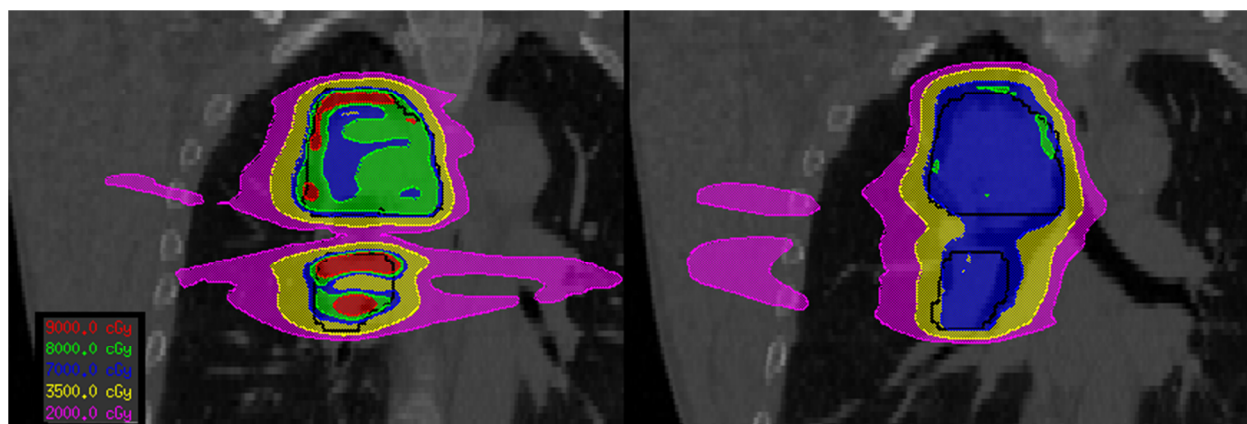
Figure 9. Coronal slice of the MAO dose distribution (left) and the ITV dose distribution (right) calculated on a single anatomy (inhale), where the CTV is drawn in black. The MAO dose distribution (left), creates CTV- hot and cold spots in individual phase doses for this patient to improve accumulated dose, this plan is more susceptible to interplay effects than any considered.

4. Discussion

Differences in 3D-and 4D-dose CTV-D_{95} exceed 2.5% in at least one ITV-plan for 6 of the 10 patients considered. For mean dose simulations, $DPE_{<D>}$ is consistent with the findings of Rosu et al.[4] and Glide-Hurst et al.[3] who have shown $DPE_{<D>}$ to be within ±3% of 4D-estimates. The $DPE_{<D>}$ and DPE based on other dose metrics which sum dose values over a region of interest (e.g. equivalent uniform dose) should be small under approximate conservation of mass and energy in different considered anatomies. However, when considering dose-volume metrics, cold spots in the ITV have the potential to create a relatively larger cold spot in the (smaller) CTV volume.

The value of CTV-DPE in an ITV plan depends on the motion of the CTV (or the CTV-PDF) and the dose distribution within the ITV; implying that dose differences are both patient- and plan- specific. Even in

cases of small motion the CTV-D_{95} can potentially be compromised, as shown for P1 and P4. A completely conformal dose within the PTV will result in zero DPE under the assumption of conservation of mass and energy in multiple anatomies. In other words, there is no motion-PDF which will alter the CTV dose if the PTV dose is completely uniform in all breathing phases. Uniformity within the PTV, however, is often relaxed to spare OARs creating the potential for degradation of the conformality of the moving CTV. For OARs, the 4D-dose was observed to be larger than 3D-dose in most cases, but this difference is less than 3.2% for lung, heart, spinal cord, and esophagus for all patients and all ITV-plans considered. Mean dose 3D- and 4D- differences for OARs are less than 1.5 Gy in all estimates.

A simple evaluation of a worst case scenario in 3D-planning of moving anatomy can indicate the possibility of large CTV-DPE. Rather than evaluate the CTV coverage based on a static contour, the CTV coverage is robust against DPE when, for each voxel of the CTV, the minimum dose in the PTV is sampled. A worse-case sampling of the PTV dose distribution will establish a limit on DPE and can be used to ensure an un-acceptable under-dosing of the CTV cannot occur in an ITV plan. A similar method was proposed by Niemierko and Goitein[28] in sampling dose distributions. The relatively small dose/volume differences in 3D- and 4D- dose for OARs can be accounted for through tolerance levels in OAR objectives. With a worst case sampling and additional OAR tolerance, new methods of optimization are not required clinically, and will ensure target coverage is not compromised.

In this study, intensity-based optimization of accumulated dose is performed within a commercial treatment planning system. Others have proposed similar methods in proof of principle studies, especially in cases of large CTV motion[14–18]. This work specifically looked at differences in 3D- and 4D-dose, not only to overcome ambiguity between the two, but to investigate the advantage of phase-specific dosimetry in MAO. This study includes cases of moderate CTV motion which may be more likely to be encountered clinically. MAO can ensure accumulated dose meets the planning objectives based on a known PDF. For five of ten patients, the MAO solution shows some advantages compared to ITV planning. The advantage of MAO is not well correlated to 3D- motion or the size of the CTV. The ITV plan assumes a uniform distribution of CTV voxels throughout the ITV, so that if motion is distributed uniformly, the CTV-PDF may resemble a uniform distribution and may explain why the MAO results in a plan nearly identical to ITV in five of the patients considered. Without some distinguishing features in the CTV-PDF, there may not be advantages in using the MAO technique.

There are limitations to MAO, and there are many hurdles to overcome in order to move this technology into clinical use. In order to implement the method of MAO described herein clinically, calibration of an accumulated, 4D-dose algorithm with delivered dose to mobile, deforming structures using a realistic deformable phantom is necessary (see, for example Kashani et al.[29]). Creation of a PTV in order to account for set-up error is another obstacle, however the MAO software is interfaced with methods to optimize margins to account for both random[30] and systematic[31] errors. Of these challenges, the sensitivities of the MAO dose distribution with respect to anatomical changes during each treatment and over the course of fractionated radiotherapy (including tumor regression) will require consideration. Because MAO depends directly on the phase images and the DVFs connecting them, the technique may be sensitive to realistic anatomic variations, at least when compared to the more conformal ITV solutions.

The effects of fractionated interplay is considered in this study, however the effect of irregular breathing may be much more significant. The probability of encountering the phase images observed in 4DCT during treatment may alter anatomical weights (in equation 1) by more than 10%. The effect of breathing variation is a focus of future studies. MLC interplay effects (which vary the anatomical weighting for each aperture) are also a concern. MLC interplay can be directly incorporated in the MAO solution through DAO including a high frame-rate of per-aperture dose calculation. The solutions presented herein are based on fluence optimization, not MLC conversion. Generalizing the fluence optimization to multi-aperture DAO will require sensitivity analysis with respect to varying anatomical weights, which grows as the delivery time of each aperture is reduced. It is plausible that the MLC delivery of the plan must be coupled to the patient specific motion in cases of limited treatment time for each aperture, which is especially relevant to arc-based therapy (see for example Ma et al.[32] or Chin and Otto[33]). Court et al.[34] have investigated MLC sequencing to ensure the interplay effect results in dose distributions within a known tolerance, and such a method may be applicable to MAO dose distributions.

The current implementation of MAO takes approximately 20 hours per patient using a single core x86 processor. Each optimization iteration requires several minutes, as dose is calculated for 7-9 beams on 10 images multiple times during each iteration, with calculation time on a single core for each beam ranging from approximately 3-6 seconds. Using a pencil beam dose calculation on multiple CPU cores

(i.e. 8 cores) will speed up this calculation by a factor of 40 or more, but will sacrifice accuracy in heterogeneous lung. The preferred method of dose calculation to pencil beam may be GPU-based superposition-convolution[35]. Of the total time for optimization, approximately 70% was spent in dose calculation on the representative anatomies, with the other 30% of time spent on dose accumulation and data transfer. Because of DIR and minimization of optimization objectives, however, the method relies only on a single contour set and a beam arrangement. User interaction is minimal, so that the resulting plan may approach a best-case scenario in terms of target coverage and OAR sparing and can be optimized off-line.

5. Conclusions

Multiple anatomy optimization has been implemented in the Pinnacle treatment planning system for free breathing radiotherapy of lung cancer. The optimization explicitly includes accumulated dose on multiple anatomies as presented in 4DCT simulation images. The method shows potential advantages compared to ITV planning for half of the patients considered, and does not require real-time tracking or prediction. The solutions are robust to breathing interplay, implying high dose rates can be used in traditional fractionation.

Acknowledgements

References

[1] P.J. Keall, G. Starkschall, H. Shukla, K.M. Forster, V. Ortiz, C.W. Stevens, S.S. Vedam, R. George, T. Guerrero, and R. Mohan, Physics in Medicine and Biology **49**, 2053 (2004).

[2] D.A. Low, M. Nystrom, E. Kalinin, P. Parikh, J.F. Dempsey, J.D. Bradley, S. Mutic, S.H. Wahab, T. Islam, G. Christensen, D.G. Politte, and B.R. Whiting, Medical Physics **30**, 1254 (2003).

[3] C.K. Glide-Hurst, G.D. Hugo, J. Liang, and D. Yan, Med Phys **35**, 5269 (2008).

[4] R.W.M. Underberg, F.J. Lagerwaard, B.J. Slotman, J.P. Cuijpers, and S. Senan, International Journal of Radiation Oncology Biology Physics **63**, 253 (2005).

[5] K. Park, L. Huang, H. Gagne, and L. Papiez, Int. J. Radiat. Oncol. Biol. Phys. **73**, 618 (2009).

[6] E. Rietzel, A.K. Liu, K.P. Doppke, J.A. Wolfgang, A.B. Chen, G.T.Y. Chen, and N.C. Choi, International Journal of Radiation Oncology Biology Physics **66**, 287 (2006).

[7] G. Starkschall, K. Britton, M.F. McAleer, M.D. Jeter, M.R. Kaus, K. Bzdusek, R. Mohan, and J.D. Cox, International Journal of Radiation Oncology Biology Physics **73**, 1560 (2009).

[8] T. Bortfeld, K. Jokivarsi, M. Goitein, J. Kung, and S.B. Jiang, Physics in Medicine and Biology **47**, 2203 (2002).

[9] S.B. Jiang, C. Pope, K.M.A. Jarrah, J.H. Kung, T. Bortfeld, and G.T.Y. Chen, Physics in Medicine and Biology **48**, 1773 (2003).

[10] R.I. Berbeco, C.J. Pope, and S.B. Jiang, Journal of Applied Clinical Medical Physics **7**, (2006).

[11] P.J. Keall, V.R. Kini, S.S. Vedam, and R. Mohan, Australas Phys Eng Sci Med **25**, 1 (2002).

[12] S.W. D McQuaid, Physics in Medicine and Biology **51**, 4819 (2006).

[13] Y. Suh, A. Sawant, R. Venkat, and P.J. Keall, Physics in Medicine and Biology **54**, 3821 (2009).

[14] A. Trofimov, E. Rietzel, H.-M. Lu, B. Martin, S. Jiang, G.T.Y. Chen, and T. Bortfeld, Physics in Medicine and Biology **50**, 2779 (2005).

[15] M. Söhn, M. Weinmann, and M. Alber, Int. J. Radiat. Oncol. Biol. Phys. **75**, 906 (2009).

[16] P. Zhang, G.D. Hugo, and D. Yan, International Journal of Radiation Oncology*Biology*Physics **72**, 1221 (2008).

[17] E. Heath, J. Unkelbach, and U. Oelfke, Medical Physics **36**, 3059 (2009).

[18] O. Nohadani, J. Seco, and T. Bortfeld, Physics in Medicine and Biology **55**, 5189 (2010).

[19] J.G. Li and L. Xing, Medical Physics **27**, 1573 (2000).

[20] M. Birkner, D. Yan, M. Alber, J. Liang, and F. Nüsslin, Med Phys **30**, 2822 (2003).

[21] J. Unkelbach and U. Oelfke, Physics in Medicine and Biology **49**, 4005 (2004).

[22] D.L. McShan, M.L. Kessler, K. Vineberg, and B.A. Fraass, Med Phys **33**, 1510 (2006).

[23] D. Rueckert, L.I. Sonoda, C. Hayes, D.L.G. Hill, M.O. Leach, and D.J. Hawkes, Medical Imaging, IEEE Transactions On **18**, 712 (1999).

[24] K. Sheng, J. Cai, J. Brookeman, J. Molloy, J. Christopher, and P. Read, Medical Physics **33**, 3321 (2006).

[25] J. Löf, Development of a General Framework for Optimization of Radiation Therapy, Stockholm University, 2000.

[26] J. Nocedal and S.J. Wright, *Numerical Optimization* (Springer, New York, 1999).

[27] T. Vercauteren, X. Pennec, A. Perchant, and N. Ayache, Neuroimage **45**, S61 (2009).

[28] A. Niemierko and M. Goitein, Medical Physics **17**, 753 (1990).

[29] R. Kashani, M. Hub, M.L. Kessler, and J.M. Balter, Medical Physics **34**, 2785 (2007).

[30] J.A. Moore, J.J. Gordon, M.S. Anscher, and J.V. Siebers, Medical Physics **36**, 3880 (2009).

[31] J.A. Moore, J.J. Gordon, M. Anscher, J. Silva, and J.V. Siebers, Medical Physics **39**, 1102 (2012).

[32] Y. Ma, D. Chang, P. Keall, Y. Xie, J. Park, T.-S. Suh, and L. Xing, Med Phys **37**, 5627 (2010) [33] E. Chin and K. Otto, Med Phys **38**, 2698 (2011).

[34] L. Court, M. Wagar, R. Berbeco, A. Reisner, B. Winey, D. Schofield, D. Ionascu, A.M. Allen, R. Popple, and T. Lingos, Medical Physics **37**, 4 (2010).

[35] R. Jacques, R. Taylor, J. Wong, and T. McNutt, High-Performance Medical Image Computing and Computer Aided Intervention Workshop (2008).

[36] H. Zhong and J.V. Siebers, Phys Med Biol **54**, 5815 (2009).

[37] H. Zhong, T. Peters, and J.V. Siebers, Physics in Medicine and Biology **52**, 4721 (2007).[38] F.J. Salguero, N.K. Saleh-Sayah, C. Yan, and J.V. Siebers, Med Phys **38**, 343 (2011).

Appendix B

Dose Differences in ITV Planning of Time Dependent Anatomy

W.T. Watkins[1], J. A. Moore[2], B. Cai[1], N. R. Anderson[1], C. Dial[1], G. D. Hugo[1], J. V. Siebers[1]

[1]Virginia Commonwealth University, Richmond, VA

[2]Johns Hopkins University, Baltimore, MD

Purpose / Objectives. Tumor motion and deformation create ambiguity in target dose coverage when prescribing to an internal target volume (ITV). This work quantifies dose differences between single image dose approximations and deformed, accumulated dose for five lung cancer patients for several different measures of target coverage.

Materials / Methods. IMRT plans are developed to deliver 70 Gy to 95% of the ITV volume on a mid-ventilation image (mid-vent) and on an average CT image (aCT) for five lung cancer patients. Dose calculations are performed for delivery to each of ten phase-sorted 4DCT images, and deformable dose accumulation is carried out utilizing a fast-symmetric Demons algorithm for registration. The accumulated dose distribution (or 4DD) is compared to the single image dose (or 3DD) through five metrics, the relative target volume at prescription isodose, minimum dose, and gEUD for a = 1, -5, and -20 to represent mean dose, radiosensitive tumor coverage, and aggressive tumor coverage, respectively. Dose measures are considered for the gross tumor volume (GTV) and a 5 mm isotropic expansion of the GTV to represent the clinical target volume (CTV) in each of the plans.

Results. In nine of ten plans, CTV prescription isodose volume is overestimated in 3DD compared to 4DD (mean, 1 standard deviation of 9.9% ± 9.7%, range of -5.1% to 19.8%). Mean dose differences ($gEUD_{a=1}$) in the CTV are 1.55 Gy ± 1.20 Gy and are overestimated in all ten 3DD calculations (range of 0.2 Gy to 3.8 Gy); however mean GTV dose differences are not significant (0.78 Gy ± 1.32 Gy, p=0.0948). Increasing the importance of cold-spots within the target, the differences in 3DD and 4DD become patient specific, with 3DD overestimating CTV-$gEUD_{a=-5}$ and GTV-$gEUD_{a=-5}$ in five of ten plans. Measured differences between 3DD and 4DD for $gEUD_{a=-5}$ range from -6.5 Gy to 3.8 Gy for CTV, and from -1.1 Gy to 3.7 Gy for GTV. Measured $gEUD_{a=-20}$ is also patient-specific for both CTV (range -3.9 Gy to 9.6 Gy) and GTV (range -9.9 Gy to 2.3 Gy) and the magnitude of observed differences increased with decreasing a. As the value of a is decreased in gEUD computations, the correlation with minimum target dose increases from 0.658 for a=-5 to 0.900 for a=-20. Planning on aCT decreases gEUD differences compared to plans on mid-vent in 12 of 15 CTV measurements, and in 10 of 15 GTV measurements.

Conclusions. Differences in 4D-accumulated dose and 3D dose on a single image are evident from dose volume histogram levels. However, for mean dose these differences are veiled, which is expected since this is a summation of similar dose values, assuming only slight deviations of conservation of mass and energy among different 4D images. When magnifying the importance of low dose voxels decreasing a in gEUD, differences in 3DD and 4DD become patient and plan specific, and should be considered in radiotherapy planning.

Appendix C

The Effects Of Interplay On Accumulated Dose In High-dose Rate Stereotactic Body Radiotherapy Of Lung Cancer

W. Watkins*[1], W. Y. Song*[2], G. D. Hugo*[1], E. Weiss*[1], J. V. Siebers*[1].

[1]*Virginia Commonwealth University, Richmond, VA*

[2]*University of California San Diego, San Diego, CA*

Purpose/Objectives. To determine the dosimetric effects of beam-delivery and breathing-phase interplay as a function of dose rate for lung cancer stereotactic body radiation therapy (SBRT).

Methods/Materials. For four lung cancer patients who underwent 4DCT and received SBRT under free-breathing conditions, 4*12 Gy/fraction is prescribed to 95% of the planning target volume (PTV), defined as a 3-5 mm expansion of the internal target volume. The plan is optimized on a single planning image (three on average-CT, one on a single phase). For each patient, this study estimates accumulated dose to 95% of a reference-phase GTV plus a 3-5 mm margin ($D95_{acc}$). In one approximation of $D95_{acc}$, the dose is assumed to be independent of beam-on time, so that dose is delivered to the same anatomy captured in 4DCT (i.e. equi-weighted respiratory phase images). This approximation of $D95_{acc}$ is compared to the planned PTV-D95. In reality, dose is dependent on the 4DCT phases encountered during treatment which in turn depends on treatment dose rate, per-aperture MUs, and the interplay of beam delivery with patient-specific breathing patterns. In order to estimate the effects of interplay on $D95_{acc}$, ten deliveries are simulated per patient by randomly sampling patient-specific breathing patterns for durations determined from per-beam MUs and dose rates 1000, 1400, and 2400 MU/min. This methodology assumes a conformal delivery (i.e. one aperture per beam). Differences between $D95_{acc}$ for each simulated delivery and the standard deviation in simulated $D95_{acc}$ are reported.

Results. Using the equi-weighted CT acquisition phases, the (nominal) $D95_{acc}$ is greater than the planned dose to the PTV by 0.1 Gy, 1.3 Gy, 1.3 Gy, and 2.8 Gy for the 4 patients considered. Beam-on times range from 2.7 seconds (at 2400 MU/min) up to 22.6 seconds (at 1000 MU/min). Including interplay, the maximum difference between the 10 estimates of $D95_{acc}$ is less than 0.71 Gy for all patients. The standard deviations of dose between the 10 simulated deliveries are < 0.11 Gy when delivered at 1000 MU/min; < 0.12 Gy when delivered at 1400 MU/min; and < 0.26 Gy when delivered at 2400 MU/min. The average $D95_{acc}$ of the 10 simulated deliveries for each dose rate differ by < 0.09 Gy for all patients; and average $D95_{acc}$ is greater than or equal to the nominal $D95_{acc}$ for ¾ patients (by up to 1.5 Gy).

Conclusions. In the cases considered, D95 to the moving target is approximately independent of beam-on time. Interplay between beam-on time for high dose-rate treatment (up to 2400 MU/min) and patient-specific breathing results in target dose variations < 0.71 Gy assuming one aperture per beam. Further studies are needed to ensure interplay effects do not compromise intended treatment in dynamic IMRT delivery.

Appendix D

Dose To Mass In Lung Cancer Radiation Therapy

W.T. Watkins[1], J. A. Moore[2], G. D. Hugo[1], J. V. Siebers[1]

[1]Virginia Commonwealth University, Richmond, VA

[2]Johns Hopkins University, Baltimore, MD

Purpose. To integrate mass and density information in structure definition, in dosimetric evaluation, and in intensity-modulated radiotherapy (IMRT) plan optimization for lung cancer radiotherapy.

Methods. Four-dimensional computed tomography (4DCT) image sets for 8 lung cancer patients are analyzed in this study. An expert physician has delineated ipsilateral lung and gross tumor volumes (GTVs) on all phases of several of the patient-image sets. Mass and volume of lung and GTV, as delineated by the physician in the phase-sorted 4DCT images, are compared to deformed contours defined through propagation of inhale-phase contours according to deformable image registration (DIR). In order to incorporate mass in dosimetric evaluation, dose-volume histograms (DVHs) are compared to dose-mass histograms (DMHs) for each patient using (DVH-based) IMRT optimized-dose distribution on the inhale phase image and on the average-4DCT density. For these same plans and images, plans based on DMH-optimization are compare to DVH-based plans.

Results. The coefficient of variance (*CV*) of ipsilateral-lung mass, defined across different phases of each 4DCT image set, is less than 5.6% for physician contours and less than 2.4% for all DIR-contours. GTV mass across respiratory phases is also approximately constant, with physician contoured *CV* < 4.7% in all image sets and DIR-based *CV* < 3.5% for 7/8 patients. In one case which included visible artifacts near the GTV, DIR resulted in a relatively large mass variation (*CV* > 8.5%). Incorporating mass into dosimetric evaluation revealed differences between DVH and DMH less than 3% for the spinal cord, heart, and

esophagus across all dose levels. In the lungs and targets, differences between DVH and DMH often exceed 5%. Differences between lung DVH and DMH were normally distributed, showing plan and patient dependence. In optimizing DMH levels in IMRT, target and ipsilateral lung doses are adjusted to account for large differences in dose to massive regions within each structure .

 Conclusions. Incorporating mass in lung cancer radiation therapy; in delineation, evaluation, and plan optimization, offers potentially useful information.

1. Introduction

The dose volume histogram (DVH) is an integral component in modern radiotherapy (RT) planning and evaluation. The DVH was first introduced as a proportion of posterior rectal wall as a function of dose by Shipley *et al* (1979) whose stated aim was "to develop practical clinical techniques for the delivery of a well-localized beam."   They unquestionably succeeded in this aim, but it is interesting to note that the first DVH plotted the relative volume of posterior rectal wall at dose, not the relative volume of the entire rectum (including contents) as is commonly done today. The entire rectum is composed of both functional and non-functional sub-units. Nioutsikou *et al* (2005) describe the inherent assumption that each voxel (of equal volume) has equal importance in DVH evaluations. Combine this assumption with prospective cell-kill models (e.g. linear-quadratic model) which rely fundamentally on the number of cells irradiated, and there is an evident disconnect between DVH measures and radiation damage.

The current standard to estimate prospective radiation damage is based on the linear-quadratic model, where the surviving fraction (N/N_0) of cells is estimated according to $N/N_0 = exp\left(-\alpha D - \beta D^2\right)$. In parallel organs, the number of surviving functional sub units (FSUs) of an organ will determine the complication probability (Niemierko and Goitein 1993). Under the assumption that FSU density is directly proportional to physical density, the biologic effect of an equal dose delivered to reduced mass is directly proportional to a reduction in complication or control probability. This assumption does not require all cells in a voxel to function equally; it requires the relative proportion of FSUs to be directly proportional to voxel density. In normal tissues, there is an added advantage in delivering radiation

through less massive regions, i.e. a reduction in radiation path length will reduce the delivered dose through normal tissue.

Consider the integral dose (Carlsson 1963, Attix 1991), dose integrated over a structure mass composed of n voxels is $\int D\,dm = \sum_n \frac{E_n}{m_n} m_n = \sum_n E_n = E^{abs}$. The integral dose in a structure of mass elements is the absorbed energy. Integral dose within n volume elements is $\int D\,dV = \sum_n D_n \frac{m_n}{\rho_n} = \sum_n \frac{E_n}{\rho_n}$, or the sum of energy absorbed per unit density (ρ) of each voxel. This quantity (integral dose over volume) is meaningful in homogenous media, where energy per unit density is directly proportional to the energy absorbed. Fundamental limitations of radiation delivery have been described based on conservation of integral dose in spherical shells (e.g D'Souza and Rosen 2003 or Reese et al 2009); however, in heterogeneous structures dose is not conserved among different beam/delivery conditions. Specifically, delivering a larger proportion of fluence through a region of lower density will reduce the dose in such a spherical shell. We hypothesize that consideration of structure mass in plan development through the dose-mass histogram (DMH) has the potential to lead to reduce integral dose to normal tissues and will result in a superior RT plan.

The differences in DVH and DMH are clear in theory but the magnitude of such differences may not be clinically significant. There is evidence that outcome (or toxicity) correlates with dose-volume parameters for many organs, without consideration of mass. Mavroidis *et al* (2006), commenting on the work of Nioutsikou *et al* (2005), showed for numerical phantoms with Gaussian dose distributions the differences between DVH and DMH are greater than 5% in lung. For a pair of tangential photon fields in a breast cancer case, they also show clinically-significant (> 5%) differences between DVH and DMH in the lung. This study examines the magnitude of DVH and DMH differences for eight lung cancer patients based on intensity modulated RT (IMRT) dose distributions. Two different planning images are considered, a plan optimized on the inhale phase of 4DCT (representing idealized gating or breath-hold therapy) and a plan optimized on the average CT (aCT) density representing free-breathing treatment. These plans are optimized based on dose-volume objectives.

For the same eight patients, DMH-based IMRT optimization is performed and compared to the DVH-based plans. The same planning images are used in DMH optimization, with objectives trivially

transformed from DVH to DMH levels. Volume and mass at fixed dose levels, as well as dose at fixed volume and mass, are compared for targets and organs at risk (OAR). DMH-based plan optimization has the potential to preferentially reduce radiation path lengths through normal tissues in order to reduce normal-tissue dose and ensure massive regions of targets are treated.

Both of the planning approaches investigated in this study are idealized. The aCT density is never physically encountered, but instead represents a mass-probability distribution averaged over the breathing cycle. Single-phase gating or breath-hold, as considered in the inhale-phase optimization, is difficult (or impossible) to achieve clinically. A better approach may be to optimize dose to structure mass, as represented in individual phases of 4DCT. A hurdle in achieving this multiple-anatomy optimization (MAO) is structure definition in multi-phase images and reliable deformable image registration (DIR) between phase images. The first step in implementing a mass-based MAO is to consistently define structures in multiple anatomies and mass evaluation has the potential to aid in this process.

During respiration anatomic mass is approximately constant, and inclusion of this information may result in more consistent structure definition. Prior to considering DMH and DVH differences, and DMH-optimization, this study reports mass and mass-conservation in delineated structures as defined in different breathing phases of 4DCT. Delineating structures in all phases of 4DCT is a time-consuming task but can be done relatively quickly using DIR and contour propagation. If mass is conserved in 4DCT-phase images, evaluation of structure mass in different phases of 4DCT is a quantitative measure of intra-observer delineation consistency.

2. Methods and Materials

2.1 PATIENT DETAILS

Eight locally advanced, non-small cell lung cancer patients who received 4DCT are considered in this study. For each patient, a single simulation 4DCT is used for planning and evaluation. All (eight) of the image-sets include physician-delineated gross tumor volume (GTV) on all phase images (ten phases). Five of these image sets include physician contours of OARs on all phases, including the ipsilateral lung

contour. Each of these patients display moderate GTV motion and a range of GTV volume from 17.4 cm^3 to 189.2 cm^3, detailed in Table 1.

Table 1. Patient details. The gross tumor volume (GTV) and the lung are defined in the inhale 4DCT-phase.

	GTV:			Lung:	
	3D-Motion (cm)	Volume (cm^3)	Mass (g)	Volume (x10^3 cm^3)	Mass(g)
P1	0.39	189.20	193.20	1.18	464.09
P2	0.40	17.40	15.68	1.02	413.08
P3	0.28	79.89	74.51	2.96	881.91
P4	0.58	60.80	55.94	1.91	715.95
P5	0.69	32.60	30.06	2.40	675.30
P6	0.50	39.20	36.24	2.26	632.31
P7	0.77	53.00	44.99	2.58	802.40
P8	0.95	185.20	166.78	3.79	948.99

2.2 EVALUATION OF MASS AND VOLUME IN 4DCT

For ipsilateral lung and GTV, both volume and mass as a function of respiratory phase are reported for each patient based on a single 4DCT image sets. The contoured mass will remain constant during respiration if the images and delineated structures are an accurate representation of actual, physical patient anatomy. Volume physically varies during respiration, especially for elastic tissues in lung (Zhao *et al* 2011). The volume variation can be expressed through the tissue fiber strain. This quantity is

estimated for both lung and GTV according to Carton *et al* (1964) as $\varepsilon = \left(V_2/V_1 \right)^{1/3} - 1$, which physically represents structure deformation of an equivalent sphere in one dimension.

A physician has contoured lung and GTV on all phases of 4DCT for five patients (named contoured structures); the DIR-propagated contours (named deformed structures) are initiated with the physician-contour on the inhale phase and are deform it to nine other 4DCT-phases. The deformed structures are propagated according to demons- deformation vector fields (DVFs), calculated using the Insight Tool Kit (ITK) and implemented in a research version of the Pinnacle[3] (Philips Healthcare, Andover, MA) treatment planning system (version 9.100).   The GTV and ipsilateral lung mass and volume in contoured and deformed structures are used to evaluate intra-observer delineation consistency for the patient cohort.

Physical volume variations will occur between structures in different respiratory phases due to tissue elasticity. Mass differences between structures defined in different breathing phases, in this work, is assumed to be due to contour delineation errors. Using mass as a surrogate for spatial discrepancies, consider two spheres with volumes V_1 and V_2 (and radii r_1 and r_2). Sampling from similar density arrays, the differences in total mass (ΔM) of the two spheres can be cast into spatial estimates of delineation consistency by volume differences, $\Delta V = V_1 - V_2$. For two spheres, if ΔV is 10% of V_1, then r_2 is within 3% of r_1. For example, if a sphere with radius 3 cm (V_1=113 cm^3) increases by 10% volume, the spatial change in radius is less than 0.1 cm. However, if the sphere is deformed to a spheroid, so that the spatial discrepancy occurs over a fraction f of the original surface ($V_2 = f V_2 + (1-f) V_1$ and $\Delta V = f(V_1 - V_2)$) then the spatial discrepancies grows with decreasing f. For example, a 10% volume change due to deformation over 1/4 of the original volume (f=1/4) results in a spatial difference between r_1 and r_2 of 16% (or 0.5 cm for r_1 = 3 cm).

The estimation of contour delineation consistency assumes a constant mean density ($\overline{\rho}$) between structures in different phases, so that $\Delta M/\overline{\rho} = \Delta V$. The fractional volume of deformation is arbitrarily chose as f=1/4 in all evaluations. Based on a sphere (radius r_1) with volume equivalent to the volume of the GTV (V_{GTV}) defined in the inhale phase, $r_1 = \left(\dfrac{3}{4\pi} V_{GTV} \right)^{1/3}$. The corresponding spatial discrepancy, Δr, based on an observed mass difference (ΔM) is

$$\Delta M \big/ \overline{\rho} = \Delta V$$

$$\Delta r = r_1 - \left(\frac{3}{4\pi} \frac{(1-f)V_1 - \Delta V}{(1-f)} \right)^{1/3}$$

The mean density ($\overline{\rho}$) is estimated as the ratio of average mass and volume computed in all phases for each patient, and Δr is reported for GTV and lung based on physician and deformed contours.

2.2 DOSE-TO-VOLUME AND DOSE-TO-MASS METRICS

Relative volume and mass differences at varying dose levels, for each plan, are evaluated for all regions of interest (ROIs) at all doses. Specific values of volume and mass at dose include planning target volume (PTV) V70/M70, lung V20/M20, esophagus V25/M25, heart V30/M30, and spinal cord maximum dose. At dose level x the differences between Vx (relative volume at dose) and Mx (relative mass at dose) are reported.

DVH and DMH differences are due to two potential factors, accuracy of heterogeneous dose calculation and relative volume and mass differences in the heterogeneous, irradiated volumes. The same dose calculation algorithm is used in DVH and DMH measures; the adaptive convolve option in the Pinnacle[3] TPS, so the effects of accurate dose calculation are not considered in this study. In a structure S of volume V_s composed of n voxels of fixed volume v, DVH is a measure of relative volume at dose D; or the relative number of voxels at dose D (n_D).

$$DVH(D) = \sum_{i \in S} v \big/ V_S \left\{ D - D_i \right\}_+ = n_D \big/ n \,.$$

DMH considers the total mass of structure S (or M_S) and the mass of each voxel (m_i), returning the relative density of the tissue in S at dose D, $S(D)$.

$$DMH(D) = \sum_{i \in S} m_i \big/ M_S \left\{ D - D_i \right\}_+ = \sum_{i \in S(D)} \rho_i \Big/ \sum_{i \in S} \rho_i \,.$$

 DVH and DMH levels are compared on two image sets for each patient considered, the inhale image and the aCT density using IMRT dose distributions.

2.3 DVH AND DMH OPTIMIZATION

For each patient considered, DVH- and DMH- based IMRT optimization is carried out. The dose calculation and mass sampling is performed with dose and image voxels of 0.3x0.3x0.3 cm^3 (the images are re-sampled at the dose distribution) within the Pinnacle^3 TPS. The resulting four optimized plans per patient (2-DVH plans, 2-DMH plans) are compared. The inhale-plan density values result in well-defined (visible) image contrast; the aCT blurs the structure densities according to 10 phases of the respiratory cycle and obscures structure boundaries in many cases.

DVH plan objectives include 70 Gy to 95% of the PTV-volume and a maximum dose less than 80 Gy, while minimizing lung V20, esophagus V25, heart V30, and maximum dose in the spinal cord less than 40 Gy. DMH optimization utilizes the same beam angles and objective weightings evaluated at relative mass levels; 70 Gy to 95% of the PTV mass (M70) and minimization of the relative mass of risk structures at the same dose levels (M20 for lung, M25 for esophagus, M30 for heart). In the inhale plan, the PTV is defined as the GTV surrounded by a 1 cm margin. In the aCT plan, the PTV is a 1 cm expansion about the internal target volume (ITV) – the union of the GTV in all phase images.

The dose-volume objectives are chosen based on outcome evidence primarily from QUANTEC (Quantitative Analysis of Normal Tissue Effects in the Clinic) reports (summarized in Marks *et al* 2010b). For lungs, 20 Gy (V20 and M20) is chosen based report of Marks *et al* (2010). For the heart, 30 Gy is chosen based on the studies of Wei et al (2008) and according to the report of Gagliardi et al (2010), who show V25 > 10% of the heart results in a non-zero NTCP. The V25 & M25 level is used to estimate risk in the esophagus, which is chosen based on two studies; Belderbos et al (2005) indicate V35 as a dosimetric predictor of Grade 2 acute esophagitis at all volume levels for 156 patients, Wei et al (2008) indicate V20 as a predictor of Grade 3 acute esophagitis at volumes exceeding 35% of the organ in in a 215 patient study. The spinal cord is evaluated at a max dose of 40 Gy, with expectations that DVH and DMH differences will be negligible when evaluated at a point (or for all maximum and minimum dose objectives).

The differences in relative volume and relative mass at defined dose levels, *DVH(D) – DMH(D)*, will result in differences between DVH- and DMH- plans due to changes in trade-off consistency. In DVH-plans,

objectives are minimized until a trade-off is encountered between conflicting volumes at dose. An optimized DMH-plan will achieve tradeoff consistency between mass at dose (or DMH) levels. Another source of differences in DVH and DMH plans is explicit consideration of mass in the DMH measure. DVH optimization may encounter reduced radiation-path lengths through OARs because they reduce the objective function, whereas DMH explicitly penalizes higher density regions of OARs at dose levels.

3. RESULTS

3.1 MASS AND VOLUME VARIATIONS IN 4DCT IMAGES

Lung volume is expected to be at maximum near inhale and at minimum near exhale, but for two of the 4DCT-image sets considered there was not a clear volume/ breathing-phase relationship. The total lung volume did not vary in a predictable way for P1 and P2. Figure 1 shows relative lung mass and volume for P2, based on physician and deformed contours. Lung mass deviations > 5% are observed in both sets of contours. For the physician contours, maximum ΔM = 36.7 g resulting in Δr = 0.47 cm; in deformed contours maximum ΔM = 28.8 g with Δr = 0.36 cm. The P2-4DCT dataset has recognizable 4DCT sorting artifacts (including 'floating diaphragm') visually evident in many of the phase images. Compromised lung function and alectasis are evident in the images for P1. For this case, deformed contours indicate small volume changes (less than 18 cm^3 of air intake, a 1.5% volume change) and mass conservation to within 11.2 g (2.4% of the mass at inhale). The physician contours, in this challenging case, indicate > 6% volume variation and mass changing by > 10% (> 50 g) between different phases in the lung. Using the calculated average density of 0.38 g/cm^3, the spatial discrepancy over ¼ of an equivalent sphere is Δr = 0.38 cm when ΔM = 55 g for the physician contours of P1.
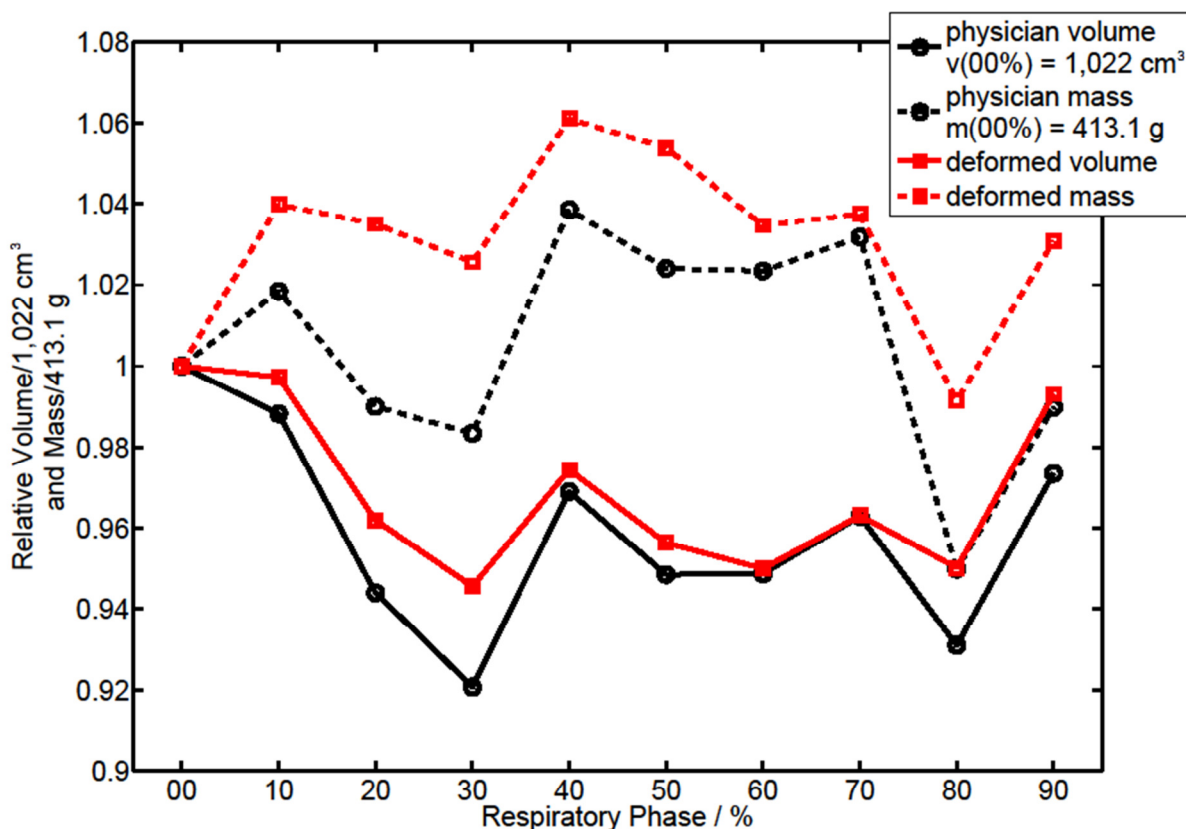
Figure 1. Relative mass and volume of lung for P2 with respect to the physician contour defined in the inhale (00%) phase for physician-defined and deformed- contours. Image artifacts are visually evident in this case and contribute to mass variations >5% in both physician and deformed contours.

Figure 2 shows the mean and two standard deviations (to show inter-patient variation) for relative mass and volume as a function of respiratory phase for three lungs (P3-P5). This data includes both physician and deformed contours and allows a direct comparison of intra-observer delineation consistency between the two. The deformed contours conserve total lung mass more consistently than physician contours for these cases based on standard deviation of the average relative mass. Statistics for each ipsilateral lung are summarized in Table 2, showing mean volume and mean mass, and the coefficient of variation (*CV*) among structures in different phases for ipsilateral lung and GTV for each patient.
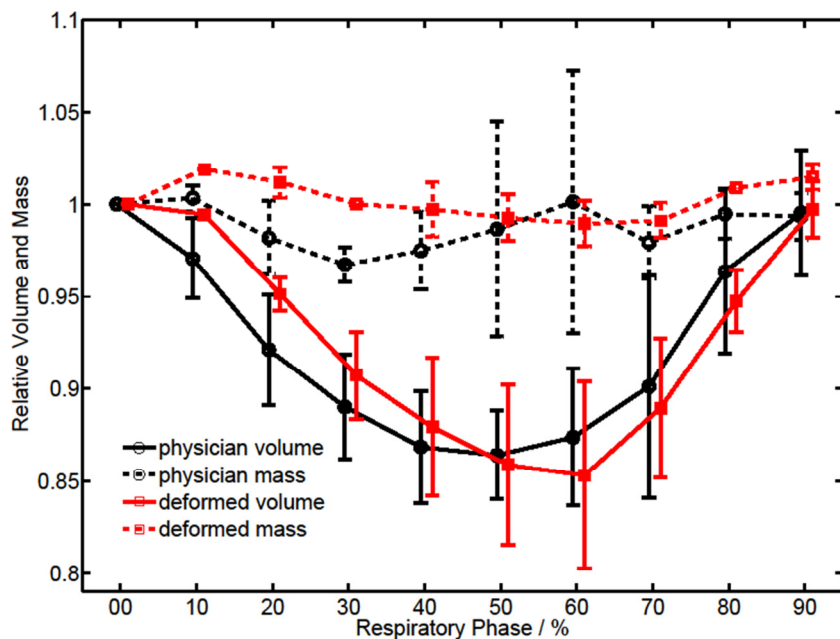
Figure 2. Relative lung mass and volume for 3 patient image sets, based on evaluation of physician-delineated and Demons-deformed contours. The deformed volumes result in a more consistent mass throughout the respiratory cycle.

Table 2. Lung volume and mass, with the coefficient of variation (CV), defined by physician contours and deformed structures.

Lung	Mean Volume (*CV*) / cm³		Mass (*CV*) / g	
	contoured	deformed	contoured	deformed
P1	1134.4 (3.0%)	1186.5 (0.4%)	433.9 (5.6%)	470.3 (0.8%)
P2	1001.2 (6.6%)	987.5 (2.2%)	415.1 (2.7%)	425.9 (2.1%)
P3	2758.6 (6.3%)	2752.3 (5.7%)	867.0 (2.0%)	879.0 (1.8%)
P4	1701.4 (7.5%)	1705.7 (8.8%)	720.7 (3.6%)	724.9 (1.7%)
P5	2291.1 (5.0%)	2251.5 (4.5%)	658.6 (2.0%)	658.6 (0.8%)
P6	-	2147.7 (3.7%)	-	634.7 (2.1%)
P7	-	2438.2 (5.2%)	-	788.2 (2.4%)
P8	-	3602.0 (3.4%)	-	952.0 (0.8%)

Gross tumor volume and masses, together with the coefficient of variation are listed for each patient in Table 3. Relative GTV mass and volume for P8 is shown in Figure 3. In this case, the physician contoured mass and volume shows phase dependence similar to the lung (for P8-GTV, physician maximum ΔM = 15.6 g, Δr = 0.16 cm, deformed maximum ΔM = 6.7 g, Δr = 0.06 cm).

The deformed contours on P7 show GTV volume and mass varies by >8% in deformed contours between phases. The relatively large variation in GTV mass for P7 indicates a failure in DIR (P7 physician maximum ΔM = 2.8 g, Δr = 0.06 cm, P7 deformed maximum ΔM = 12.4 g, Δr = 0.33 cm). A coronal slice of the inhale-phase image for P7 is shown in Figure 4. This phase is the reference image, from which all DVFs and deformed contours are generated. The sorting artifacts near the superior and inferior border of the contoured tumor, as pointed out in Figure 4, are a possible cause of the observed mass deviations in the deformed GTV structures. DIR shows larger mass variation with decreasing GTV-mass, i.e. a weak negative correlation was found between GTV volume and DIR-based mass CV across all phases (r=-0.47) and maximum mass differences across all phases (r=-0.46). There was no clear correlation in the physician-based mass CV and GTV size.

Table 3. Gross tumor volume and mass, with the coefficient of variation (CV), defined by physician contours and deformed structures. *The GTV for P7 was copied from the inhale phase to all other phases.

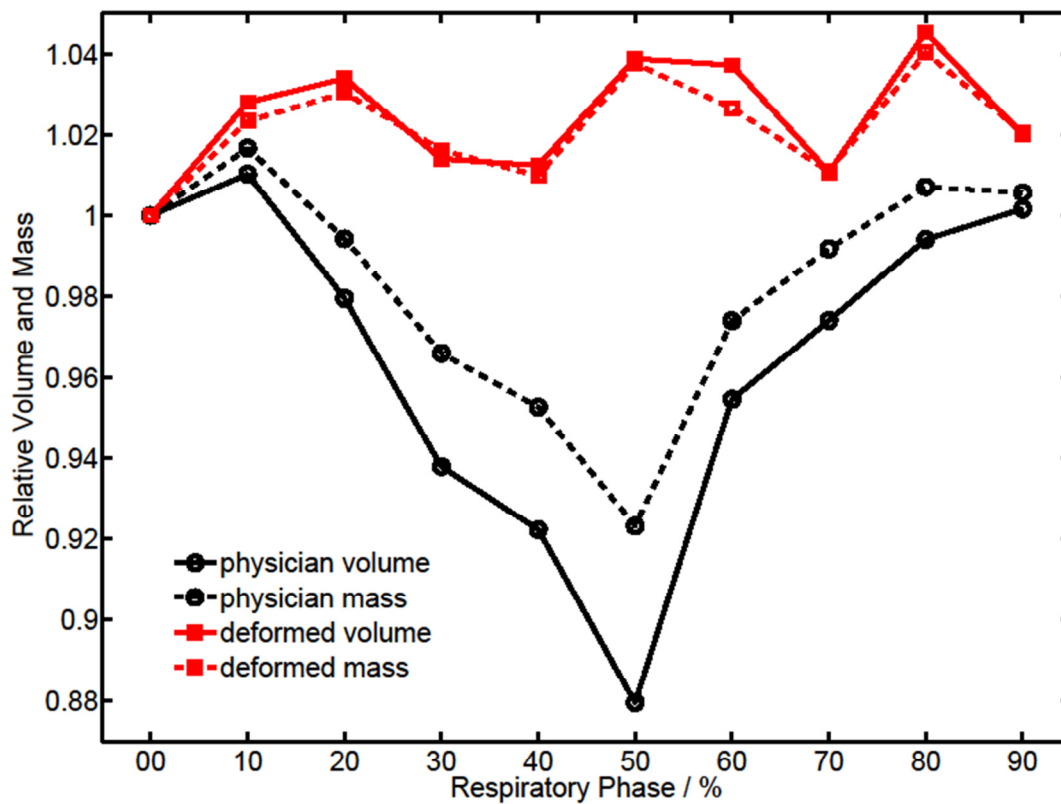| GTV	Mean Volume (CV) / cm^3		Mass (CV) / g	
	contoured	deformed	contoured	deformed
P1	180.6 (2.5%)	191.9 (0.1%)	184.0 (2.4%)	195.0 (1.0%)
P2	17.3 (1.0%)	19.1 (4.5%)	15.3 (1.9%)	16.9 (3.5%)
P3	76.6 (2.8%)	83.0 (2.1%)	71.8 (2.7%)	75.7 (2.0%)
P4	58.2 (2.2%)	64.9 (3.2%)	54.7 (1.6%)	59.0 (2.5%)
P5	32.2 (5.0%)	33.3 (3.0%)	29.6 (4.6%)	30.1 (3.0%)
P6	42.7 (4.6%)	41.5 (3.5%)	37.9 (2.1%)	37.7 (2.0%)
P7	53.0 (0.0%*)	54.2 (9.4%)	43.6 (2.5%)	45.1 (8.6%)
P8	178.8 (4.3%)	189.7 (1.4%)	164.0 (3.0%)	170.4 (1.3%)

Figure 3. Relative volume and mass for the GTV of patient 8. The physician contours show a phase dependence which is typical of the lung (at minimum in exhale, at maximum in inhale).
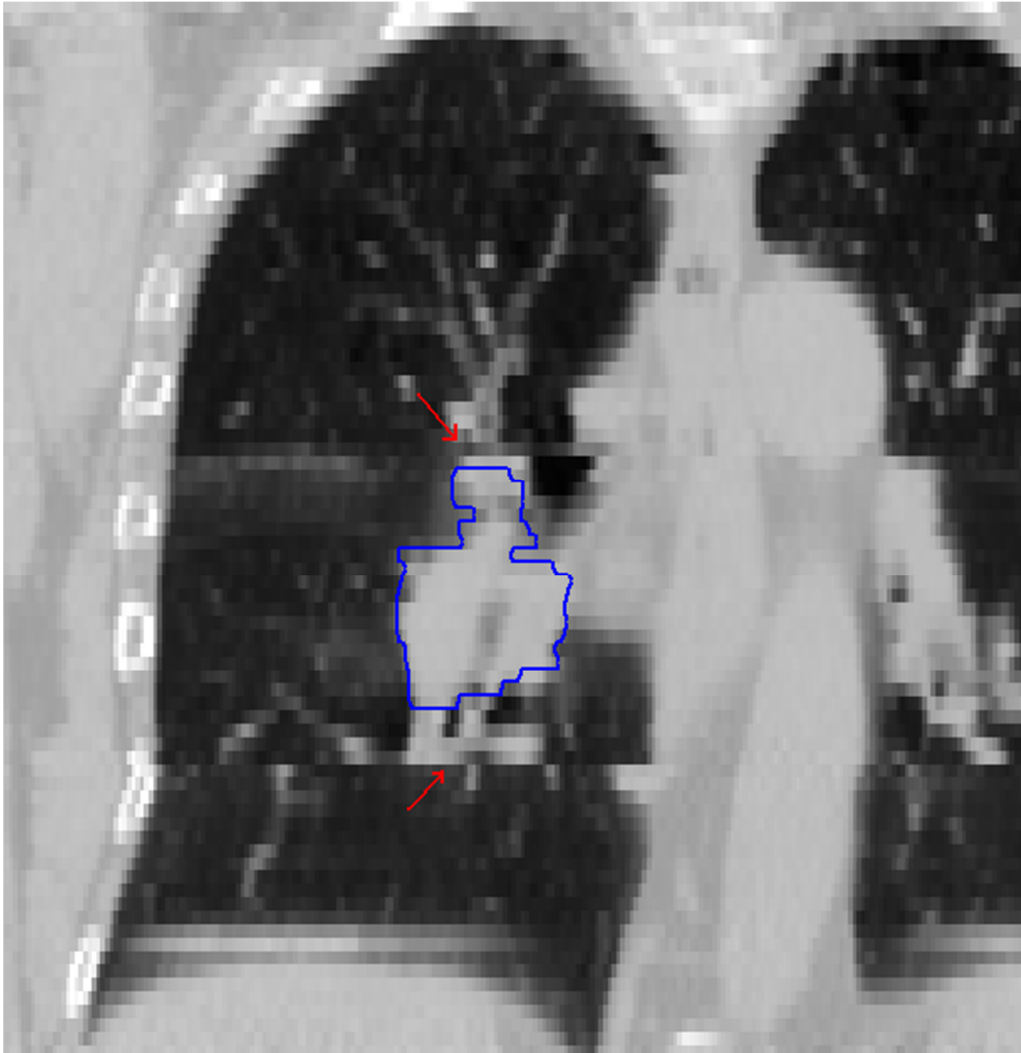
Figure 42. An inhale-phase coronal slice for P7. The sorting artifacts near the superior/inferior borders of the tumor result in >10% mass deviations in deformed GTV structures in different respiratory phases.

3.2 DVH AND DMH DIFFERENCES

DVH-based plans, optimized for delivery on both the inhale-phase image and the aCT are used to evaluate DVH and DMH differences. The differences in relative volume and relative mass at all dose

levels (DVH-DMH) are less than 3% in the spinal cord and the heart for all patients (8) and DVH-plans (16) considered. For the esophagus, 1 of 8 patients show relative mass/volume differences exceeding 3% at doses above 2 Gy. In the ipsilateral lung, differences in relative mass and volume exceed 3% in 3 of 8 inhale-based plans, and in 6 of 8 aCT- plans at dose levels ranging from 10-20 Gy.   The targets (including GTV, ITV, and PTV) show differences exceeding 3% in both inhale and aCT plans for all patients near the prescription dose. The PTV dose at 95% volume (D_{95V}), when compared to PTV dose at 95% mass (D_{95M}), differ by up to 15.7 Gy for P3, implying cold spots occur in massive regions of the PTV for this patient. For 5 of 8 patients considered, differences in D_{95V} and D_{95M} are less than 1 Gy, but for three patients these differences exceed 2 Gy in at least one of the two plans considered. Figure 5 shows the difference between relative volume and relative mass at prescription dose levels for both lungs and PTV on each of the images considered. For the GTV (in inhale plans) and ITV (in aCT plans), the results are similar to PTV, with differences occurring near the prescription dose.

Figure 6 shows the DVH and DMH for the aCT-plan for P1. In this case, relative lung mass at dose is greater than the DVH levels by at least 5% for doses ranging from 20 Gy–70 Gy. This is the only case which shows differences in esophagus DVH and DMH > 3% of the DVH value.
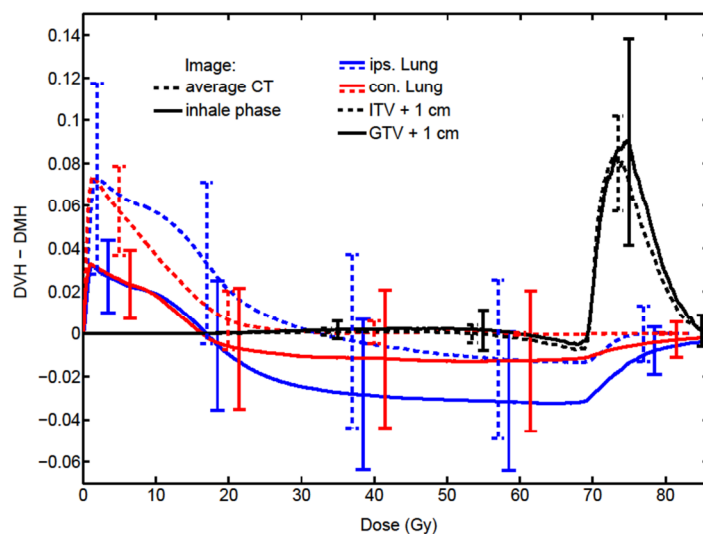

Figure 5. (DVH-DMH) Average DVH and DMH differences planned and evaluated on the inhale phase image, with the PTV defined as a 1 cm expansion of the GTV. The only structures of potential significance in all cases considered are the lungs, GTV, and PTV.
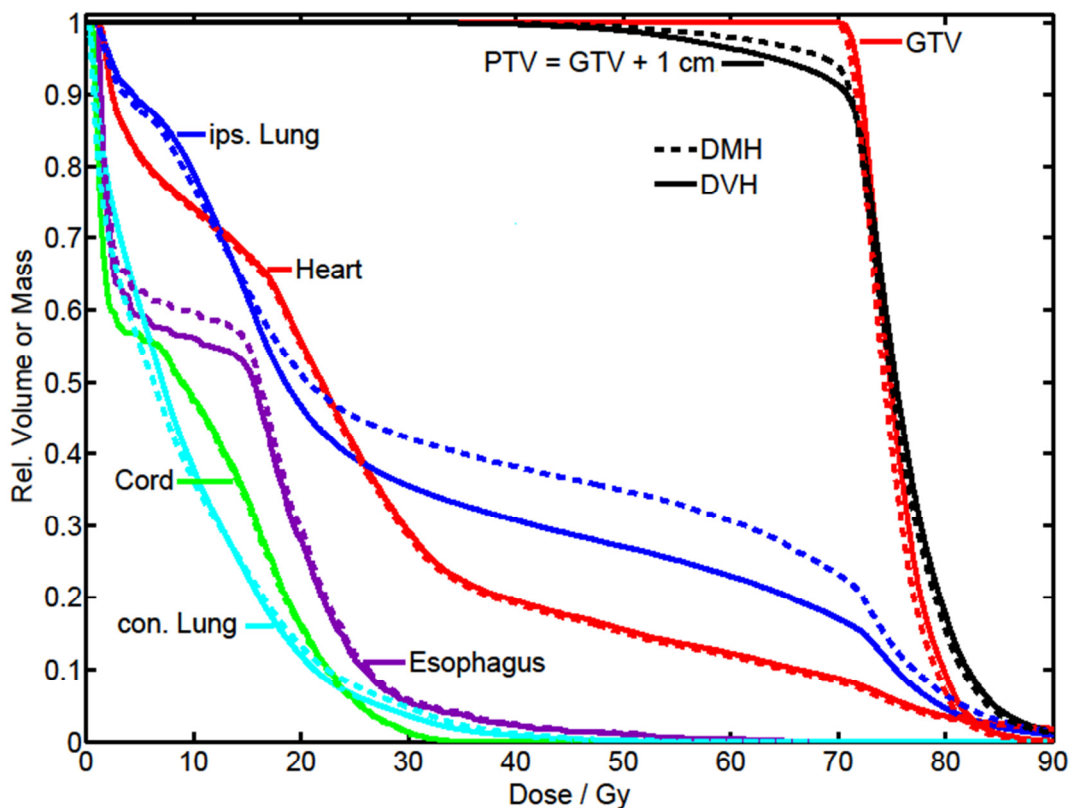
Figure 6. DVH (solid) and DMH (dasheded) values for P1 for a plan optimized on the average-CT. The optimization objectives shown as solid triangles. The relative mass at dose is higher than dose-volume levels for ipsilateral lung, esophagus, and for the PTV. This is the only case which shows >3% differences in esophagus, and these differences are far below the esophagus objective

Average DVH and DMH differences based on inhale- and aCT-images/plans across the 8-patient cohort at objective dose levels are shown in Table 4. Population average differences are normally distributed and are small for esophagus, heart, and cord. For lungs, relative volume and relative mass differences at 20 Gy ranges from -0.07 to 0.03 at 20 Gy on the inhale plans, and from -0.04 to 0.07 on aCT plans. These DVH and DMH differences have potential to impact plan optimization and outcome evaluation. For the GTV and PTV, DVH at prescription dose is consistently greater than the DMH in all inhale-plans, and in

6/8 aCT-plans. This implies that cold-spots in the target occur in regions of high density in these plans. At the prescription dose level (70 Gy), the PTV-DVH > PTV-DMH in 14/16 plans. Ipsilateral lung did not show a consistent trend in DVH and DMH differences.

Table 4 Differences between relative volume and relative mass at objective dose levels,for IMRT plans on inhale and on average-CT.   The average (μ), standard deviation (σ), and the p-value (p) calculated from a student's t-test. The dose-levels are specified following the V and M in the metric, e.g. V25 is volume receiving 25 Gy.

	Inhale-Plan			aCT-Plan		
	μ	σ	p	μ	σ	p
Esophagus (V25-M25)	-0.0013	0.0048	0.5	0.00015	0.004	0.9
Heart (V30-M30)	0.0023	0.002	0.02	0.0021	0.0019	0.02
Cord (V40-M40)	-0.00064	0.0015	0.3	0.0003	0.00085	0.4
Left Lung (V20-M20)	-0.0099	0.027	0.3	0.0022	0.024	0.08
Right Lung (V20-M20)	-0.0032	0.023	0.7	0.021	0.034	0.1
GTV / ITV (V70-M70)	0.047	0.023	0.0006	0.029	0.03	0.03
PTV (V70-M70)	0.026	0.025	0.02	0.016	0.031	0.2

3.3 DVH AND DMH OPTIMIZATION

Differences in volume and mass at prescription dose levels yield different optimized solutions based on tade-off consistency between objectives. An example of the adjustments when considering DMH, instead of DVH, is shown in Figure 7 for the aCT-plan of P4. Both lung V20-M20 (=0.046) and PTV V70-M70 (=0.063) are greater than zero, so the DMH-optimized plan increases lung-mass at 20 Gy in order to ensure PTV-mass coverage at 70 Gy. The converse is true for P1, shown in the previous section. For this

plan, for both lung and PTV, DMH > DVH at objective dose levels so that DMH-optimization reduces both PTV-dose at mass and lung-dose at mass, in order to reduce the objective function.
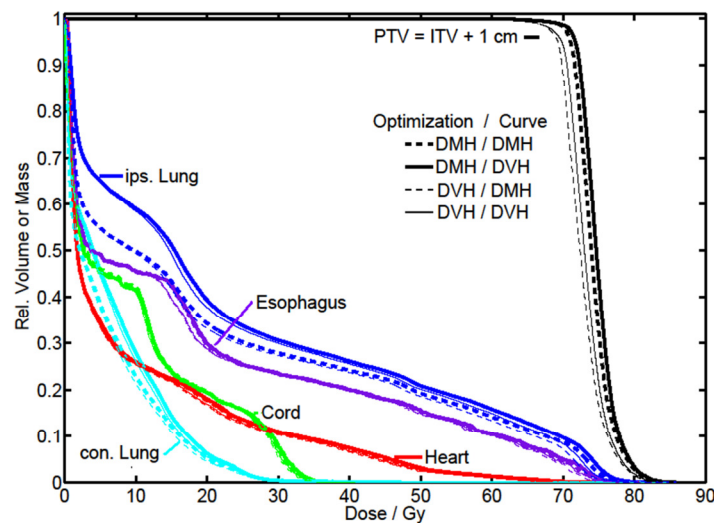

Figure 7. DVH (solid) and DMH (dashed) curves resulting from DVH-optimization (thin) and DMH-optimization (thick) for P4. Because lung DMH<DVH, the DMH-optimized plan results in better PTV coverage. Dose to 95% of the PTV-mass is increased from 69.3 Gy in the DVH- optimized plan, to 71.1 Gy in the DMH- optimized plan.

In 13/16 DVH-optimized plans, cold-spot distributions in dense PTV sub-volumes result in V70 > M70 and led to increased PTV-mass coverage in DMH-optimized plans. However, the difference in dose to 95% volume (PTV-D_{95V}) and dose to 95% mass (PTV-D_{95M}) between DVH and DMH plans is less than 2 Gy in 6 of 8 inhale-plans, and in 6 of 8 aCT-plans (and in both aCT and inhale plans in 5 of 8 patients considered). This was not the case for P3, where PTV-D_{95M} increases from 49.7 Gy to 58.4 Gy. This 8.7 Gy increase in mass-coverage is achieved by increasing PTV-D_{95V} by just 3.2 Gy (from 65.4 Gy in the DVH-plan to 68.6 Gy in the DMH-plan). A different trend was observed for P1, where lung DMH > DVH by 15.7% of the DVH value in the inhale-plan and by 9% in the aCT-plan. By optimizing DMH for P1, PTV-D_{95V} is reduced by 12.6 Gy in the inhale plan and by 8.5 Gy in the aCT plan, resulting in reduced lung mass and volume at dose (by 9-14% of DVH-optimized values); however, PTV-D_{95M} is reduced by just 2.5 Gy in the inhale plan (69.4 Gy to 66.9 Gy) and by 1.8 Gy (68.8 Gy to 67 Gy) in the aCT-plan. The comparison of DVH and DMH optimized inhale-plans for P1 is shown in Figure 8. A large reduction in PTV-volume at dose allowed significant sparing while maintaining an acceptable PTV-mass at prescription dose.
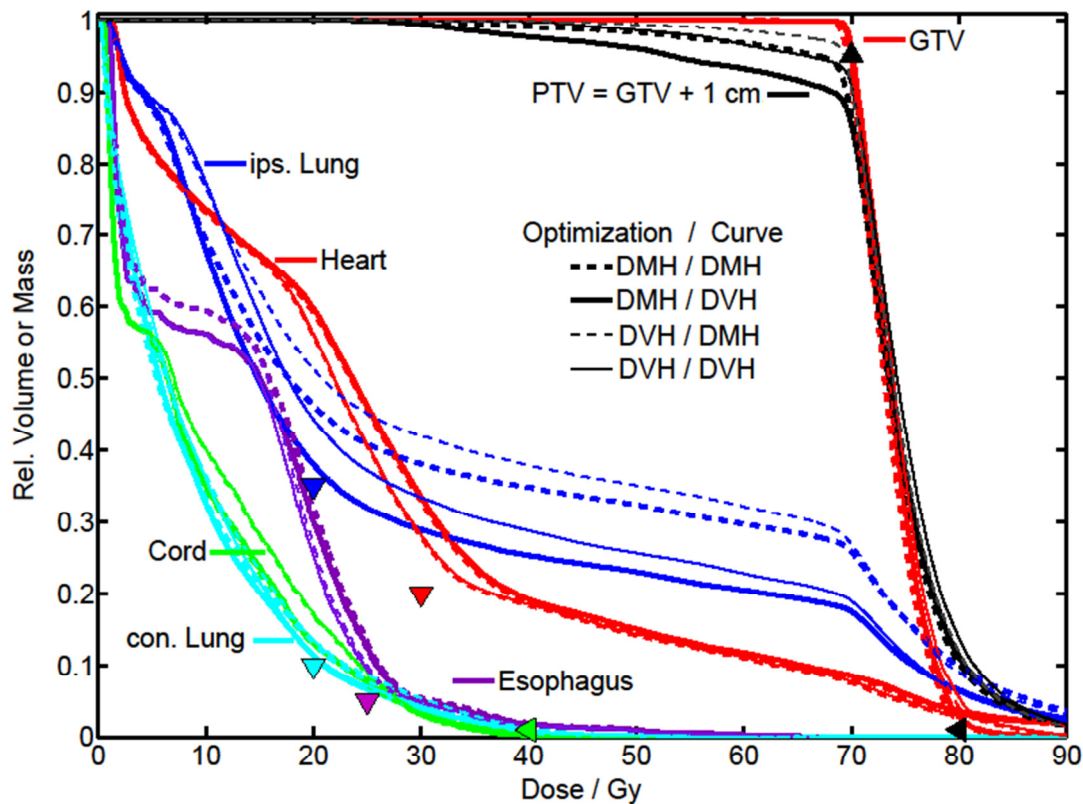
Figure 8. DVH (solid) and DMH (dashed) curves resulting from DVH-optimization (thin) and DMH-optimization (thick) for P1. DMH-optimization reduces dose at 95% PTV volume by 12.6 Gy compared to DVH-optimized levels in order to reduce ipsilateral lung mass at 20 Gy. Even though the PTV-volume is clearly under-dosed, the dose at 95% of PTV mass is 66.9 Gy.

4. DISCUSSION

The current standard for simulation of lung cancer patients is 4DCT; under the assumption that 4D information will improve the quality of plans and associated risk/benefit analysis. In a first stage towards this goal, anatomical structures must be well defined with minimal inter- and intra- observer contouring variability (Louie *et al* 2010). Evaluation of structure mass in different phases of 4DCT has the potential to lead to more consistent structure definition, and using DIR to define structures will

reduce the physician delineation workload by a factor of 5 or more. In this work, consistent GTV mass across different breathing phases using demons DIR is observed for 7/8 patients; and compared to delineated structures the deformed GTV shows smaller mass variation in 5/8 4DCT image set (comparable mass conservation in two more cases). In 1 image set, however, DIR failed to preserve mass across respiratory phases due to image-artifacts – that is, mass-based evaluation of structures identified registration problems that require attention. If structure definition can be improved, which certainly requires careful steps to ensure 4DCT images are free of artifacts, structure density as reported in 4DCT has the potential to be correlated to function (Ma *et al* 2009). If artifacts are present, which have been shown to be prevalent in 4DCT image sets (Yamamoto *et al* 2008), the findings of this study suggest they can be identified through DIR-contour propagation and mass analysis.

For lung, density may not correlate well with lung functionality, very low density parenchyma may be significant to oxygen exchange. Lung on CT is primarily composed of a mixture of blood vessels, blood, and air, with functional alveoli difficult or impossible to identify. Several authors have incorporated lung perfusion imaging in plan optimization (Seppenwoolde *et al* 2002, Christian *et al* 2005, McGuire *et al* 2006, Shioyama *et al* 2007, Lavrenkov *et al* 2007, Munawar *et al* 2010) and beam angle optimization (McGuire 2010) to reduce dose to functional lung. Castillo *et al* (2010) have considered methods to produce ventilation images from 4DCT data sets, and have shown that neither the Jacobian determinant of the DVF nor the fractional air content of each voxel correlates well with perfusion imaging, with dice similarity coefficients less than 0.4 in six of seven cases. In this study, mass is used as a surrogate for voxel importance in optimization for lung cancer. The method proposed here can take advantage of reduced radiation path-lengths through tissue, regardless of functionality. By preferentially treating the tumor through lower density normal tissue, more unit incident fluence is delivered to the tumor. However, using mass (and density) as a surrogate for cell importance can be replaced by some other indicator of functionality (e.g. perfusion) if one is available.

Comparison of dose-at-volume (using DVH) with dose-at-mass (using DMH) shows differences in lung volume at fixed dose often exceed 5% and exceed 2Gy at fixed volume or mass. The study of Mavroidis *et al* (2006) shows similar results. It is possible that these differences have a one-to-one correspondence with uncertainty in outcome data relying on the DVH (Lyman 1985), based on the linear-quadratic prospective model of cell-kill. This study shows DVH and DMH in both lung and lung-

cancer targets can vary by >10%, and the sign of this difference is patient and radiation-path dependent. For a set of voxels composing a given volume, the subset of irradiated voxels may have a different mean density than the entire structure mean. No conclusive generalization can be made about DVH and DMH differences; the irradiated volume may be more dense than the structure mean (and DMH>DVH) or less dense than the structure mean (with DMH<DVH).

5. CONCLUSIONS

The results of this study show the utility of structure mass in structure delineation, in dose evaluation, and in RT plan optimization. Relying on the premise that mass is constant during respiration, evaluation of structure mass defined on different respiratory-phases measures intra-observer delineation consistency. Using DIR to define contours often results in more consistent structure mass between phases compared to physician contours, but DIR failed in the presence of image artifacts. In dose evaluation using the DMH, density of the irradiated tissue is explicitly included in evaluation, rather than consider the entire structure which may include non-functional sub-units, the density of irradiated tissue is explicitly included inmass-based evaluation. Finally, optimizing RT plans using mass (and the DMH) has the potential to reduce radiation path lengths by treating less dense regions of normal tissue as well as increasing importance in massive regions of the target.

ACKNOWLEDGEMENTS

References

The Insight Segmentation and Registration Toolkit (ITK) Online: www.itk.org

Attix F H 1991 *Introduction to Radiological Physics and Radiation Dosimetry* (Wiley-VCH) Online: http://www.goodreads.com/book/show/320576.Introduction_to_Radiological_Physics_and_Radiation_Dosimetry

Carlsson C 1963 Determination of Integral Absorbed Dose from Exposure Measurements *Acta Oncologica* **1** 433–58

Carton R W, Clark J W, Dainauskas J and Barron A 1964 Estimation of tissue elasticity of the lung *J Appl Physiol* **19** 236–42

Castillo R, Castillo E, Martinez J and Guerrero T 2010 Ventilation from four-dimensional computed tomography: density versus Jacobian methods *Physics in Medicine and Biology* **55** 4661–85

Christian J A, Partridge M, Nioutsikou E, Cook G, McNair H A, Cronin B, Courbon F, Bedford J L and Brada M 2005 The incorporation of SPECT functional lung imaging into inverse radiotherapy planning for non-small cell lung cancer *Radiother Oncol* **77** 271–7

D'Souza W D and Rosen I I 2003 Nontumor integral dose variation in conventional radiotherapy treatment planning *Medical Physics* **30** 2065–71

Lavrenkov K, Christian J A, Partridge M, Niotsikou E, Cook G, Parker M, Bedford J L and Brada M 2007 A potential to reduce pulmonary toxicity: the use of perfusion SPECT with IMRT for functional lung avoidance in radiotherapy of non-small cell lung cancer *Radiother Oncol* **83** 156–62

Louie A V, Rodrigues G, Olsthoorn J, Palma D, Yu E, Yaremko B, Ahmad B, Aivas I and Gaede S 2010 Inter-observer and intra-observer reliability for lung cancer target volume delineation in the 4D-CT era *Radiotherapy and Oncology* **95** 166–71

Lyman J T 1985 Complication Probability as Assessed from Dose-Volume Histograms *Radiation Research* **104** S13–S19

Ma J, Zhang J, Zhou S, Hubbs J L, Foltz R J, Hollis D R, Light K L, Wong T Z, Kelsey C R and Marks L B 2009 Association Between RT-Induced Changes in Lung Tissue Density and Global Lung Function *International Journal of Radiation Oncology*Biology*Physics* **74** 781–9

Marks L B, Bentzen S M, Deasy J O, Kong F-M (Spring), Bradley J D, Vogelius I S, El Naqa I, Hubbs J L, Lebesque J V, Timmerman R D, Martel M K and Jackson A 2010a Radiation Dose–Volume Effects in the Lung *International Journal of Radiation Oncology*Biology*Physics* **76** S70–S76

Marks L B, Ten Haken R K and Martel M K 2010b Guest Editor's Introduction to QUANTEC: A Users Guide *International Journal of Radiation Oncology*Biology*Physics* **76** S1–S2

Mavroidis P, Plataniotis G A, Górka M A and Lind B K 2006 Comments on "Reconsidering the definition of a dose–volume histogram"—dose–mass histogram (DMH) versus dose–volume histogram (DVH) for predicting radiation-induced pneumonitis *Physics in Medicine and Biology* **51** L43–L50

McGuire S M, Zhou S, Marks L B, Dewhirst M, Yin F-F and Das S K 2006 A methodology for using SPECT to reduce intensity-modulated radiation therapy (IMRT) dose to functioning lung *Int. J. Radiat. Oncol. Biol. Phys.* **66** 1543–52

Munawar I, Yaremko B P, Craig J, Oliver M, Gaede S, Rodrigues G, Yu E, Reid R H, Leung E, Urbain J-L, Chen J and Wong E 2010 Intensity modulated radiotherapy of non-small-cell lung cancer incorporating SPECT ventilation imaging *Med Phys* **37** 1863–72

Niemierko A and Goitein M 1993 Modeling of normal tissue response to radiation: The critical volume model *International Journal of Radiation Oncology*Biology*Physics* **25** 135–45

Nioutsikou E, Webb S, Panakis N, Bortfeld T and Oelfke U 2005 Reconsidering the definition of a dose--volume histogram *Physics in Medicine and Biology* **50** L17–L19

Reese A S, Das S K, Curle C and Marks L B 2009 Integral dose conservation in radiotherapy *Medical Physics* **36** 734–40

Seppenwoolde Y, Engelsman M, De Jaeger K, Muller S H, Baas P, McShan D L, Fraass B A, Kessler M L, Belderbos J S A, Boersma L J and Lebesque J V 2002 Optimizing radiation treatment plans for lung cancer using lung perfusion information *Radiotherapy and Oncology* **63** 165–77

Shioyama Y, Jang S Y, Liu H H, Guerrero T, Wang X, Gayed I W, Erwin W D, Liao Z, Chang J Y, Jeter M, Yaremko B P, Borghero Y O, Cox J D, Komaki R and Mohan R 2007 Preserving Functional Lung Using Perfusion Imaging and Intensity-Modulated Radiation Therapy for Advanced-Stage Non–Small Cell Lung Cancer *International Journal of Radiation Oncology*Biology*Physics* **68** 1349–58

Shipley W U, Tepper J E, Prout G R Jr, Verhey L J, Mendiondo O A, Goitein M, Koehler A M and Suit H D 1979 Proton radiation as boost therapy for localized prostatic carcinoma *JAMA* **241** 1912–5

Yamamoto T, Langner U, Loo Jr. B W, Shen J and Keall P J 2008 Retrospective Analysis of Artifacts in Four-Dimensional CT Images of 50 Abdominal and Thoracic Radiotherapy Patients *International Journal of Radiation Oncology*Biology*Physics* **72** 1250–8

Zhao T, White B, Moore K L, Lamb J, Yang D, Lu W, Mutic S and Low D A 2011 Biomechanical interpretation of a free-breathing lung motion model *Physics in Medicine and Biology* **56** 7523–40

Appendix E

Multi-criteria Optimization for Real-Time Planning of
Lung Cancer Radiotherapy

W.T. Watkins[1], W.Y. Song[2], E. Weiss[1], J.R. Merrick[1], G. D. Hugo[1], J. V. Siebers[1]

[1]Virginia Commonwealth University, Richmond, VA

[2]University of California San Diego, La Jolla, CA

Purpose. Multi-criteria optimization (MCO) is implemented for planning lung cancer radiotherapy treatments to clarify patient-specific tradeoffs and allow real-time plan decision making.

Methods. For four locally advanced lung cancer patients (Pt1-Pt4), a basis set of MCO plans are constructed and compared to plans determined from fixed-objective (FO) optimization for organs at risk (OARs). All optimized plans include constraints on target-D_{95}>70 Gy and spinal cord D_{max}<45 Gy. Five MCO basis plans are designed per patient through weight variation of four non-zero dose-volume objectives (DVOs) for ipsilateral lung (iLung), contralateral lung (cLung), heart, and esophagus. The five basis plans are optimized according to: (1) simultaneous minimization of four OAR-DVOs and (2-5) weight variation for one OAR-DVO.

Results. Patient-specific tradeoffs between OAR objectives are revealed with MCO which are not evident in FO-optimization. For Pt1, MCO basis plans vary iLung-V_{20} from 46% to 65% and show that V_{20}<46% is not achievable; the FO iLung-V_{20} is 54%. For Pt2,the FO-plan trades off a 1% reduction in iLung-V_{20} for a 29% increase in esophagus-V_{20}. An interpolated MCO plan, in this case, takes advantage

of this tradeoff to reduce esophagus V20 by from 41% to 8%. Pt3 shows increasing heart-V_{20} by 35% (from 20% to 55%) results in a 7% (34%-27%) reduction in iLung-V_{20}. With Pt4, MCO reveals a tradeoff between the two lungs; varying iLung-V_{20} from 23% to 30% corresponds to cLung-V_{20} varying from 23% to 17%. The FO plan treats cLung up to the V_{20} objective (to 29%) without penalty. MCO shows the ability to reduce OAR dose-volumes, but often led to increased PTV hotspots.

Conclusions. Analysis of MCO plans clarifies conflicting objectives and exposes inherent limitations due to patient geometry. Real-time decision making is possible with a small set of MCO plans, and achieves plans which are superior to FO-optimization.

Vita

William Tyler Watkins was born in Grossmont Hospital, San Diego, CA, on 4/27/1979. Tyler grew up in Ramona, CA and South Page, IA, attending both South Page High School and Ramona High School. He went to college at San Diego State University and was awarded a B.S. in Physics with a minor in mathematics in 2003 and an M.S. in physics in 2009. Tyler moved to Richmond, VA in 2010, in order to pursue his Ph.D. and work with Dr. Jeff Siebers.